

INFORMATION TO USERS

This manuscript has been reproduced from the microfilm master. UMI films the text directly from the original or copy submitted. Thus, some thesis and dissertation copies are in typewriter face, while others may be from any type of computer printer.

The quality of this reproduction is dependent upon the quality of the copy submitted. Broken or indistinct print, colored or poor quality illustrations and photographs, print bleedthrough, substandard margins, and improper alignment can adversely affect reproduction.

In the unlikely event that the author did not send UMI a complete manuscript and there are missing pages, these will be noted. Also, if unauthorized copyright material had to be removed, a note will indicate the deletion.

Oversize materials (e.g., maps, drawings, charts) are reproduced by sectioning the original, beginning at the upper left-hand corner and continuing from left to right in equal sections with small overlaps.

Photographs included in the original manuscript have been reproduced xerographically in this copy. Higher quality 6" x 9" black and white photographic prints are available for any photographs or illustrations appearing in this copy for an additional charge. Contact UMI directly to order.

Bell & Howell Information and Learning
300 North Zeeb Road, Ann Arbor, MI 48106-1346 USA
800-521-0600

UMI[®]

THE FLORIDA STATE UNIVERSITY
COLLEGE OF ARTS AND SCIENCES

INTERANNUAL VARIABILITY IN THE
EASTERN SUBTROPICAL PACIFIC OCEAN

By

ALAN P. LEONARDI

A dissertation submitted to the
Department of Oceanography
in partial fulfillment of the
requirements for the degree of
Doctor of Philosophy

Degree Awarded:
Fall Semester, 2000

UMI Number: 9994571



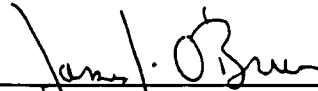
UMI Microform 9994571

Copyright 2001 by Bell & Howell Information and Learning Company.

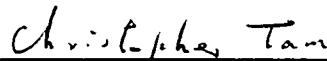
All rights reserved. This microform edition is protected against
unauthorized copying under Title 17, United States Code.

Bell & Howell Information and Learning Company
300 North Zeeb Road
P.O. Box 1346
Ann Arbor, MI 48106-1346

The members of the Committee approve the dissertation of Alan
P. Leonardi defended on June 7, 2000.



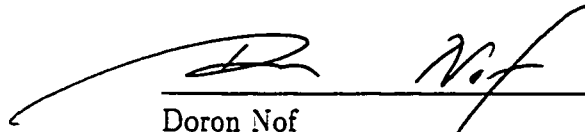
James J. O'Brien
Professor Directing Dissertation



Christopher K. W. Tam
Outside Committee Member



William K. Dewar
Committee Member



Doron Nof
Committee Member



Richard L. Iverson
Committee Member

Ai miei genitori, mia famiglia, e miei amici. Soprattutto mia mamma, *Hollis*; mio padre, *Gregory*; mio fratello, *Scott*; e *principessa*, la guardina del mio cuore.

ACKNOWLEDGEMENTS

My appreciation goes out to Dr. O'Brien, whose guidance and insight has led me to be not only a better researcher, but also a better person.

I would also like to thank my committee members, Dr.'s Dewar, Iverson, Nof, and Tam, for their helpful comments regarding the contents of this dissertation. Special thanks to Mr. E. J. Metzger and Dr. H. Hurlburt of Naval Research Laboratories for many helpful discussions about and the use of results from their model, the NLOM.

Further thanks is extended to all of the members of COAPS who helped make this research what it is today. In particular, the help and encouragement of Dr. S. Morey, Mr. C. Tilburg, Mr. L. Zamudio, and Dr. B. Subrahmanyam have aided in the production of this dissertation as well as my mental well being. Thanks for all you have done.

Finally, I would like to thank Dr. T. Busalacchi and all of the members of the Laboratory for Hydrospheres, NASA Goddard Space Flight Center. Their helpful comments regarding the presentation of this material are greatly appreciated.

TABLE OF CONTENTS

LIST OF FIGURES	vii
ABSTRACT	xi
1. INTRODUCTION	1
2. MODEL AND DATA	7
2.1 Eddy Resolving General Circulation Model	7
2.2 TOPEX/Poseidon Altimetry	9
3. METHODOLOGY	12
3.1 Decimating the NLOM Data	12
3.2 Empirical Orthogonal Function (EOF) Analysis	15
3.3 Singular Value Decomposition (SVD) Analysis	19
3.4 Multi-channel Singular Spectrum Analysis (M-SSA)	23
4. MODEL/DATA COMPARISON	25
4.1 Wind Comparisons	26
4.2 Sea Surface Height (SSH) Comparisons	31
Empirical Orthogonal Function (EOF) Analysis	31
Singular Value Decomposition (SVD) Analysis	34
Longitude-Time Comparisons	37

5. RESULTS AND DISCUSSION	42
5.1 Large Scale Ekman Pumping	45
5.2 Propagating Patterns	49
5.3 Forced Atmosphere-Ocean Response	58
5.4 Discussion	61
6. SUMMARY AND CONCLUSIONS	68
APPENDICES	70
A. SYMBOLS	70
B. HANNING FILTER	72
C. (INTER)DECADAL VARIABILITY	77
REFERENCES	82
BIOGRAPHICAL SKETCH	88

LIST OF FIGURES

1	Comparison of the original sea surface height (SSH) data (top) and the decimated data (bottom) from the Naval Research Laboratory (NRL) Layered Ocean Model (NLOM). The data are a snapshot of the 3.05 day output from the high resolution model. Original data have a grid spacing of $1/16^\circ \times 45/512^\circ$ (latitude \times longitude) while the decimated data have a grid spacing of $1^\circ \times 1^\circ$. Units for SSH are <i>cm</i> . .	13
2	Comparison of the original sea surface height (SSH) time series with the decimated data time series along representative longitudinal (left column) and latitudinal (right column) transects. SSH data are plotted every 3.05 days with units of <i>cm</i> . .	14
3	First mode EOF spatial amplitude functions of the filtered FSU pseudo (top) and ECMWF/HR hybrid wind (bottom) zonal stresses (τ^z) along with their associated principal components (middle, FSU=black line, ECMWF/HR=red line). Both modes represent 24% of the overall variance.	27
4	Second mode EOF spatial amplitude functions of the normalized FSU pseudo (top) and ECMWF/HR hybrid wind (bottom) zonal stresses (τ^z) along with their associated principal components (middle, FSU=black line, ECMWF/HR=red line). Both modes represent 24% of the overall variance.	28
5	First mode EOF spatial amplitude functions of the unfiltered FSU pseudo (top) and ECMWF/HR hybrid wind (bottom) zonal stresses (τ^z) along with their associated principal components (middle, FSU=black line, ECMWF/HR=red line). Each mode represents 16% and 15% of the overall variance for the FSU and ECMWF/HR winds respectively.	30
6	First mode EOF spatial amplitude functions of the unfiltered NLOM (top) and TOPEX/POSEIDON (T/P, bottom) sea surface height (SSH) along with their associated principal components (middle, NLOM=black line, T/P=red line). Each mode represents 16% and 22% of the overall variance for the NLOM and T/P SSH respectively.	32
7	Second mode EOF spatial amplitude functions of the unfiltered NLOM (top) and TOPEX/POSEIDON (T/P, bottom) sea surface height (SSH) along with their associated principal components (middle, NLOM=black line, T/P=red line). Each mode represents 12% and 12% of the overall variance for the NLOM and T/P SSH respectively.	33

8	Third mode EOF spatial amplitude functions of the unfiltered NLOM (top) and TOPEX/POSEIDON (T/P, bottom) sea surface height (SSH) along with their associated principal components (middle, NLOM=black line, T/P=red line). Each mode represents 10% and 7% of the overall variance for the NLOM and T/P SSH respectively.	34
9	First mode SVD spatial eigenvectors of the low pass filtered NLOM (top) and TOPEX/POSEIDON (T/P, bottom) sea surface height (SSH) along with their associated eigenfunctions (middle, NLOM=black line, T/P=red line). The coupled mode clearly depicts an interannual signal and accounts for 67% of the squared covariance.	35
10	Second mode SVD spatial eigenvectors of the low pass filtered NLOM (top) and TOPEX/POSEIDON (T/P, bottom) sea surface height (SSH) along with their associated eigenfunctions (middle, NLOM=black line, T/P=red line) accounting for 19% of the squared covariance.	36
11	Third mode SVD spatial eigenvectors of the low pass filtered NLOM (top) and TOPEX/POSEIDON (T/P, bottom) sea surface height (SSH) along with their associated eigenfunctions (middle, NLOM=black line, T/P=red line) accounting for 10% of the squared covariance.	37
12	Longitude-time representations of the NLOM and T/P derived SSH signatures along the equator. The left two panels represent the unfiltered NLOM and T/P SSH respectively, while the right two panels compare the low pass filtered NLOM and T/P SSH signals. Units are centimeters.	38
13	Longitude-time representations of the NLOM and T/P derived SSH signatures along 10°N. The left two panels represent the unfiltered NLOM and T/P SSH respectively, while the right two panels compare the low pass filtered NLOM and T/P SSH signals. Units are centimeters.	39
14	Longitude-time representations of the NLOM and T/P derived SSH signatures along 20°N. The left two panels represent the unfiltered NLOM and T/P SSH respectively, while the right two panels compare the low pass filtered NLOM and T/P SSH signals. Units are centimeters.	40
15	Longitude-time representations of the NLOM and T/P derived SSH signatures along 30°N. The left two panels represent the unfiltered NLOM and T/P SSH respectively, while the right two panels compare the low pass filtered NLOM and T/P SSH signals. Units are centimeters.	41

16	First mode SVD spatial eigenvectors of the monthly mean NLOM upper layer thickness (top) and ECMWF/HR monthly wind stress curl (bottom) along with their associated eigenfunctions (middle, NLOM=black line, ECMWF/HR=red line) accounting for 39% of the overall variance.	46
17	Second mode SVD spatial eigenvectors of the monthly mean NLOM upper layer thickness (top) and ECMWF/HR monthly wind stress curl (bottom) along with their associated eigenfunctions (middle, NLOM=black line, ECMWF/HR=red line) accounting for 24% of the overall variance.	47
18	Modeled upper layer thickness anomaly (left) and upper layer thickness anomaly associated with the coupled SVD mode 2 (right) along 20°N upstream of the Hawaiian Islands. For comparison purposes, the modeled upper layer thickness is normalized in a manner consistent with the SVD analysis (see section 3.3). The coupled standing mode (right) represent 24% of the overall coupled variance.	48
19	Mode 1 CEOF upper layer thickness response representing 21% of the overall variance for the unfiltered monthly data. Shown clockwise from the top left are the (a) spatial amplitude function, (b) the temporal amplitude function, (c) the temporal phase (in radians), and (d) the spatial phase (in radians). Note: the large north south dipole in the spatial phase and the shift in temporal phase represent a low frequency, large spatial scale change in the overall structure of the eastern North Pacific Ocean, possibly associated with the Pacific Decadal Oscillation (PDO, see Appendix C).	50
20	As in figure 19, except for CEOF mode 2 representing 15% of the overall variance.	51
21	As in figure 19, except for CEOF mode 3 representing 8% of the overall variance.	52
22	As in figure 19, except for CEOF mode 4 representing 5% of the overall variance.	53
23	As in figure 19, except for CEOF mode 5 representing 4% of the overall variance.	54
24	Hovmöller plots along 20° of CEOF modes 1-5. Shown are the modes themselves (a-e) as well as the modes summed consecutively. For example, panel (c) shows the response of mode 3 by itself, while panel (h) shows the attenuated effects of modes 1-3. Similarly, panel (e) shows the response of mode 5 alone, while panel (j) shows the attenuated response of modes 1-5. units are cm. Variances are given as the percent of overall variance associated with the given mode (a-e) and the variance associated with the attenuated response of the summed modes (f-j).	56
24	(Continued).	57

25	Multi-channel singular spectrum analysis (M-SSA) results for upper layer thickness (ULT) and wind stress curl (WSC). Interannual variability is represented by reconstructed components 1 and 2 (RC_{1-2}) for both ULT, carrying 59% of the variance (top left), and WSC, carrying 21% of the variance (top right), respectively. The reconstructed principal components (middle panel) are highly correlated, $r = -0.76$ at the 99% confidence level, with WSC variations leading ULT by 3 months. Both ULT (bottom panel, solid line) and WSC (bottom panel, dashed line) show strong spectral peaks in the interannual band with frequencies corresponding to ~ 51 months.	65
26	As in figure 25, but for M-SSA reconstructed modes 3 and 4 (RC_{3-4}). A clear interdecadal signal is exhibited with slight propagation. Both signals are highly correlated in time ($r = -0.59$ at the 99% level) with frequency peaks in the interdecadal bands.	66
27	As in figure 25 but for M-SSA reconstructed modes 5 through 10 (RC_{5-10}). Quasi-biennial variability is exhibited for both ULT and WSC anomalies, but with low correlation. The two modes represent differing signals with ULT anomalies being biennial Rossby waves with a period of 24 months, and WSC anomalies representing a quasi-biennial standing mode with period of 17 months.	67
28	Example of successive application of a Hanning filter. Here, the order of the hanning filter represents the number of successive applications of the filter. i.e. a 6 th order Hanning filter means the filter was applied repetitively 6 times to the original data. Top: The original data along with the low pass filtered data. Bottom: Power response associated with the 6 th order Hanning filter. Clearly, over 40% of the power is retained at frequencies lower than $0.0027day^{-1}$ (dashed line, corresponding to a time scales longer than 1 year).	76
29	First mode SVD spatial eigenvectors of the monthly mean NLOM upper layer thickness (top) and ECMWF/HR monthly wind stress curl (bottom) along with their associated eigenfunctions (middle, NLOM=black line, ECMWF/HR=red line) accounting for 34% of the overall variance. For comparison purposes, the PDO index is plotted (in blue) along with the SVD eigenfunctions.	78
30	Second mode SVD spatial eigenvectors of the monthly mean NLOM upper layer thickness (top) and ECMWF/HR monthly wind stress curl (bottom) along with their associated eigenfunctions (middle, NLOM=black line, ECMWF/HR=red line) accounting for 20% of the overall variance. For comparison purposes, the low pass filtered ALPI is plotted (in blue) along with the SVD eigenfunctions. . .	80

ABSTRACT

Interannual variability in the eastern subtropical Pacific Ocean is investigated using the Naval Research Laboratory Layered Ocean Model (NLOM). Emphasis is placed on examining the nature of westward propagating Rossby waves and their interaction with the overlying atmosphere.

Singular value decomposition (SVD), complex empirical orthogonal function (CEOF) and multivariate singular spectrum (M-SSA) analyses are used to isolate the standing and propagating response due to Rossby waves and wind stress curl (WSC) anomalies as well as their dominant frequencies of oscillation respectively. In addition to a large scale interdecadal fluctuation, two distinct forms of Rossby waves are found to exist.

SVD and CEOF analyses suggest a leading order source of variability stemming from a large scale interdecadal fluctuation. M-SSA analysis also depicts this low frequency mode, but to a lesser extent and at higher order. The modeled temporal coverage limits the extent to which this feature can be studied further.

Of primary interest in the eastern subtropical Pacific Ocean are large scale interannual wind forced Rossby wave variations. Independent M-SSA analysis of upper layer thickness (ULT) and WSC anomalies suggests a low frequency (~ 51 month period) atmospherically forced ocean response in which westward atmospheric propagation leads forced oceanic Rossby wave propagation by roughly 3 months.

In addition to this low frequency forced oceanic wave response, a distinct freely propagating biennial (~ 24 month period) oceanic Rossby wave is found to exist.

Longitude lag/time lag correlation matrices reveal phase speeds $c_r \sim 8 \text{ cm/s}$ and $c_r \sim 12 \text{ cm/s}$ for the freely propagating and forced Rossby waves respectively, both in accordance with their respective theories.

Model results and forcing are compared with TOPEX/POSEIDON altimetry and Florida State University pseudo-stresses respectively. The model compares extremely well with independent observations giving validity to the results and choice of forcing while providing substantive evidence for the ability of the ocean model to reproduce oceanic variability.

1. INTRODUCTION

Since *Stommel* (1957), and later *White and McCreary* (1974), investigated the response of the interior ocean to changes in the overlying atmosphere, numerous investigators have examined Pacific Ocean thermocline variability on time scales of seasons to decades (*Meyers* 1975, *White* 1977, 1978, *Meyers* 1979, *Kang and Magaard* 1980, *Magaard* 1983, *White et al.* 1985, *Kessler* 1990, *Qiu et al.* 1997, *White and Cayan* 2000, and references therein). An integral component of these studies focused on observing and explaining large scale westward propagating Rossby waves and their interaction with the overlying atmosphere.

Although the foundations of these studies are rooted in theory (*Stommel* 1957, *White and McCreary* 1974), *Meyers* (1975) first provided clear evidence for an ocean-atmosphere interaction by relating annual thermocline fluctuations to the annual cycle in wind stress curl (WSC) in the vicinity of the Pacific North Equatorial Current. Using an augmented data set, *White* (1977) extended the f -plane dynamics of *Meyers* (1975) arguing the thermocline variability to be strongly influenced by β -plane dynamics. In this work, *White* (1977) first suggests a westward propagating long wave, composed of a local forced response and a freely propagating response, with a phase speed twice that of nondispersive Rossby waves ($C = 2C_R$).

A few major assumptions employed by *White* (1977) include the lack of both an alongshore wind and equatorially forced, coastally propagating Kelvin waves. *Meyers* (1979) suggests these limitations are avoided if one moves to a point west of the eastern boundary layer and uses observed thermocline variations as the boundary condition

for the model. In this case, thermocline variability depends on a local Ekman pumping response as well as a westward propagating response emanating from the Eastern boundary. At the same time, the dynamics of the boundary solution, be it a local atmospheric response or an equatorial teleconnection, are not specified. The results of *Meyers* (1979) analysis suggest varying dynamics in the tropical North Pacific Ocean with thermocline displacements owing solely to Ekman pumping along 12°N while variability along 6°N is more representative of the combined Ekman pumping/Rossby wave mode. Interestingly, *Meyers* (1979) suggests larger than expected phase speeds (observed in the data) might be better understood if interaction between the annual waves and mean shear flow is allowed.

Following an observational study using inverse methods on the subject (*Kang and Magaard* 1980), *Magaard* (1983) provided a unifying discussion of previously presented annual Rossby wave data as well as new evidence for interannual mode Rossby waves. The collective results suggested only first mode annual Rossby waves dominate the North Pacific between $30\text{--}40^{\circ}\text{N}$ while variations encompassing the entire spectrum (from 5 months to 10 years) are seen between $20\text{--}30^{\circ}\text{N}$. *Magaard* (1983) found two intriguing sequences of Rossby wave energy between $20\text{--}25^{\circ}\text{N}$ and $175\text{--}130^{\circ}\text{W}$ with spectral peaks corresponding to 4 and 6.7 year periods. The westward monotonically increasing energy suggested local generation of the waves. Prior to these interannual results, the primary focus had been on annual variability.

Using a greatly augmented data set, *Kessler* (1990) revisited the annual Rossby wave question of the previous authors as well as addressing aspects of interannual variability in the North Pacific Ocean. Like previous authors, *Kessler* (1990) employed a simple quasi-geostrophic (QG) model of thermocline variations dependent upon Ekman pumping and Rossby wave radiation. *Kessler* (1990) notes the largest

interannual WSC forcing exists in mid-basin, occurring between 15-30°N and 175-110°W, while there is little annual variation over the same region. Analysis results suggested the simple QG model performed well along 5°N (in agreement with *Meyers* 1979) and between 14-18°N for annual variations. However, for interannual variations, the results are mixed with poor performance of the QG model equatorward of 15°N and relatively good performance poleward of 15°N. It should be noted, however, that this analysis focused primarily on the two strong El Niño-Southern Oscillation events of 1972 and 1982.

During the time *Kessler* (1990) was analyzing bathythermograph (BT) data, major achievements were being made with satellite observing platforms. One of the primary culminations of this feat, was the seminal work of *Chelton and Schlax* (1996) providing altimetrically derived global observations of oceanic Rossby waves. Although the filtering techniques applied to the data were aimed at representing annual Rossby waves, the work was innovative and provided some startling new results. Namely, *Chelton and Schlax* (1996) were the first to produce a set of observations providing global evidence for systematic differences between observed Rossby wave phase speeds and those predicted by standard linear theory.

The observations of *Chelton and Schlax* (1996) spawned a wide array of research aimed at understanding the discrepancies between observations and linear theory. Among these were observational and theoretical works attributing the enhanced propagation speeds seen in the data to interactions between the waves and the background mean flow (*Killworth et al.* 1997, *Dewar* 1998). In another study, the modified phase speeds are attributed to eddy dissipation which preferentially selects for a forced wave response with phase speed twice that of the damped free wave (*Qiu et al.* 1997). Of the remaining research on the subject, most is aimed at understanding the phase

speed differences by attributing them to ocean-atmosphere interactions with emphasis placed on the role of the wind in modifying the Rossby wave phase speed (e.g. *Miller et al.* 1997, *White et al.* 1998, *White* 2000). In each case, the results suggest that Rossby wave phase speed modifications from each independent process are of the right size and orientation to account for the observed discrepancies.

Although the observations of *Chelton and Schlax* (1996) were aimed at annual Rossby waves, the analytical, numerical, and observational analyses described above are not limited in scope and can be equally applied to annual or interannual Rossby waves. Thus, it is clear that a variety of mechanisms may be responsible for the differences between observed Rossby waves and linear theory. With respect to the mechanisms described above, namely dissipation, mean flow effects, and atmosphere-ocean coupling, this research deals with the latter.

Recently, evidence has emerged linking large scale atmospheric changes with changes in the underlying ocean from biennial to inter-decadal time scales (*Miller et al.* 1997, *White et al.* 1998, *Tourre et al.* 1999, *White and Cayan* 2000, *White* 2000). Of particular interest to this study, *Miller et al.* (1997) suggests interannual variability in the interior ocean to be dominated by large scale changes in the wind stress curl associated with Pacific North American pattern fluctuations in the atmosphere. Furthermore, *White et al.* (1998) reveal large scale coherent propagating patterns in both atmospheric (WSC, meridional wind stress) and oceanic (sea level height, sea surface temperature) fields in extratropical regions. *White* (2000) expanded this to include more tropical regions (10-22°N) suggesting a positive feedback loop between propagating features in the atmosphere and the ocean. The observational evidence suggests a plausible link between the atmosphere and ocean on interannual time scales.

The present study is motivated by these ongoing efforts aimed at understanding interannual variability in the North Pacific Ocean. In particular, the development of a better understanding of the interannual variability in the eastern subtropical North Pacific Ocean and the ocean-atmosphere interaction between the WSC and westward, freely propagating Rossby waves is sought. This study is not intended to refute the findings of the previous authors, but rather, to examine this common problem in an analogous but unique manner. Like many previous authors, the dynamical basis of understanding relies upon the quasi-geostrophic potential vorticity equation. However, to the best of the authors knowledge, this problem is addressed for the first time through the use of a high resolution, nonlinear numerical ocean model with realistic forcing, the results of which are analyzed using a series of related statistical techniques (empirical orthogonal function (EOF) , singular value decomposition (SVD), and multi-channel singular spectrum (M-SSA) analyses).

It will be shown that although coastally forced westward freely propagating Rossby Waves do exist over the latitude band in question (18° - 24° N), the dominant mode of interannual variability in the eastern subtropical Pacific Ocean is due to large scale fluctuations in the wind stress curl (WSC). The WSC anomalies manifest themselves in the ocean as wind forced Rossby waves with propagation speeds roughly twice that of linear theory. Additionally, the possible existence of a longer inter-decadal mode of variability is noted, but its validation and physical implications are left out of the current study.

Results from both high resolution numerical model simulations and TOPEX/POSEIDON (T/P) satellite altimetry are compared to establish the validity of the numerical model. Similarly, the wind stress used to force the model, a hybrid product using the monthly mean climatology from the *Hellerman and*

Rosenstein (HR, 1983) and the 12 hourly variability from the *European Centre for Medium-Range Weather Forecasts* (ECMWF, 1995) winds (ECMWF/HR), and the Florida State University (FSU) pseudo-stresses are compared in an effort to validate the choice of forcing used as well as isolate the effects of the wind stress curl and Ekman pumping.

The structure of this work is as follows. Section 2 presents the numerical ocean model and observational data used in this work. The methodology employed in this work is presented in section 3. Section 4 compares the numerical results with observations. Evidence for and the discussion of the subtropical eastern Pacific Ocean interannual variability is presented in section 5. Finally, a synthesis of the results and possible avenues for further research is provided in section 6. Discussion regarding a potential inter-decadal mode is left to an appendix.

2. MODEL AND DATA

2.1 Eddy Resolving General Circulation Model

The Naval Research Laboratory Layered Ocean Model (NLOM) is utilized. The primitive equation layered ocean model is a descendent of the model by *Hurlburt and Thompson* (1980) with enhanced processing and capability *Wallcraft* (1991). The vertically integrated equations used in the current version of the NLOM n -layer, finite depth, hydrodynamic model are:

$$\begin{aligned}
\frac{\partial \vec{V}_k}{\partial t} + (\nabla \cdot \vec{V}_k + \vec{V}_k \cdot \nabla) \vec{v}_k + \hat{k} \times f \vec{V}_k \\
= -h_k \sum_{l=1}^n G_{kl} \nabla (h_l - H_l) + \frac{(\bar{\tau}_{k-1} - \bar{\tau}_k)}{\rho_0} \\
+ \max(0, -\omega_{k-1}) \vec{v}_{k-1} - [\max(0, \omega_{k-1}) \\
+ \max(0, -\omega_k)] \vec{v}_k + \max(0, \omega_k) \vec{v}_{k+1} \\
+ \max(0, -C_M \omega_{k-1}) (\vec{v}_{k-1} - \vec{v}_k) \\
+ \max(0, C_M \omega_k) (\vec{v}_{k+1} - \vec{v}_k) + A_H \nabla^2 \vec{V}_k
\end{aligned}$$

$$\frac{\partial h_k}{\partial t} + \nabla \cdot \vec{V}_k = \omega_k - \omega_{k-1} \tag{1}$$

where, $k = 1 \dots n$ when referring to layers, and $k = 0 \dots n$ when referring to interfaces between layers with $k = 0$ at the surface.

The model has no-slip and kinematic boundary conditions and is solved on a C-grid (*Messinger and Arakawa* 1976) using a semi-implicit scheme for finite depth simulations, and an explicit scheme for reduced gravity experiments. The model includes a free surface and the barotropic mode. A more detailed description of the model is given by *Wallcraft* (1991) and *Shriver and Hurlburt* (1997).

Although thermodynamic versions of the model exist, only results from a single hydrodynamic simulation are presented here. The only forcing used in this experiment is the applied wind stress fields, a hybrid wind stress composed of *Hellerman and Rosenstein* (1983, HR) monthly climatology and the *European Centre for Medium-Range Weather Forecasts* (1995, ECMWF) 1000 mb twelve-hourly winds. The ECMWF/HR hybrid wind stress data are constructed by replacing the ECMWF climatological mean for 1981-1996 with that of the HR data set. This is done in an effort to produce a wind stress with both realistic variability and climatology. The ECMWF/HR pseudo-stress data is then multiplied by a constant drag coefficient, $C_D = 1.5 \times 10^{-3}$, and the air density at sea level, $\rho_a = 1.2 \text{ kg/m}^3$, to obtain the wind stress.

A realistic coastline and bottom topography are included by utilizing a modified version of the 1/12° ETOP05 (*NOAA* 1986) bottom topography with extensive corrections to the geometry of the Hawaiian Islands and several semi-enclosed seas in the Western Pacific Ocean. The ETOP05 data set is interpolated to the model grid and twice smoothed using a 9-point smoother. The smoothing is designed to reduce energy generation at smaller scales.

The 200 m isobath is used to determine the model boundary and represents the shelf break as well as the minimum depth in the model. The only exceptions to this are regions where shallower depths are needed to connect semi-enclosed seas to the

Pacific Ocean (e.g. the Tsugaru, Tsushima and Soya Straits connecting the Sea of Japan to the Pacific Ocean).

The maximum depth of the model is 6500 m. In the finite depth simulations, seamounts and other rough bottom topography are confined to the lowest layer. As a result, numerical difficulties arising when moving interfaces and sloping topography intersect are removed (*Hurlburt and Thompson 1980*). The two primary reasons for including topographic features are to force the lowest layer (abyssal) flow to follow the f/h contours and to regulate baroclinic instability. The confinement of topography to the lowest layer has negligible impact on these. Additionally, flow through straits and shallow sills is constrained to small values below the sill depth.

The model domain is the Pacific Ocean from 20°S to 62°N and 109.125°E to 77.203135°W with a horizontal resolution of $1/16^\circ \times 45/512^\circ$ (latitude \times longitude). Since the model boundaries at 20°S and Indonesia are treated as closed, there is no Indonesian throughflow and no contribution from the global thermohaline circulation.

The model outputs data every 3.05 days. However, since the time scales of interest here are interannual, monthly means are created and examined from January 1981 through December 1996. The basic large scale model phenomenology is the same as that of *Jacobs et al. (1994)*, *Metzger and Hurlburt (1996)*, *Hurlburt et al. (1996)*, *Mitchell et al. (1996)*, *Leonardi et al. (2000)* and *Murray et al. (2000)*. As such, a detailed description of the basin scale flow is not provided here. The interested reader is directed to the previous studies.

2.2 TOPEX/Poseidon Altimetry

Of the many variables essential to examining oceanic variability, two of the most important include the structure of the sea surface height (SSH) and the surface oceanic

current velocity fields. Although many observations exist over the world's oceans for both of these fields, the best such platform, for comparison with modeled results, that currently exists is the SSH data derived from the TOPEX/Poseidon (hereafter T/P) exact repeat mission (ERM). Not only does the T/P data provide comprehensive and nearly continuous global ocean SSH, but the SSH data can also be used to calculate geostrophic global surface velocity fields.

Two different types of T/P data are readily available: regularly gridded and along track data. The along track data allows for adequate resolution of smaller time and length scale mesoscale/synoptic variability. The gridded product is an objectively mapped version of the along track data. Since the satellite data used in this work is aimed at validating the oceanic features simulated by the model, the gridded product is not only adequate for our purposes, but also easier to use. As such, the along track product will not be discussed except in its relation to the production of the gridded product, which will be discussed next.

The T/P data are derived from the geophysical data records (GDR's) provided on cdrom by *Archiving, Validation, and Interpretation of Satellite Oceanographic data* (1992, AVISO). One-second average SSH values are used globally for cycles 11 through 234, corresponding to the time between January 1993 and January 1999. Since the T/P data are available over land and ocean, quality control procedures set by the T/P science working team (*Archiving, Validation, and Interpretation of Satellite Oceanographic data* 1992) were applied. Additionally, suggestions made by *Fu et al.* (1994) regarding geophysical corrections are applied. Oceanic tides are removed through the use of the CSR 3.0 tidal model (*Eanes and Bettadpur* 1995). All other standard corrections are applied (i.e. ionospheric, dry/wet tropospheric, sea state bias corrections, etc.; *Callahan* 1993).

The measurement position of the T/P measurements is not fixed in space or time. In an effort to minimize the effects of along track sampling variation, the tracks were collocated to a fixed position with a simple linear interpolation using a perpendicular bisector approach (*Cheney et al.* 1983a) between the two closest data points to cycle 18 repeat tracks. Across track variations in the satellite path (which can be as large as 1 km) are minimized by applying the Basic and Rapp mean sea surface model (*Cheney et al.* 1983b).

After all of the corrections were applied, the temporal mean for the data record (cycles 11-234) is calculated for each reference point in the collocated SSH data and removed from the individual cycles. The resulting data field comprises the along track SSH data. The gridded data product is then produced by taking the residual SSH signal from the along track data and mapping it to a $1^{\circ} \times 1^{\circ}$ latitude/longitude grid using Gaussian interpolation with a full-width half maximum of 150 km and a search radius of 200 km.

3. METHODOLOGY

3.1 Decimating the NLOM Data

High spatial and temporal resolution in the numerical model is required to properly represent the mesoscale oceanic features. This results in an extremely large data set in which proper statistical analyses are often difficult to perform in a timely and efficient manner. As such, a method is employed in the current research in which the model data are decimated from their original $1/16^\circ \times 45/512^\circ$ grid to a more economical $1^\circ \times 1^\circ$ grid. In addition to reducing the size of the data matrix involved in the computations, this decimation procedure also puts the NLOM data on a grid that allows direct spatial comparison with gridded satellite altimeter data, e.g. Topex/Poseidon.

The decimation procedure is simple in nature. It involves extracting the given data (u, v, h, ssh, etc.) on each grid point evenly spaced one degree apart and residing on integer numbered lines of longitude and latitude. For the latitudinal direction, this is exactly represented since the latitudinal locations are evenly spaced beginning at 20°S latitude. The longitudinal grid, on the other hand, does not generally reside on integer lines of longitude. This is due to the zonal grid spacing being $45/512^\circ$ rather than $1/16^\circ$. Thus, to obtain the data at local integer lines of longitude, a simple average is made of the two points surrounding the longitude desired, one to the west and the other to the east.

One may wonder whether or not this decimation procedure would be adequate to

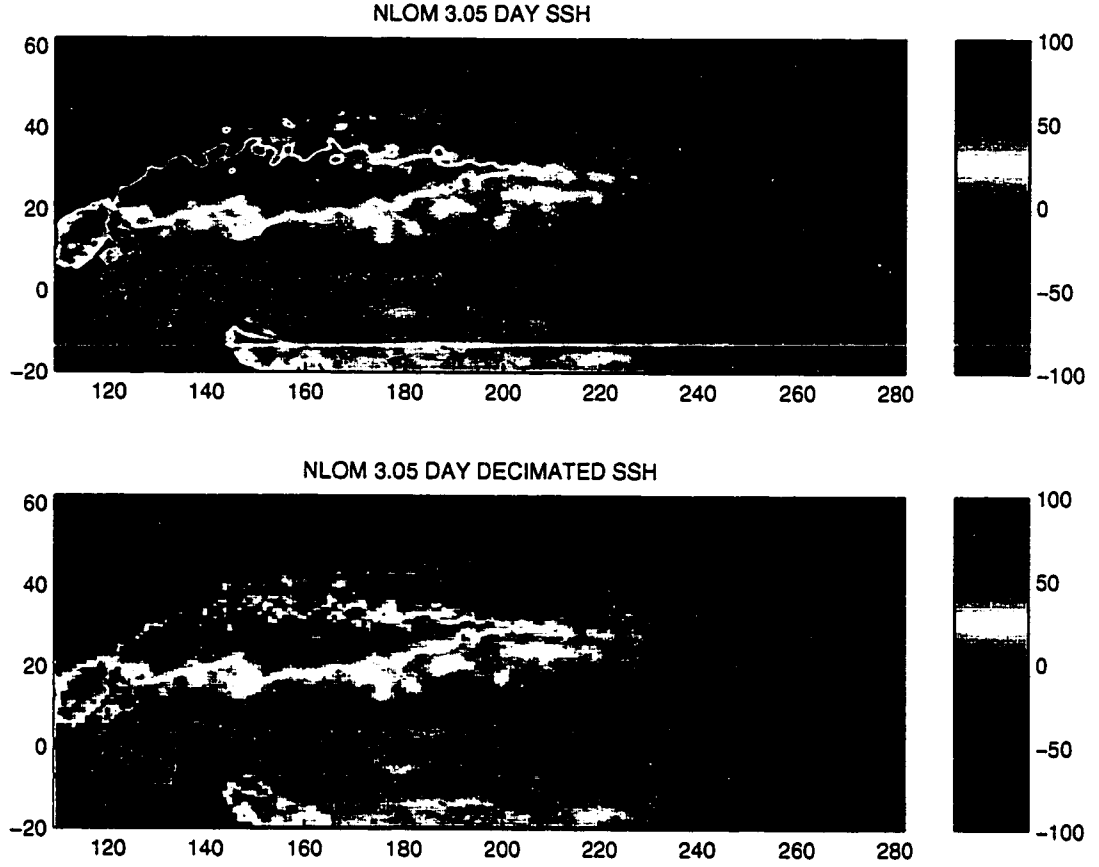


Figure 1: Comparison of the original sea surface height (SSH) data (top) and the decimated data (bottom) from the Naval Research Laboratory (NRL) Layered Ocean Model (NLOM). The data are a snapshot of the 3.05 day output from the high resolution model. Original data have a grid spacing of $1/16^\circ \times 45/512^\circ$ (latitude \times longitude) while the decimated data have a grid spacing of $1^\circ \times 1^\circ$. Units for SSH are *cm*.

reduce the number of data points while still retaining the mesoscale features of the circulation. Comparison of the decimated data (figure 1, bottom) with the original data (figure 1, top) reveals close agreement on both the large and mesoscale. Clearly, the decimation process reduces the size of the data matrix greatly (from ~ 2.6 million independent data points per time step to $\sim 14,400$ data points per time step) while retaining the key elements to the mesoscale structure.

As a secondary check, it is necessary to check whether the decimation has adverse

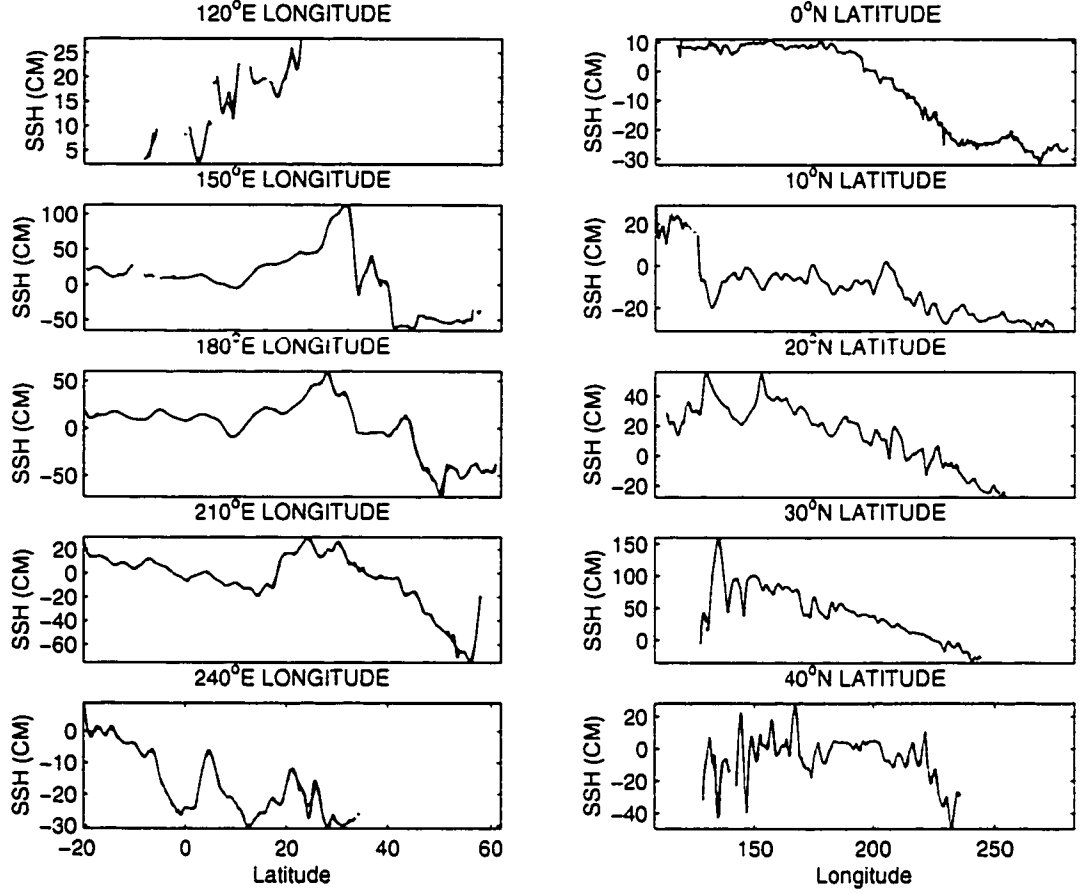


Figure 2: Comparison of the original sea surface height (SSH) time series with the decimated data time series along representative longitudinal (left column) and latitudinal (right column) transects. SSH data are plotted every 3.05 days with units of *cm*.

effects along local lines of longitude or latitude. The model data along representative longitudinal and latitudinal transects (figure 2) indicates that although the decimation has the effect of smoothing extremely high wavenumber ($O(1/16^\circ)$) features, The large scale structure and variability remain intact. Thus, the decimation procedure reveals no substantial effects on the representation of both the large- and meso-scale flow. It should also be noted that since the decimation process is purely spatial, there are no ill effects on the time series at each individual location.

3.2 Empirical Orthogonal Function (EOF) Analysis

Both satellite altimeters and numerical ocean models provide spatially and temporally robust data sets for examining the worlds oceans. However, the relative amount of information contained in the data is substantially smaller than the actual physical amount of data itself. As such, it becomes important to reduce the data set to a manageable size while retaining all of the important physics of the problem being examined. One way to do this is through empirical orthogonal function (EOF) analysis (additionally known as principle component analysis).

EOF analysis is essentially a statistical method in which a large data set is broken down into its most important constituents, or modes, of variability. Thus, it is a method in which the spatial and temporal variability of the data set is reduced to the fewest number of spatial patterns representing standing modes that vary in time according to a temporal amplitude function (the time series).

There are two major shortcomings to EOF analysis. First, unlike linear regression analysis (LRA) in which the basis functions for the system being studied are set *a priori*, EOF analysis allows the data to determine its own basis functions under the strict criterion that each individual function must hold the maximum variance and be mutually orthogonal to all remaining functions (*Mitchum* 1993). Thus, there is no guarantee in EOF analysis that the functions represent physical modes of variability of the original data. The second shortcoming of EOF analysis is that although it can be used to detect propagating features, it is designed to detect large amounts of variance associated with standing waves (*White et al.* 1987, *Shriver et al.* 1991).

The first shortcoming can not be avoided, but careful inspection of the data and results allows one to distinguish between physical and non-physical results. The second shortcoming is averted if one uses complex empirical orthogonal function (CEOF)

analysis. Since traveling waves are also of interest here, it is important to discuss the differences between CEOF and EOF analyses.

CEOF and EOF analyses are similar in that they reduce the variability into a greatly compressed format. However, instead of containing only the standing modes, CEOF's also contain the traveling modes of variability. This allows one to distinguish between the two and capture the variability of large scale propagating wave-like features. For oceanography, the wave-like disturbances most of interest are baroclinic Rossby waves. Since EOF analysis is just a specific case of CEOF analysis, the remainder of this section will focus solely on the mechanics of CEOF's.

For data with two spatial dimensions and a temporal dimension, one can construct a two dimensional array, $d(x_m, t)$, such that $d(x_m, t) = D(\vec{r}_m, t)$, where \vec{r}_m is the two dimensional position vector, $\vec{r}_m = (x_m, y_m)$, and t the time index. The data field, $d(x_m, t)$, can then be broken down into its Fourier components as

$$d(x_m, t) = \sum_{\omega} a_m(\omega) \cos(\omega t) + b_m(\omega) \sin(\omega t). \quad (2)$$

Here, $a_m(\omega)$ and $b_m(\omega)$ are the Fourier coefficients.

This can also be represented in the complex notation as

$$D_m = \sum_{\omega} c_m(\omega) e^{-i\omega t} \quad (3)$$

where $c_m(\omega) = a_m(\omega) + ib_m(\omega)$.

Inserting $c_m(\omega)$ into equation (3) and expanding yields

$$D_m = \sum_{\omega} [a_m(\omega) \cos(\omega t) + b_m(\omega) \sin(\omega t)] + i[b_m(\omega) \cos(\omega t) + a_m(\omega) \sin(\omega t)]$$

$$= u_m(t) + i\hat{u}_m(t). \quad (4)$$

Here, the imaginary part, $\hat{u}_m(t)$, of D_m is just the Hilbert transform of the real part, representing the original data, $u_m(t)$, phase shifted in time by $\pi/2$ ($-\pi/2$) for the positive (negative) frequencies but without a change in magnitude.

Next, we perform the standard (non-complex) EOF analysis on the complex data. The result will be a set of eigenvalues ($\lambda_i, i = 1, 2, \dots, n$) and eigenvectors (the temporal functions) with the normalized eigenvalues representing a relative (or percent) variance for each mode.

The complex data can then be reconstructed by summing the spatial and temporal eigenfunctions as:

$$\begin{aligned} D_m &= \sum_l [SF]^* [TF] \\ &= \sum_l [S_l(m)e^{i\theta_l(m)}]^* [R_l(t)e^{i\phi_l(t)}] \end{aligned} \quad (5)$$

where, SF and TF correspond to the spatial and temporal functions respectively, $S_l(m)$ and $R_l(t)$ the spatial and temporal amplitude functions, $\theta_l(m)$ and $\phi_l(t)$ the spatial and temporal phase functions, and $*$ denotes the complex conjugate.

It is clear from equation (5) that the spatial and temporal amplitude functions are simply:

$$\begin{aligned} S_l(m) &= \sqrt{(SF)(SF)^*} \\ R_l(t) &= \sqrt{(TF)(TF)^*} \end{aligned} \quad (6)$$

and the spatial and temporal phase functions as:

$$\begin{aligned}\theta_l(m) &= \arctan \left[\frac{\Im(SF)}{\Re(SF)} \right] \\ \phi_l(t) &= \arctan \left[\frac{\Im(TF)}{\Re(TF)} \right].\end{aligned}\tag{7}$$

Above, $\Re(X)$ and $\Im(X)$ represent the real and imaginary parts of the given function respectively, and $*$ is again used to denote the complex conjugate.

Finally, the wavenumber, \vec{k} , and frequency, ω , can be obtained from the spatial and temporal phase functions respectively as:

$$\begin{aligned}\vec{k} &= \frac{\partial \theta_l(m)}{\partial \vec{x}} \\ \omega &= \frac{\partial \phi_l(t)}{\partial t}\end{aligned}\tag{8}$$

for $\vec{x} = (x, y)$ (*Shriver et al.* 1991).

Thus, CEOF analysis breaks the original data down into spatial and temporal modes. The spatial mode provides the spatial pattern associated with a given mode while the temporal mode provides information on how the amplitude of the associated spatial mode changes in time (its variability). Together, the two provide a complete representation of the variability of the given mode. Additionally, by knowing the amplitude and phase of the variability one can distinguish propagating features in the circulation (e.g. Rossby waves) and determine their associated phase speeds. A summation of the individual modes returns the spatial and temporal variability of the original data. Thus, examining only a few of the modes does not provide a full representation of the data, but contains the majority of the variance needed to understand the dynamics.

3.3 Singular Value Decomposition (SVD) Analysis

Computationally, EOF analysis (described in the previous section) requires one to use the covariance matrix. For large, regularly spaced data fields, such as those often used in geophysical applications, calculation and use of the covariance matrix becomes computationally expensive to create and use. One solution is to use singular value decomposition (SVD) analysis rather than EOF analysis (*Kelly 1988, Emery and Thomson 1997*).

Like EOF analysis, SVD analysis breaks the data down into its fundamental modes. However, unlike EOF analysis, it does not require the use of the covariance matrix and provides a single step operation for solving the eigenvalue problem. Additionally, many statistical packages provide a SVD routine (e.g Matlab©, IDL©, Linpack©).

SVD analysis is based on the linear algebra idea that a given $M \times N$ matrix \mathbf{D} can be written as the product of three matrices:

$$\mathbf{D} = \mathbf{U} \begin{pmatrix} s_1 & & & \\ & s_2 & & \\ & & \ddots & \\ & & & s_N \end{pmatrix} \mathbf{V}^T \quad (9)$$

where, \mathbf{U} , \mathbf{S} , and \mathbf{V} are $M \times M$ column orthogonal, $M \times N$ diagonal with zero or positive elements, and $N \times N$ orthogonal matrices respectively.

In the case of modeled or altimetric data, the data matrix \mathbf{D} contains M rows of spatial points and N columns of temporal data, while the scalar values of matrix \mathbf{S} represent the singular values of \mathbf{D} and are sorted in descending magnitude as in EOF

analysis. Matrices \mathbf{U} and \mathbf{V} are called the left and right singular vectors respectively.

Matrix \mathbf{U} represents the mutually orthogonal eigenvectors of the problem. For EOF analysis it is also necessary to obtain eigenfunctions describing the temporal variability of the individual modes. This requires a matrix \mathbf{A} satisfying:

$$\mathbf{D} = \mathbf{U}\mathbf{A}^T \quad (10)$$

which by equation (9) is simply:

$$\mathbf{A} = \mathbf{V}\mathbf{S}. \quad (11)$$

Thus, using the SVD method, one can obtain the same results (to within roundoff) as from traditional EOF analysis using the covariance matrix (*Emery and Thomson 1997*).

An increasingly popular research technique is to perform SVD analysis on the cross covariance matrix of two fields (*Wallace et al. 1992, Cheng and Dunkerton 1995, Leuliette and Wahr 1999*), the net effect of which is to isolate coupled patterns between two geophysical fields and their associated time series¹. An in depth review of the method can be found in *Bretherton et al. (1992)* the highlights of which (adapted from *Cheng and Dunkerton (1995)*) will be outlined below.

As was stated above, SVD analysis of the covariance matrix of an individual field is equivalent to that of the field itself. It should be intuitive, then, that the SVD analysis of the cross covariance matrix of two fields should provide the dominant

¹It should be noted that there is no guarantee that the isolated response is coupled. The technique actually finds responses between the two fields that act in similar spatial and temporal manners. As such, it may be more appropriate to consider fields to act as a parallel rather than coupled response. However, for the purposes here, the term coupled will be used to describe the isolated response.

coupled modes of variability between the two fields. Consider “left” and “right” data fields $\mathbf{H}(x, t)$ and $\mathbf{W}(x, t)$ representing the thermocline depth and the wind stress curl respectively. Although the matrices need not be the same size, for the sake of discussion let us assume that each field contains N spatial grid points and T temporal points such that the data fields are $N_h \times T$ and $N_w \times T$ matrices respectively.

The goal of SVD analysis is to determine N_h and N_w dimensional orthogonal vectors $\mathbf{u}_k (k = 1, \dots, N_h)$ and $\mathbf{v}_k (k = 1, \dots, N_w)$ for $\mathbf{H}(x, t)$ and $\mathbf{W}(x, t)$ respectively such that the covariance between the projections of $\mathbf{H}(x, t)$ on \mathbf{u}_k and $\mathbf{W}(x, t)$ on \mathbf{v}_k , represented as

$$\frac{1}{T}(\mathbf{u}_k^T \mathbf{H})(\mathbf{v}_k^T \mathbf{W})^T, \quad (12)$$

is maximized subject to the constraint that $\mathbf{u}_k \mathbf{u}_k^T = 1$ and $\mathbf{v}_k \mathbf{v}_k^T = 1$.

The SVD analysis reduces the problem to the product of three matrices \mathbf{U} , \mathbf{S} , and \mathbf{V} as in equation (9), where in this case \mathbf{D} represents the covariance matrix

$$\mathbf{C}_{hw} = \mathbf{D} = \mathbf{U} \mathbf{S} \mathbf{V}^T. \quad (13)$$

Since the matrices \mathbf{U} and \mathbf{V} are uniquely defined, the original data fields can be decomposed (following the logic in equations (10) and (11)) as

$$\mathbf{A} = \mathbf{H}^T \mathbf{U} \quad (14)$$

$$\mathbf{B} = \mathbf{W}^T \mathbf{V}. \quad (15)$$

Above, the column vectors in matrices \mathbf{A} and \mathbf{B} represent the time series of the

expansion coefficients defined by projecting the left (right) field onto the left (right) singular vectors. Hence, a pair of singular vectors combined with their respective time series defines a mode of variability with the added constraint that a mode in the left field is correlated only with the same mode in the right field.

Following *Bretherton et al.* (1992), one can also define correlation and covariance maps. Letting $r[f(t), g(t)]$ denote the correlation coefficient between the two time series $f(t)$ and $g(t)$ we can define the k th left homogeneous and heterogeneous correlation maps as follows. The k th left homogeneous correlation map is defined to be the vector $r[\mathbf{H}, \mathbf{A}]$ of correlations between the gridpoint values of the left field and the k th left expansion coefficient, and is generally a good indicator of the geographic localization of the covarying part of the left field, \mathbf{H} . The k th left heterogeneous correlation map is defined to be the vector $r[\mathbf{H}, \mathbf{B}]$ of correlations between the gridpoint values of the left field and the k th right expansion coefficient, and is a good indicator of how well the right expansion coefficient can be used to predict the grid points in the left field. Similar analysis holds for the right homogeneous and heterogeneous correlation maps.

Finally, since the amount of variance described in a given mode is also of interest, a quantitative measure of the total covariance explained by a single pair of patterns (σ_k^2) is desired. The amount of total squared covariance for an individual mode (denoted here as the squared covariance fraction, SCF) is proportional to the square of its singular value

$$SCF_k = \frac{\sigma_k^2}{\sum_{l=1}^R \sigma_l^2} \quad (16)$$

where $R = \min(N_h, N_w)$.

Before closing, it is necessary to discuss a few of the caveats of SVD analysis. Like EOF analysis, SVD analysis has the ability to produce modes of variability that are purely mathematical in nature and have no physical basis in the real world (*Mitchum* 1993). It is wise to understand the physics of the problem at hand prior to interpretation of the results. Of additional concern, however, is that although large contributions to the SCF generally describe modes in which the temporal coefficients **A** and **B** are highly correlated, the SCF may also be large for a given mode if either **A** or **B** are substantially large independent of the other (*Leuliette and Wahr* 1999). The two caveats above suggest extreme caution when interpreting the SVD results.

3.4 Multi-channel Singular Spectrum Analysis (M-SSA)

Mathematically, multi-channel singular spectrum analysis (M-SSA) is identical to extended empirical orthogonal function analysis (EEOF, *Preisendorfer* 1988, *Allen and Smith* 1996). Here, the choice of nomenclature is used to alleviate confusion with standard EOF analysis. M-SSA works in a similar manner as standard EOF (or alternatively principal component) analysis. In M-SSA, use of the lagged covariance matrix (as opposed to the plain covariance matrix in EOF analysis) has the added benefit of allowing the user to better extract periodic signals which persist in time.

Following *Allen and Robertson* (1996), M-SSA can be described with respect to traditional EOF analysis using a sliding window example. EOF analysis is described as sliding a narrow and long window across the input data and identifying high variance spatial (EOF's) or temporal (principal components, PC's) patterns of variability. In M-SSA, however, standard EOF techniques are generalized and a long, scalable window is applied to the data to extract persistent patterns of lagged variability. Here, scalable means that the window width is user defined dependent upon the problem.

In the case of standard EOF analysis, the covariance matrix is supplied as the input. In M-SSA, the original data matrix is supplied along with M copies of itself. Standard SVD is then applied to the new data matrix, resulting in two orthonormal vectors representing the EOF's and reduced principal components (RPC's) of the M-SSA technique. Here, the RPC's represent the principal components but are of reduced length due to the lagged analysis.

Since standard EOF analysis is just a special case ($M = 1$), the mathematical details of M-SSA are left out. Instead, the reader is encouraged to consult the discussion of EOF's in section 3.2 and the broad body of literature on M-SSA (e.g. *Vautard et al.* 1992, *Keppenne and Ghil* 1992, 1993, *Allen and Robertson* 1996, *Allen and Smith* 1996, and references therein).

4. MODEL/DATA COMPARISON

Numerical ocean models are powerful tools that can be used to understand the fundamental dynamics of the ocean circulation. Examination of the governing equations of motion for a fluid suggest the primary dynamical response of the ocean can be understood by modeling the terms that should have the largest response (in terms of scale analysis). The remaining terms, although important in many respects, may be neglected if one wishes only to understand the leading order dynamics. Thus, unlike real observations, numerical models allow researchers to model the fundamental processes involved in the circulation and isolate the dynamical response due to the individual components (e.g. wind forcing, planetary motion, etc.).

One caveat when using ocean models, however, is that although efficacious, the response of the ocean may exist for the wrong reasons. Namely, the physics behind the response may not be realistic or worse, the response may arise from numerical errors. As such, it is important to compare the model being used with observational results to ensure the physics behind the forcing and output terms represent something that is not only physically realistic, but also something that agrees with observations.

The goal of this section is to compare the Naval Research Laboratory (NRL) Layered Ocean Model (NLOM) with a variety of observations in an effort to validate both the forcing used and the model results themselves. First, since the hydrodynamic nature of the model relies solely on the wind stress as the driving force, it is important to determine whether the winds used to force the model agree with other independent wind sets. Second, the modeled sea surface height (SSH) is compared

with observational SSH obtained from the Topex/Poseidon satellite altimeter. The two comparisons together provide substantive evidence for the validity of the model and the wind stress used to force the model.

4.1 Wind Comparisons

The model used in this study was forced by the 12 hourly 1000 mb winds from the *European Centre for Medium-Range Weather Forecasts* (1995) with the monthly means replaced by the *Hellerman and Rosenstein* (1983) monthly climatology, hereinafter referred to as the ECMWF/HR hybrid winds. For comparison purposes, the Florida State University pseudo stresses (FSU, *Stricherz et al.* 1992, 1997) will be used to examine the reliability of the modeled forcing to observed winds. For brevity, only the relationship between the zonal wind stress components are compared here. *Hundermark et al.* (1999) examined the two products in detail noting differences in large scale trends and regional scale features. However, aside from the long term trends and the few localized features, the results indicate reasonable agreement between the large scale spatial features and the interannual variability.

The most efficient way to examine the two products without reproducing the results of *Hundermark et al.* (1999) is to perform an empirical orthogonal function (EOF) analysis on the two data sets independently and compare the resultant spatial and temporal patterns. The mathematical details of the EOF analysis are provided in section 3.2. Prior to applying the EOF analysis, the two data sets must be preprocessed to remove the large scale differences mentioned above and to ensure the fields are comparable.

The first task is to ensure that the data fields reside on the same grid. The result, a $2^\circ \times 2^\circ$ longitude \times latitude grid spanning $124\text{--}282^\circ\text{E}$ and $19^\circ\text{S--}29^\circ\text{N}$, is achieved by

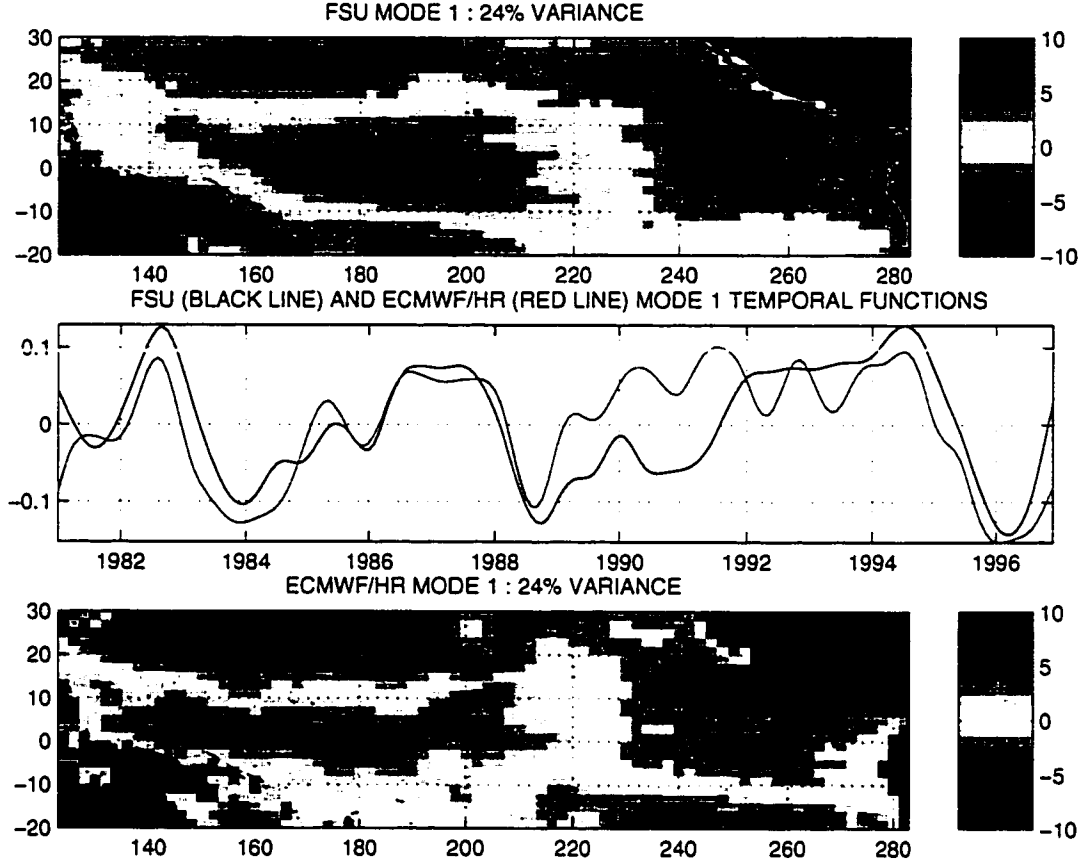


Figure 3: First mode EOF spatial amplitude functions of the filtered FSU pseudo (top) and ECMWF/HR hybrid wind (bottom) zonal stresses (τ_{xz}) along with their associated principal components (middle, FSU=black line, ECMWF/HR=red line). Both modes represent 24% of the overall variance.

extracting the ECMWF/HR and FSU winds corresponding to an overlapping grid between the two products. Second, monthly means are created spanning 1981-1996 inclusive. The data are then detrended in time using a linear fit, effectively removing the long term mean in the process, and then normalized by their standard deviations in an effort to preserve the overall variance. As a final step, a 15-point Hanning filter (described in appendix B) is applied to retain the interannual time scales but to remove annual or higher frequency variability.

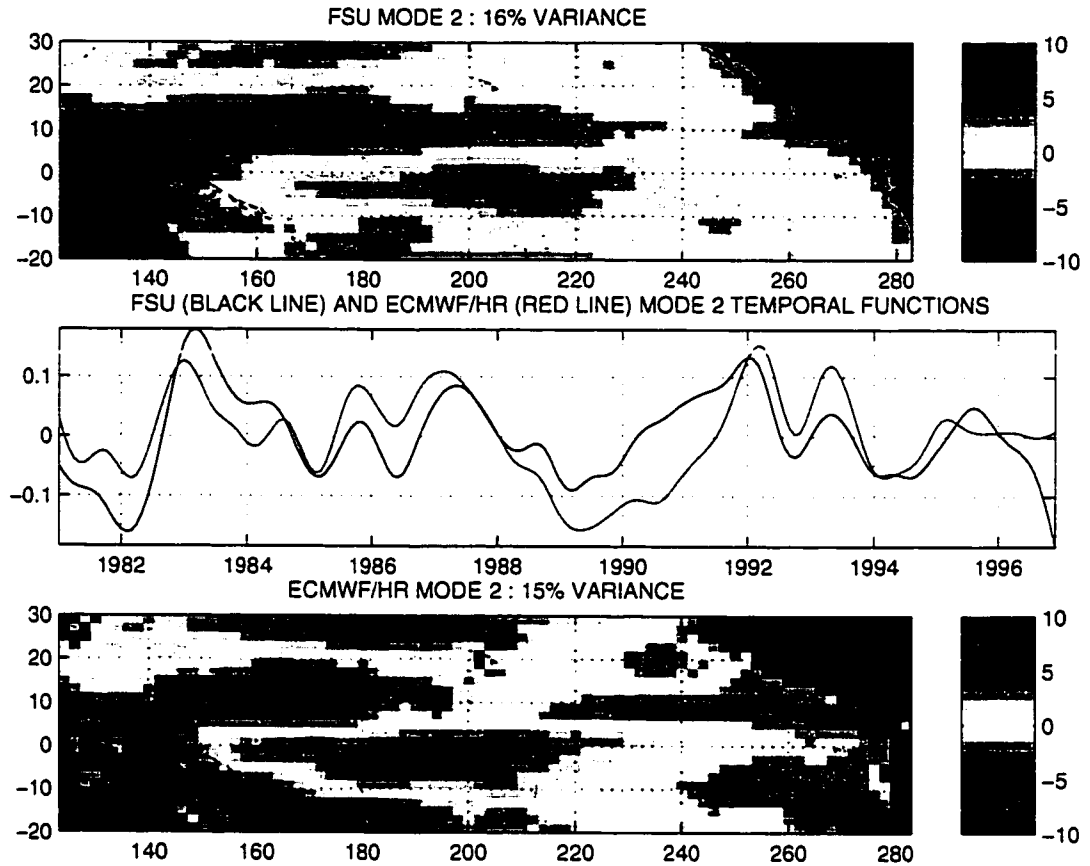


Figure 4: Second mode EOF spatial amplitude functions of the normalized FSU pseudo (top) and ECMWF/HR hybrid wind (bottom) zonal stresses (τ^z) along with their associated principal components (middle, FSU=black line, ECMWF/HR=red line). Both modes represent 24% of the overall variance.

The EOF analysis reveals reasonable agreement between the ECMWF/HR and FSU products. However, substantial differences exist in the southeast Pacific Ocean near 20°S. This is likely due to the lack of adequate ship observations (which the FSU winds rely upon) in the southeast Pacific Ocean. Additionally, temporal differences in both EOF modes 1 and 2 (see below) likely represent a propagating feature that has been split between the two modes. The differences, although noteworthy, are not a major concern here since the focus of this research is on the midlatitude North

Pacific Ocean.

The first mode EOF (figure 3) exhibits the classical ENSO signature with spatial peaks along the equator in the vicinity of the dateline. As the temporal functions show, these represent the weakening (or reversal) of the equatorial trade winds associated with the onset of El Niño. The two time series are essentially identical with small variations at frequencies higher than interannual. Both analyses represent 24% of the overall variance in the data set. Similarly, mode 2 (figure 4), representing 16% and 15% of the variance for the FSU and ECMWF/HR products respectively, also exhibits spatial and temporal patterns generally associated with ENSO. The two primary modes in each data set are likely a coupled mode that represents the standing and propagating modes of ENSO and encompass roughly 40% of the variance collectively.

In addition to examining the interannual fluctuations, it is beneficial to compare the two unfiltered data sets in an effort to confirm that the variability is not coming from separate sources. This is done in a manner analogous to the results shown above with the exception that the data is not filtered in time. The results are striking. Unlike the results above in which the dominant mode of variability was interannual in nature, the unfiltered EOF's suggest the dominant mode of variability to be associated with the annual migration of the trade winds. The spatial patterns (figure 5) for both data sets are nearly identical. Similarly, the temporal patterns are highly correlated also. A purely sinusoidal annual signal is not clearly depicted, but this is probably attributed to higher frequency variability and from fluctuations arising from ENSO and monsoon circulations in the western Pacific (*Waliser and Gautier* 1993). However, the variance associated with the dominant unfiltered mode is 60% higher in the ECMWF/HR product ($\sim 16\%$) than in the FSU product ($\sim 10\%$). Again, this is likely due to

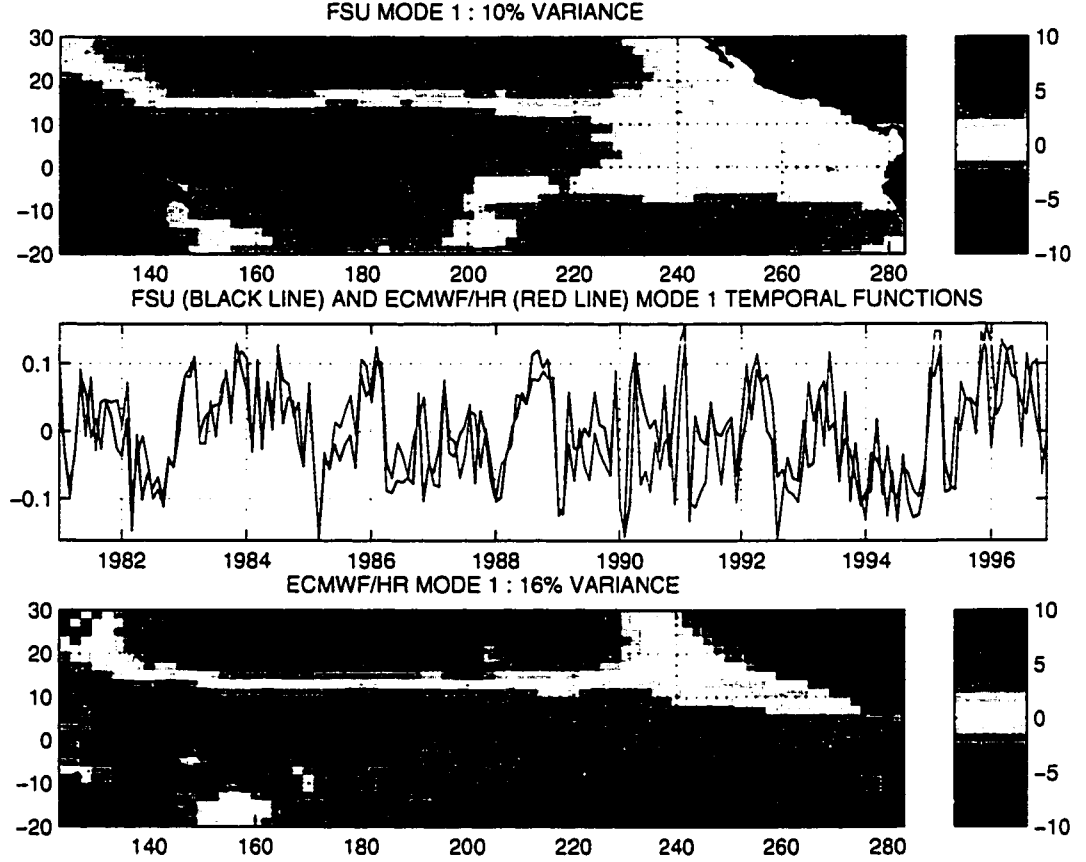


Figure 5: First mode EOF spatial amplitude functions of the unfiltered FSU pseudo (top) and ECMWF/HR hybrid wind (bottom) zonal stresses (τ^x) along with their associated principal components (middle, FSU=black line, ECMWF/HR=red line). Each mode represents 16% and 15% of the overall variance for the FSU and ECMWF/HR winds respectively.

the coupled nature of the higher modes in both data sets. All in all, however, it is clear that the ECMWF/HR wind stress is a reasonable choice in forcing the model, especially if we wish to obtain the interannual signals.

4.2 Sea Surface Height (SSH) Comparisons

Empirical Orthogonal Function (EOF) Analysis

In addition to ensuring that the winds used to force the model are reasonable, it is important to compare the model response with observations. Given the spatial extent of the model, the best observational choice for comparison with the model is satellite derived sea surface height (SSH) measurements from TOPEX/POSEIDON (T/P). The T/P data are described in detail in section 2.2 and the references therein.

Strict comparison between the modeled SSH and T/P SSH is impossible based on the sampling intervals of each, 3.05 and 9.92 days for the model and T/P data respectively. However, assuming that dramatic changes in the large scale flow patterns are resolvable (temporally) by both data sets, it is sufficient to compare the monthly mean SSH over the time frame in which the model and T/P data overlap, in this case between January 1993 and December 1996.

For both the model and T/P, the data are first extracted such that they reside on the same grid. The region of overlap between the model and T/P data spans 20°S-60°N and 124°-282°E. One major difference over this region is that the T/P data cover the coastal areas as well as the Gulf of Mexico, whereas the model boundary is defined by the 200 m isobath and the Gulf of Mexico is set to land values. Thus, in order to ensure a direct comparison, the T/P data are set to missing for any location in which model data are lacking.

After creating the monthly means on the same grid as described above, the data are then bin averaged to form $2 \times 2^\circ$ bins. The primary reason for this is to smooth the data spatially. The secondary reason is to reduce the size of the matrix involved in the statistical computations. Following the bin averaging, the data are detrended

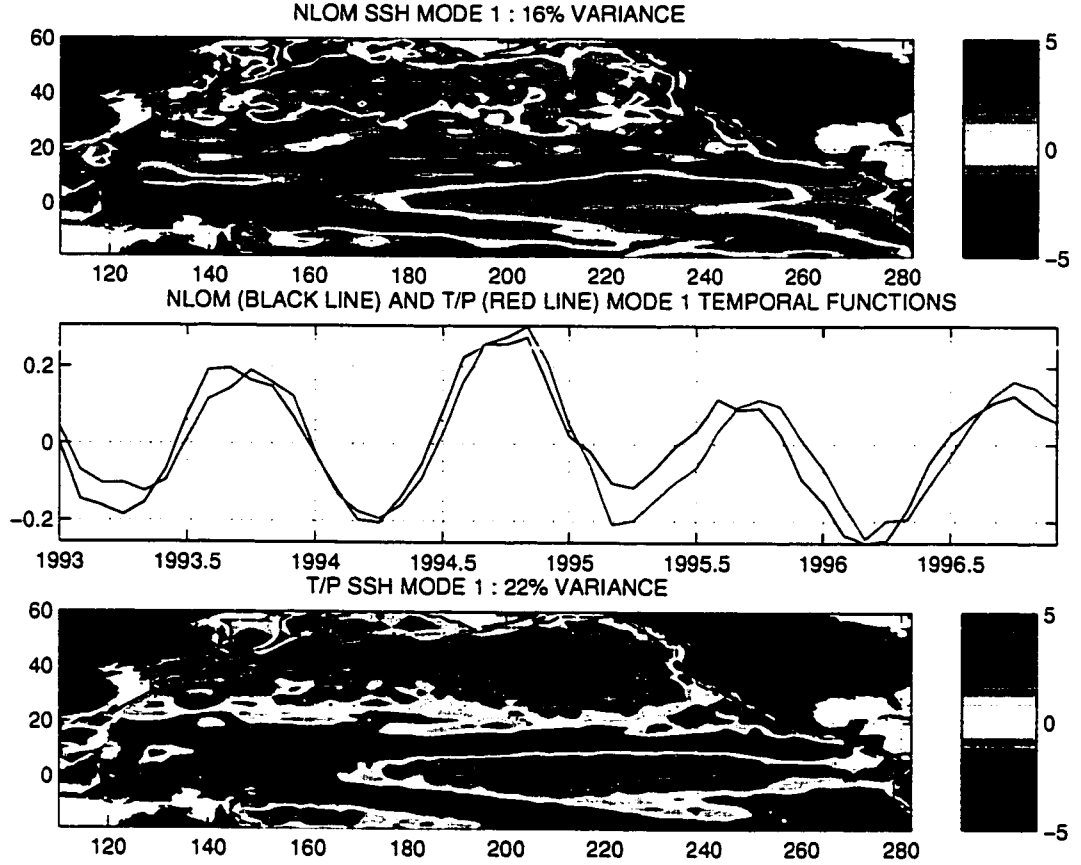


Figure 6: First mode EOF spatial amplitude functions of the unfiltered NLOM (top) and TOPEX/POSEIDON (T/P, bottom) sea surface height (SSH) along with their associated principal components (middle, NLOM=black line, T/P=red line). Each mode represents 16% and 22% of the overall variance for the NLOM and T/P SSH respectively.

in time, normalized to produce a variance conserving matrix, and individual EOF analyses are performed on the respective data sets.

Similar to the case with the wind forcing, the comparisons between modeled and observed SSH are striking (figures 6, 7, and 8). In each of the first three modes, the spatial and temporal functions reveal a strong resemblance between the model and T/P SSH fields. Modes 1 and 2 are related for each data set, clearly reveal the annual cycle, and account for 28% and 32% of the overall variance for the modeled

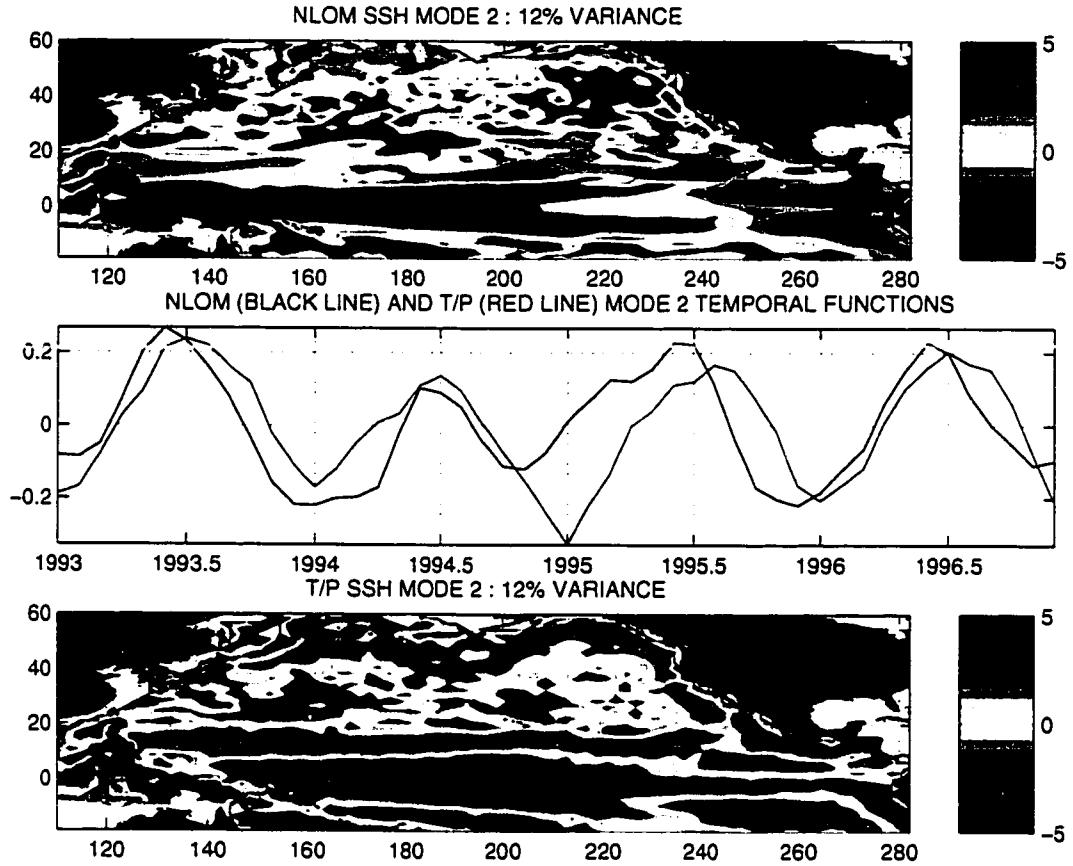


Figure 7: Second mode EOF spatial amplitude functions of the unfiltered NLOM (top) and TOPEX/POSEIDON (T/P, bottom) sea surface height (SSH) along with their associated principal components (middle, NLOM=black line, T/P=red line). Each mode represents 12% and 12% of the overall variance for the NLOM and T/P SSH respectively.

and T/P derived SSH respectively. Mode 3, representing 10% and 7% of the variance for the model and T/P derived data, more closely resembles the interannual signal. However, the close proximity in variance to the higher modes and the shortened time series make a reliable analysis questionable. Still, the modeled SSH field compares extremely well with the satellite derived SSH product suggesting the model reproduces the large scale Pacific Ocean circulation to an amazing degree of accuracy. Higher modes (modes 4 and 5, not shown) concur with this analysis.

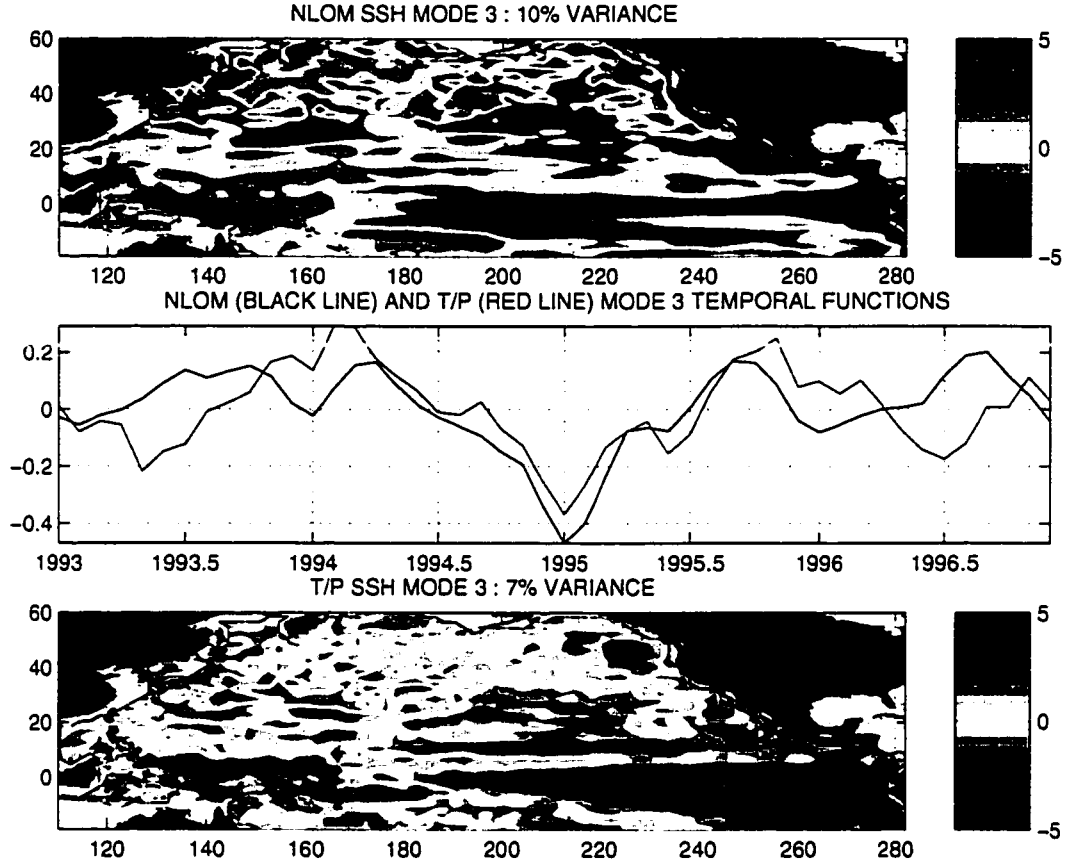


Figure 8: Third mode EOF spatial amplitude functions of the unfiltered NLOM (top) and TOPEX/POSEIDON (T/P, bottom) sea surface height (SSH) along with their associated principal components (middle, NLOM=black line, T/P=red line). Each mode represents 10% and 7% of the overall variance for the NLOM and T/P SSH respectively.

Singular Value Decomposition (SVD) Analysis

In addition to the separate EOF analyses performed above, it is also beneficial to examine the singular value decomposition (SVD) analysis of the cross covariance matrix. As described in section 3.3, the SVD analysis finds coupled modes of variability between the two data sets. If the data sets are identical, the SVD analysis would be equivalent to determining the EOF's of the field. Also, since the EOF analyses above revealed a close agreement between the NLOM and T/P derived SSH fields,

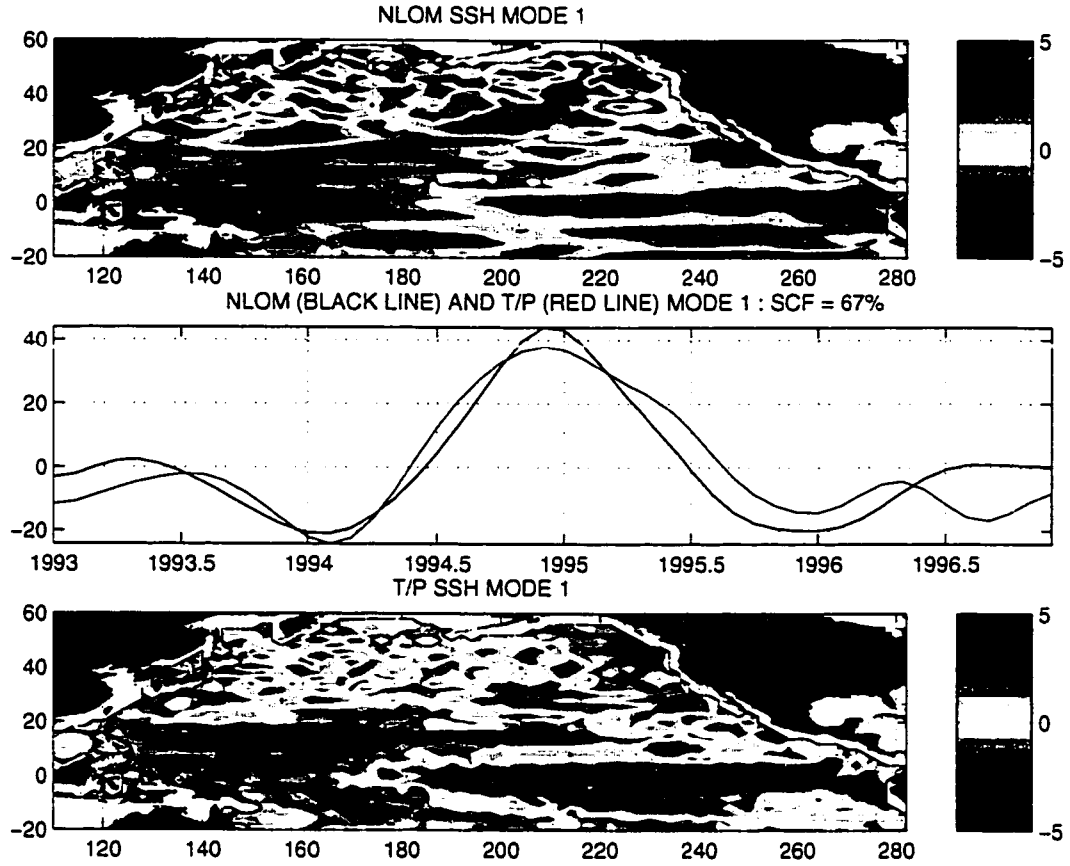


Figure 9: First mode SVD spatial eigenvectors of the low pass filtered NLOM (top) and TOPEX/POSEIDON (T/P, bottom) sea surface height (SSH) along with their associated eigenfunctions (middle, NLOM=black line, T/P=red line). The coupled mode clearly depicts an interannual signal and accounts for 67% of the squared covariance.

SVD analysis on the raw monthly mean fields would be redundant. Instead, the data are low pass filtered (by applying a Hanning filter to the data six times) effectively removing 95% of variability at time scales shorter than 6 months (for a complete derivation of the filter frequency response, see Appendix B).

The first three modes (figures 9, 10, and 11) indicate strong agreement between the modeled and satellite derived large scale SSH accounting for a surprising 96% of the overall squared covariance. The spatial and temporal agreement between the

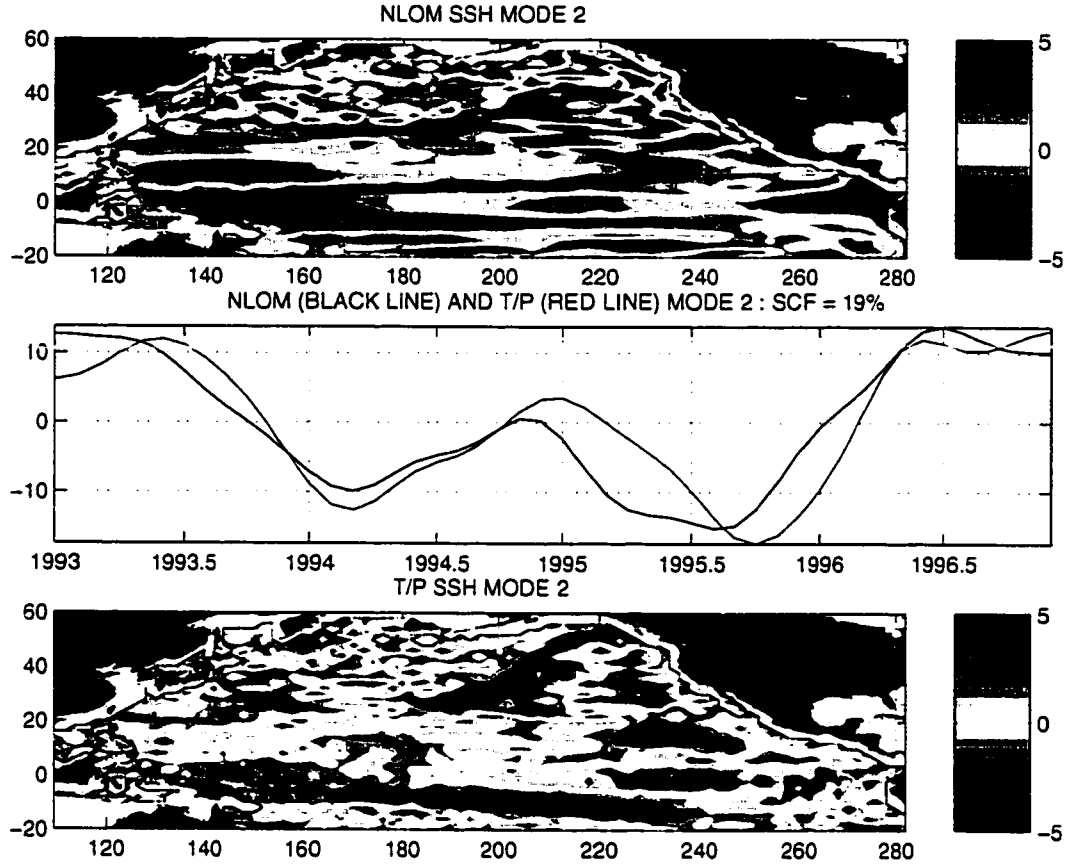


Figure 10: Second mode SVD spatial eigenvectors of the low pass filtered NLOM (top) and TOPEX/POSEIDON (T/P, bottom) sea surface height (SSH) along with their associated eigenfunctions (middle, NLOM=black line, T/P=red line) accounting for 19% of the squared covariance.

NLOM and T/P data confirm the model has the ability to reproduce the observed features, especially the interannual features, of the basin scale circulation. Slight deviations between the two data sets can likely be attributed to errors arising from sampling differences, tendencies in the wind data used to force the model (a complete description of which can be found in *Hundermark et al.* 1999), or the lack of a steric signature in the hydrodynamic model.

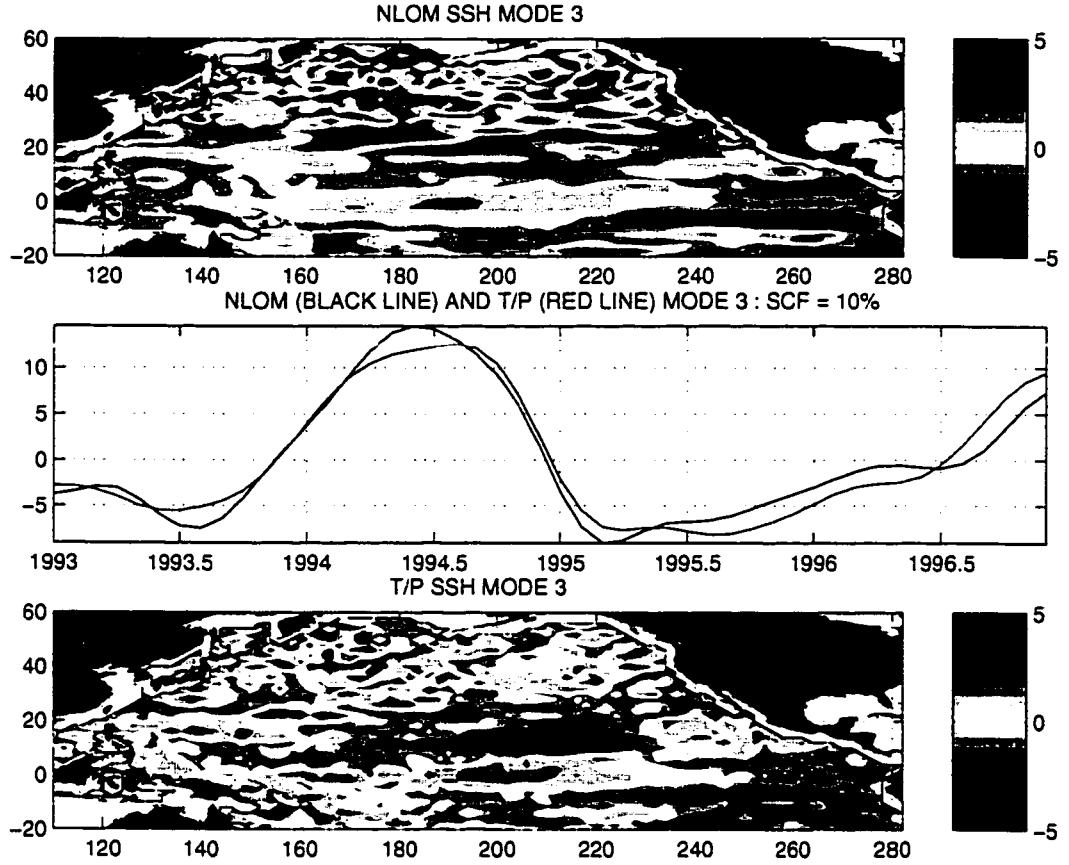


Figure 11: Third mode SVD spatial eigenvectors of the low pass filtered NLOM (top) and TOPEX/POSEIDON (T/P, bottom) sea surface height (SSH) along with their associated eigenfunctions (middle, NLOM=black line, T/P=red line) accounting for 10% of the squared covariance.

Longitude-Time Comparisons

The above analyses provide clear evidence for the ability of the model to reproduce the large scale circulation features in the Pacific Ocean. However, the question remains whether the model adequately describes the local circulation features of interest here, in particular the flow field in the eastern subtropical Pacific Ocean. As such, it is important to investigate these features.

In an effort to validate the model over the eastern Pacific subtropical gyre, time

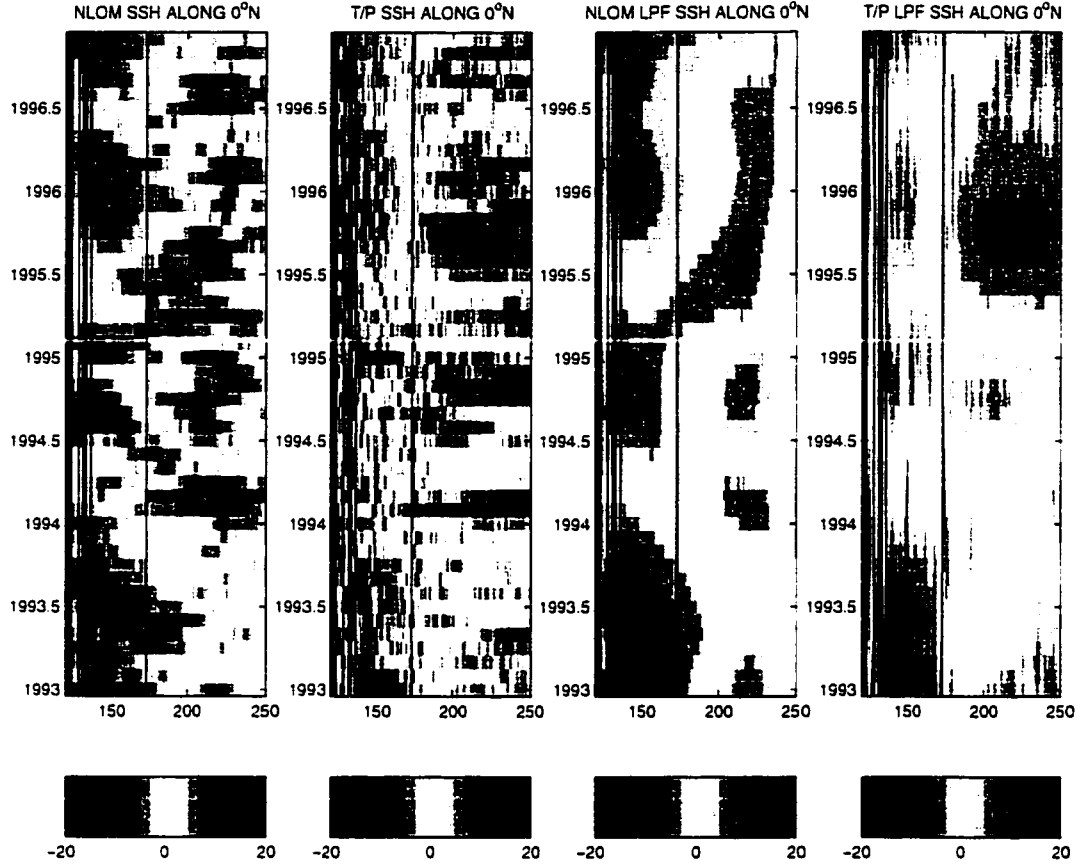


Figure 12: Longitude-time representations of the NLOM and T/P derived SSH signatures along the equator. The left two panels represent the unfiltered NLOM and T/P SSH respectively, while the right two panels compare the low pass filtered NLOM and T/P SSH signals. Units are centimeters.

longitude sections were calculated every ten degrees of latitude from the equator to 30°N . The data are bin averaged over $1^{\circ} \times 3^{\circ}$ longitude \times latitude sections and plotted as Hovmöller diagrams in an effort to compare the westward propagating features seen in both the model and altimetry data. The closest agreement between the model occurs, not surprisingly, at the equator (figure 12), with less agreement occurring poleward (figures 13, 14, and 15). Still, the model seems to do a reasonable job capturing the westward propagating features seen in the data, especially when the data are low pass filtered to retain the interannual time scales.

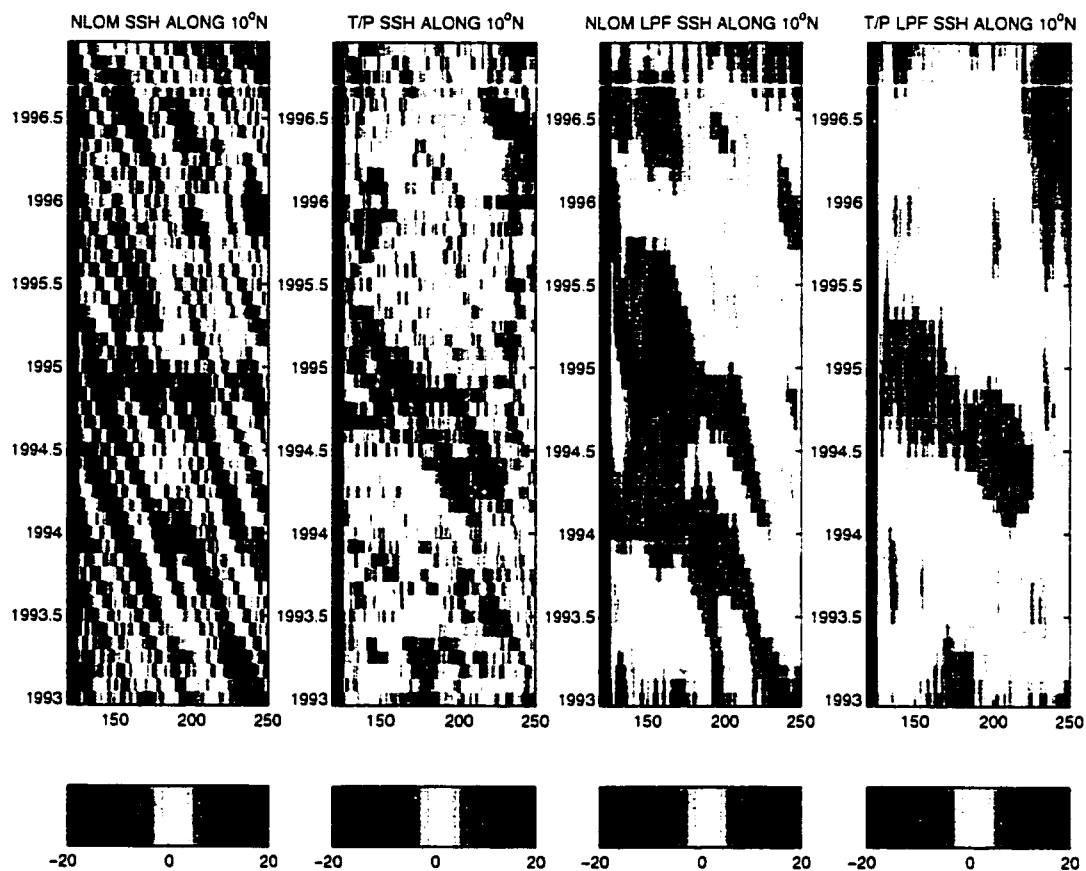


Figure 13: Longitude-time representations of the NLOM and T/P derived SSH signatures along 10°N. The left two panels represent the unfiltered NLOM and T/P SSH respectively, while the right two panels compare the low pass filtered NLOM and T/P SSH signals. Units are centimeters.

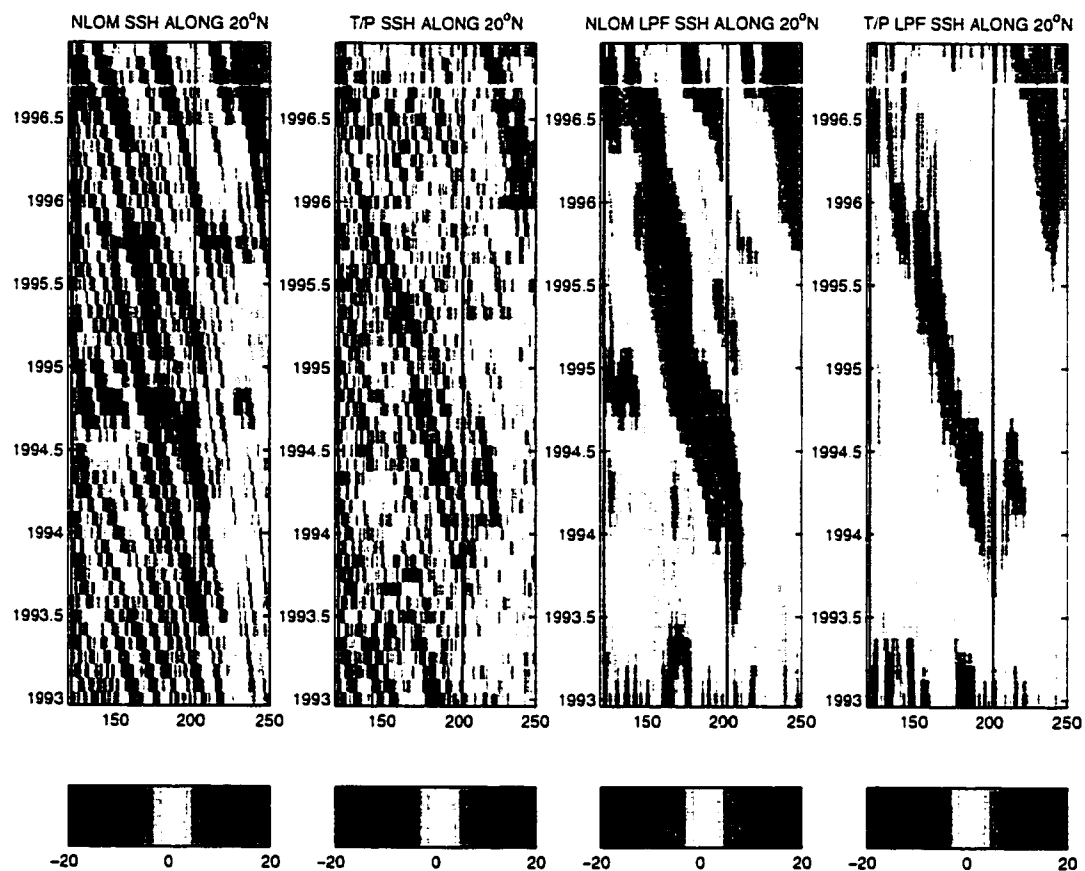


Figure 14: Longitude-time representations of the NLOM and T/P derived SSH signatures along 20°N. The left two panels represent the unfiltered NLOM and T/P SSH respectively, while the right two panels compare the low pass filtered NLOM and T/P SSH signals. Units are centimeters.

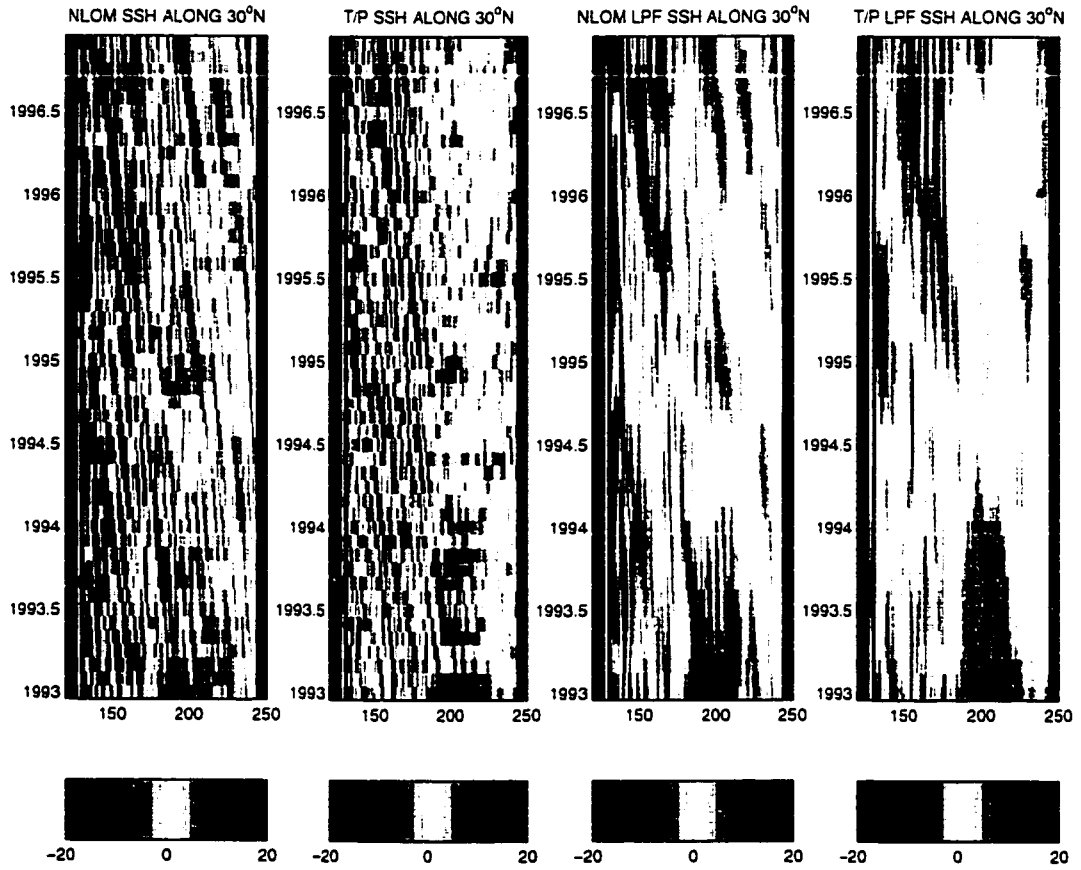


Figure 15: Longitude-time representations of the NLOM and T/P derived SSH signatures along 30°N. The left two panels represent the unfiltered NLOM and T/P SSH respectively, while the right two panels compare the low pass filtered NLOM and T/P SSH signals. Units are centimeters.

5. RESULTS AND DISCUSSION

A simple analytical model is employed to examine the interannual variability in the eastern Pacific subtropical gyre. Although *Kessler* (1990) (and *Meyers* 1975, *White* 1977, 1978, *Meyers* 1979, beforehand) utilized a simple QG model to examine thermocline fluctuations, the isopycnal nature of the model used here allows similar analysis with respect to the modeled upper layer thickness (*White* 1978, *Meyers* 1979, *Qiu et al.* 1997). Applying a few simple assumptions to the generalized Navier-Stokes equations reduces the horizontal equations of motion to

$$\begin{aligned} -fv &= -g' \frac{\partial h}{\partial x} + \frac{\tau_w^x}{\rho H} \\ fu &= -g' \frac{\partial h}{\partial y} + \frac{\tau_w^y}{\rho H} \end{aligned} \tag{17}$$

and the continuity equation to

$$\frac{\partial h}{\partial t} + H \left(\frac{\partial u}{\partial x} + \frac{\partial v}{\partial y} \right) = 0 \tag{18}$$

where all variables are as defined in the appendix with the exception of the reduced gravity, $g' = g \frac{\Delta \rho}{\rho}$.

The above equations can be further reduced by cross differentiation and elimina-

tion of the divergence term via the continuity equation. The result

$$\frac{\partial h}{\partial t} - \frac{\beta c^2}{f^2} \frac{\partial h}{\partial x} = -\nabla \times \frac{\vec{\tau}_w}{\rho f} \quad (19)$$

is the low frequency vorticity equation representing changes in the upper layer thickness (or analogously, the thermocline depth) brought about by Rossby wave propagation and Ekman pumping.

It is important to note that the above equations could not have been brought about without assuming that local accelerations are negligible (the common low-frequency limit, long wave approximation, see *Gill* 1982). Under this assumption, solutions to equation (19) are latitudinally dependent with each latitude independent of the others and long planetary waves being non-dispersive with westward phase speeds dependent on the layer thickness, $c = \sqrt{g'H}$.

Now, although equation (19) is the simplest possible relationship one can obtain when examining time-dependent β -plane dynamics, it is a valuable tool for determining the interannual response of the ocean to both Rossby waves and Ekman pumping. As pointed out by *Kessler* (1990), there are three main limitations to using a simple analytical model of this form: (1) the Rossby waves are treated as being non-dispersive (as stated above), (2) the theory excludes the impacts of strong zonal geostrophic currents, and (3) the simple two layer system automatically assumes that all motion occurs in the uppermost layer. In each case, *Kessler* (1990) examines the limitations and concludes that for extra-equatorial, interannual fluctuations, the attenuated effects of these limitations have negligible impact on the overall nature of the solution.

In contrast, *Killworth et al.* (1997) and *Dewar* (1998) cite that effects arising

from vertical and horizontal shears can exist and produce modified Rossby wave phase speeds in accord with the observations of *Chelton and Schlax* (1996). Both of these impacts are neglected under assumptions (2) and (3) above. Both factors have maximum effect equatorward and poleward of the subtropics. Over the subtropics, however, the effects are minimized. Since the focus here is primarily subtropical and on the effects of large scale WSC, the simple equation presented above is suitable for the present application.

Two common ways to solve equation (19) are through numerical calculation (*Busalacchi and O'Brien* 1980, *Busalacchi et al.* 1983) and integrating along characteristics (*Gill and Clarke* 1974, *Meyers* 1979, *Kessler* 1990). However, since the goal of the current research is to distinguish between and discuss the interannual signals associated with upstream Ekman pumping and Rossby wave propagation, a different approach is applied here. First, SVD analysis will be used to isolate the response of the upper layer thickness to the wind stress curl. Then, CEOF analysis will be used to isolate the response due to large scale propagating features, such as Rossby waves. Finally, M-SSA will be used to further separate the propagating response into its forced and freely propagating components, each of which exist in distinct frequency bands. Consistency between these independent analyses lends considerable weight to the robustness of the results.

Before proceeding to the analysis it is important to note that the following analysis is performed on the upper layer thickness and wind stress curl fields after removing the annual cycle. The logic behind this is two-fold. First, the focus of this research is on the interannual variability of the eastern subtropical Pacific, east of the Hawaiian Islands. Keeping the annual signal only serves to complicate the analysis results. Secondly, both *Kessler* (1990) and *Goldenberg and O'Brien* (1981) provide substantial

evidence for the lack of a strong annual cycle in the mid-latitude eastern Pacific Ocean, especially upstream of Hawaii. In both cases, the primary source of variance associated with the annual cycle occurs along 10°N and is a result of the north-south migration of the trade winds and associated intertropical convergence zone (ITCZ). As such, removing the annual cycle has little, if any, significance on the results over the eastern subtropical Pacific.

5.1 Large Scale Ekman Pumping

In this section, we wish to determine the interannual variability of the topmost model layer to wind stress curl forcing. Equation (19) suggests that increases (decreases) in layer thickness should be associated with negative (positive) wind stress curl anomalies. Thus, any atmospheric response that acts to alter the gradients in the zonal or meridional wind stress will likewise force a response to the upper layer thickness.

As discussed in section 3.3, one of the most efficient ways to isolate the coupled response between two fields is to apply SVD analysis to the fields. Since we are interested in the associated temporal response of the two fields, SVD analysis is applied to the temporal cross covariance matrix of the wind stress curl and the upper layer thickness. Results of the SVD analysis are presented in figures 16-17.

The first SVD mode represents a long term climatological signal with an associated jump in wind stress curl amplitude occurring between 1984 and 1986. However, the length of model results (16 years) limits the ability to clearly determine the source of the signal and its implications. It is possible that the high variance associated with mode 1 is due to strongly coherent wind stress curl maxima in the vicinity of Hawaii or a change in the ECMWF/HR winds themselves (As noted by *Hundermark et al.* 1999). In either case, the overall large scale response is likely due to an interdecadal

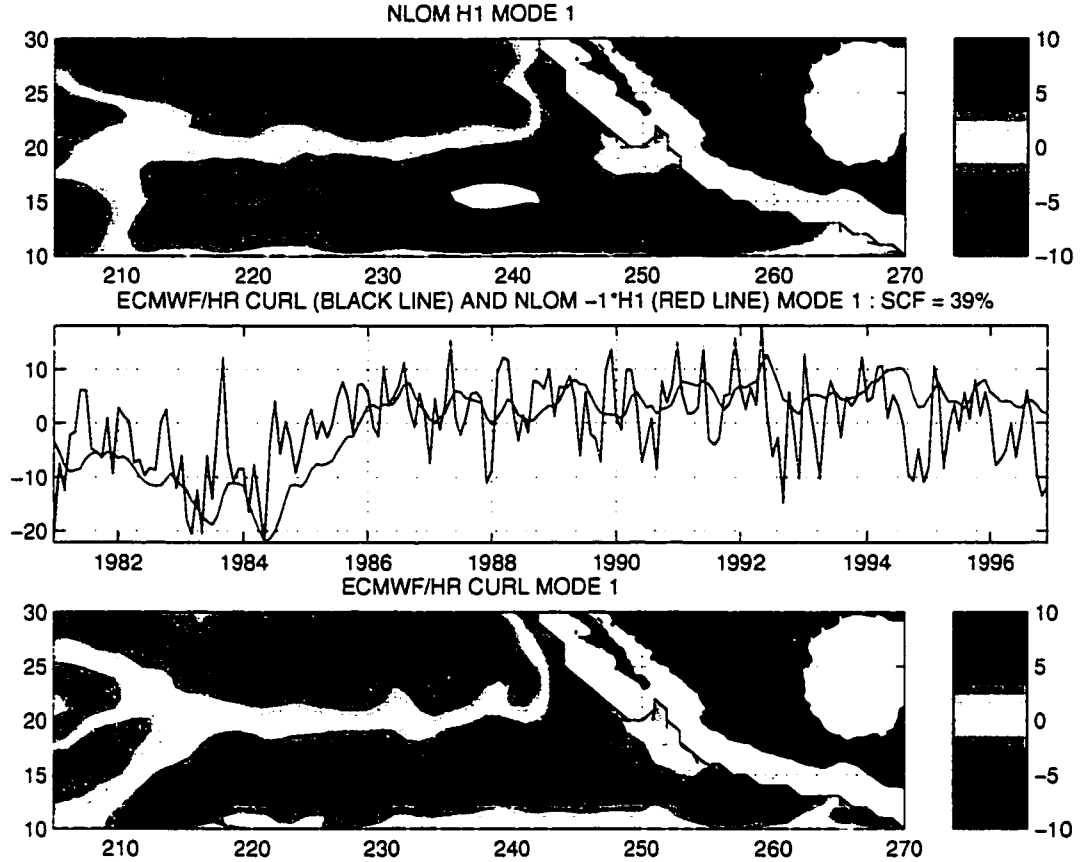


Figure 16: First mode SVD spatial eigenvectors of the monthly mean NLOM upper layer thickness (top) and ECMWF/HR monthly wind stress curl (bottom) along with their associated eigenfunctions (middle, NLOM=black line, ECMWF/HR=red line) accounting for 39% of the overall variance.

pattern that can not be properly resolved by the time series used here, but which is touched upon in appendix C.

The second SVD mode, on the other hand, clearly depicts an interannual signal with a strong relationship between the wind stress curl and the upper layer thickness (both spatially and temporally). For convenience, the upper layer thickness temporal function has been multiplied by -1 to reveal the correspondence with the wind stress curl. As predicted by equation (19), a large positive (negative) wind stress curl anomaly is followed by an associated negative (positive) upper layer thickness

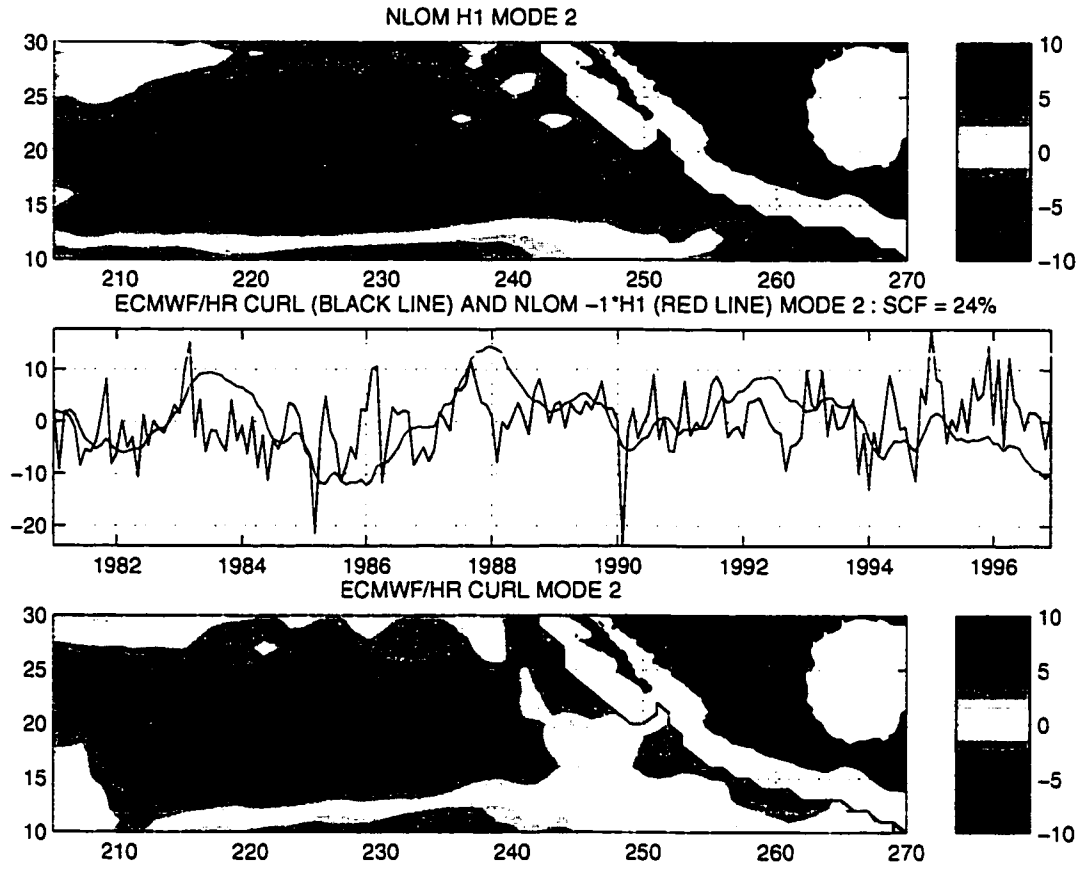


Figure 17: Second mode SVD spatial eigenvectors of the monthly mean NLOM upper layer thickness (top) and ECMWF/HR monthly wind stress curl (bottom) along with their associated eigenfunctions (middle, NLOM=black line, ECMWF/HR=red line) accounting for 24% of the overall variance.

anomaly. Additionally, it should be of no surprise that the wind forcing contains more variability than the upper layer thickness. This owes itself to the slow response time of the ocean (relative to the atmosphere).

For the purposes intended here, it is not necessary to show the results of the higher order SVD modes. It is important, however, to simply state that modes 3 and 4 likely represent additional sources of interannual variability, but with much lower variance (13% and 8% respectively). The modes themselves probably represent part

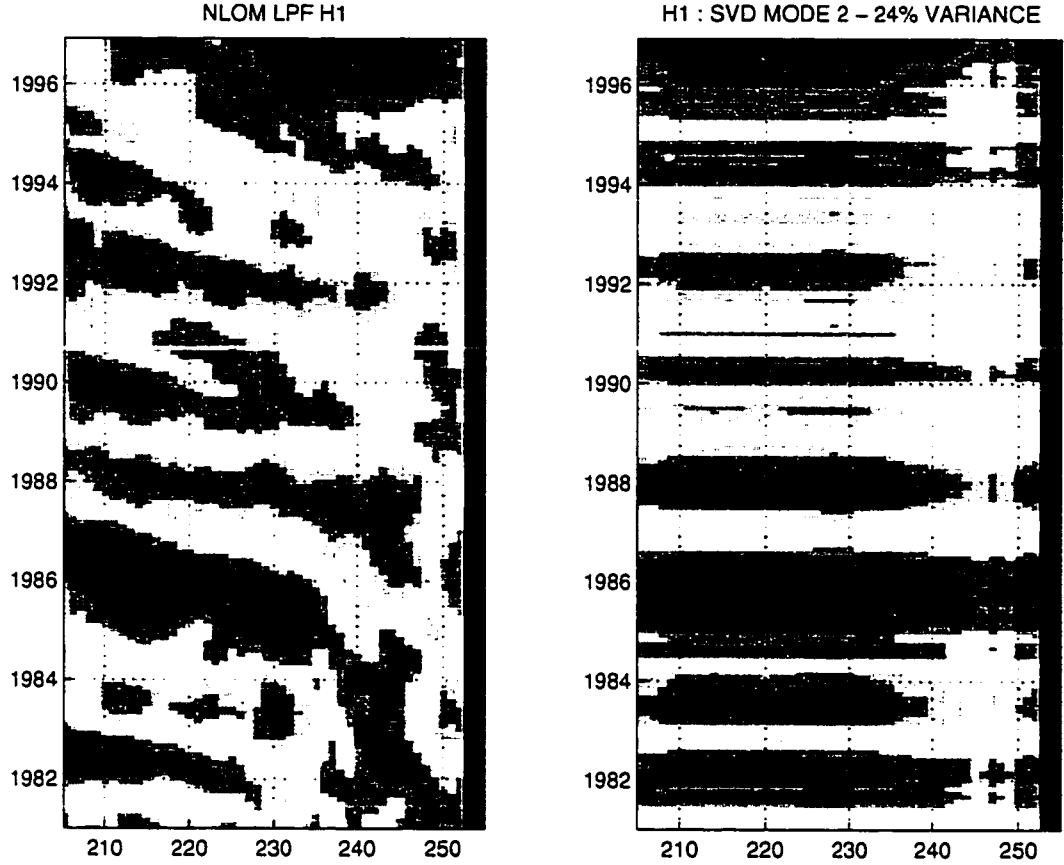


Figure 18: Modeled upper layer thickness anomaly (left) and upper layer thickness anomaly associated with the coupled SVD mode 2 (right) along 20°N upstream of the Hawaiian Islands. For comparison purposes, the modeled upper layer thickness is normalized in a manner consistent with the SVD analysis (see section 3.3). The coupled standing mode (right) represent 24% of the overall coupled variance.

of a propagating pattern associated with or resulting from SVD mode 2. Overall, it should be noted that the first four modes of the SVD analysis account for 82% of the overall squared covariance.

Now that we have determined that there is indeed a coupled response between the upper layer thickness and the wind stress curl, it is important to discuss the response in relation to the flow over the region of interest. Hovmöller diagrams of the modeled upper layer thickness and the upper layer thickness response associated

with the wind stress curl for SVD mode 2 upstream of the Hawaiian Islands along 20°N (figure 18, left and right respectively) reveal a distinct correspondence between the modeled and projected upper layer thickness. Note, since the coupled response has largest amplitude and is centered around 20°N latitude, this latitude is chosen as a representative example throughout the remaining discussion.

The coupled SVD mode clearly shows up and compares extremely well with the modeled upper layer thickness. The interannual signal is very pronounced in both with slight deviations in the modeled upper layer thickness. These deviations are likely associated with large scale propagating features, such as long Rossby waves or extremely low frequency variability, as will be addressed in the following sections.

5.2 Propagating Patterns

Returning to equation (19), we can recall that there are two main mechanisms involved in the vorticity equation for our system that produce changes in the upper layer thickness. The first, the response of the upper layer thickness to the wind stress curl, was addressed in the previous section and shown to provide a strong and coherent source of variability over the region and, in particular, along 20°N latitude. The latter mechanism is the advection of gradients in the upper layer thickness by large scale propagating features, in this case Rossby waves. This term will be discussed below.

Since we are interested in propagating features, it is wise to use a tool that is specifically designed to isolate coherent propagating features with substantial amounts of variance. Although a variety of methods can be employed to examine these features, the method used here is the common and popular complex empirical orthogonal function (CEOF) analysis (described in section 3.2). CEOF analysis, like EOF analysis, is designed to find the modes of variability in the data set that account for the largest

amount of variance. Unlike EOF analysis, however, CEOF analysis has the added functionality that it is designed to distinguish propagating modes of variability.

NLOM LAYER 1 THICKNESS CEOF MODE 1 : 21% VARIANCE

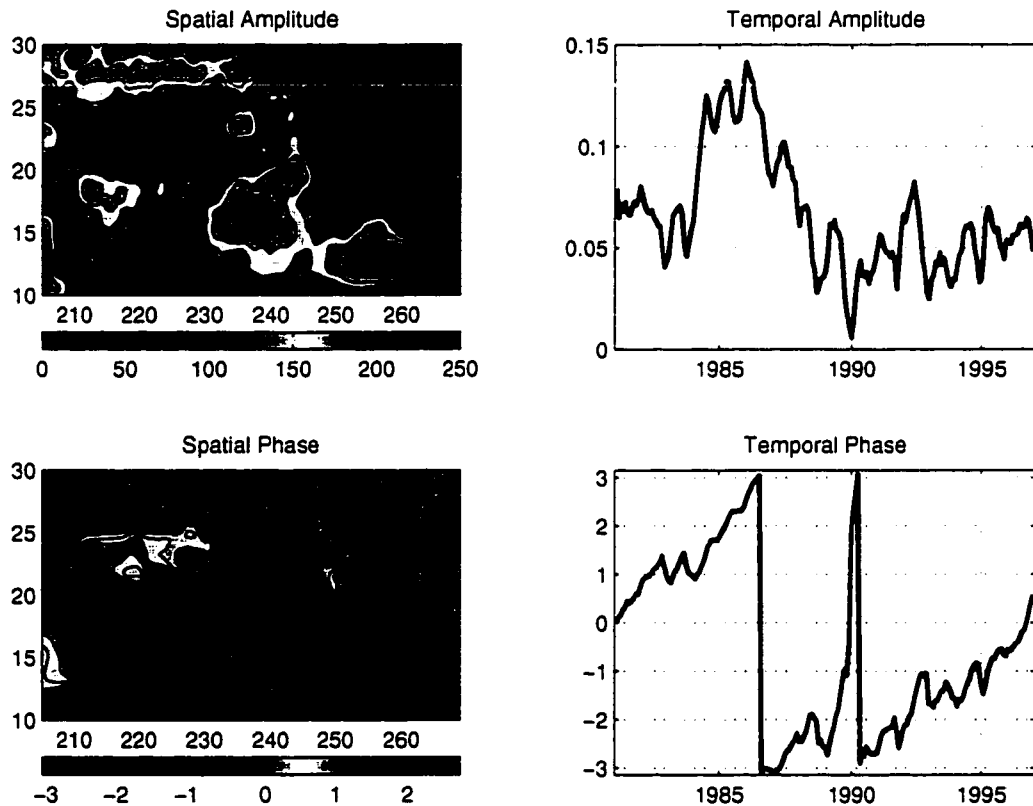


Figure 19: Mode 1 CEOF upper layer thickness response representing 21% of the overall variance for the unfiltered monthly data. Shown clockwise from the top left are the (a) spatial amplitude function, (b) the temporal amplitude function, (c) the temporal phase (in radians), and (d) the spatial phase (in radians). Note: the large north south dipole in the spatial phase and the shift in temporal phase represent a low frequency, large spatial scale change in the overall structure of the eastern North Pacific Ocean, possibly associated with the Pacific Decadal Oscillation (PDO, see Appendix C).

The spatial and temporal representations of CEOF modes 1-3 show similar results to the SVD analysis. The dominant mode (figure 19), reveals the same low frequency pattern as the SVD analysis. As was stated before, this is likely a longer term response resulting from an interdecadal signature in the wind forcing (as discussed in appendix

NLOM LAYER 1 THICKNESS CEOF MODE 2 : 15% VARIANCE

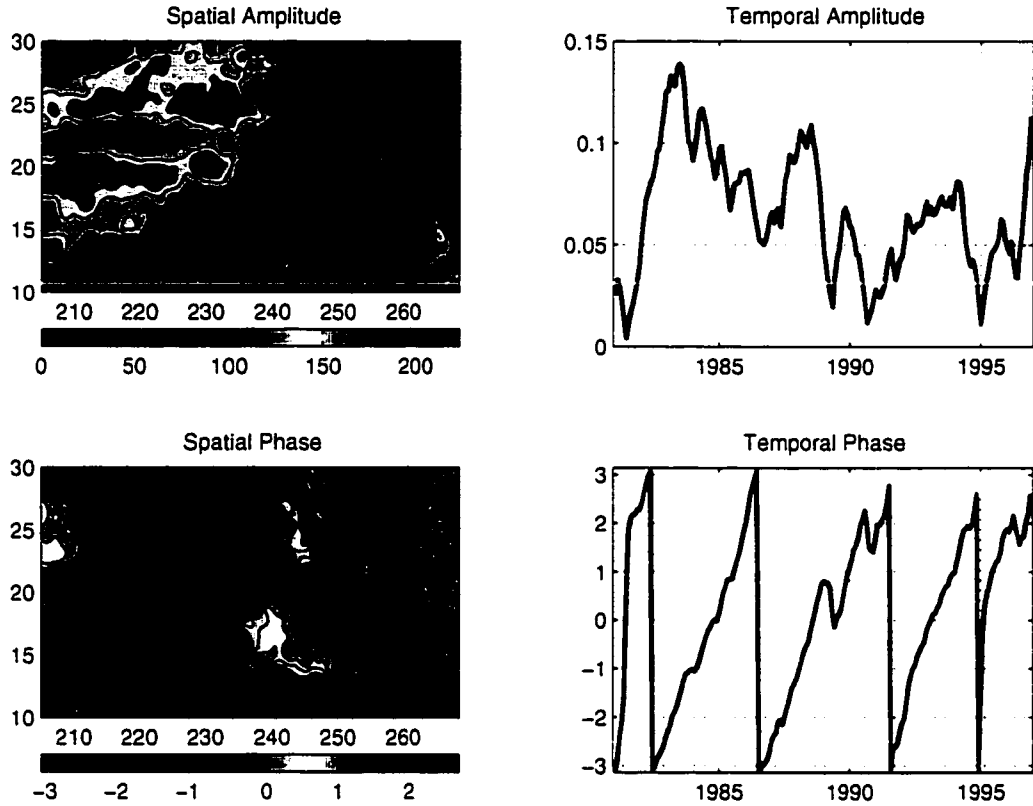


Figure 20: As in figure 19, except for CEOF mode 2 representing 15% of the overall variance.

C). Again, though, the time series of the model results does not allow for a direct analysis of this longer time scale feature. Whatever the responsible mechanism may be, the probable result is a simple alteration of the background state upon which the interannual variability acts (*Wang 1995, Wang and Ropelewski 1995*). For the purposes of the current research it is simply stated and left to future research.

The second most dominant CEOF mode (figure 20), encompassing 15% of the overall variance, represents the large scale Ekman pumping modes described in section 5.1. The spatial function shows a large amplitude response upstream of the Hawaiian

NLOM LAYER 1 THICKNESS CEOF MODE 3 : 8% VARIANCE

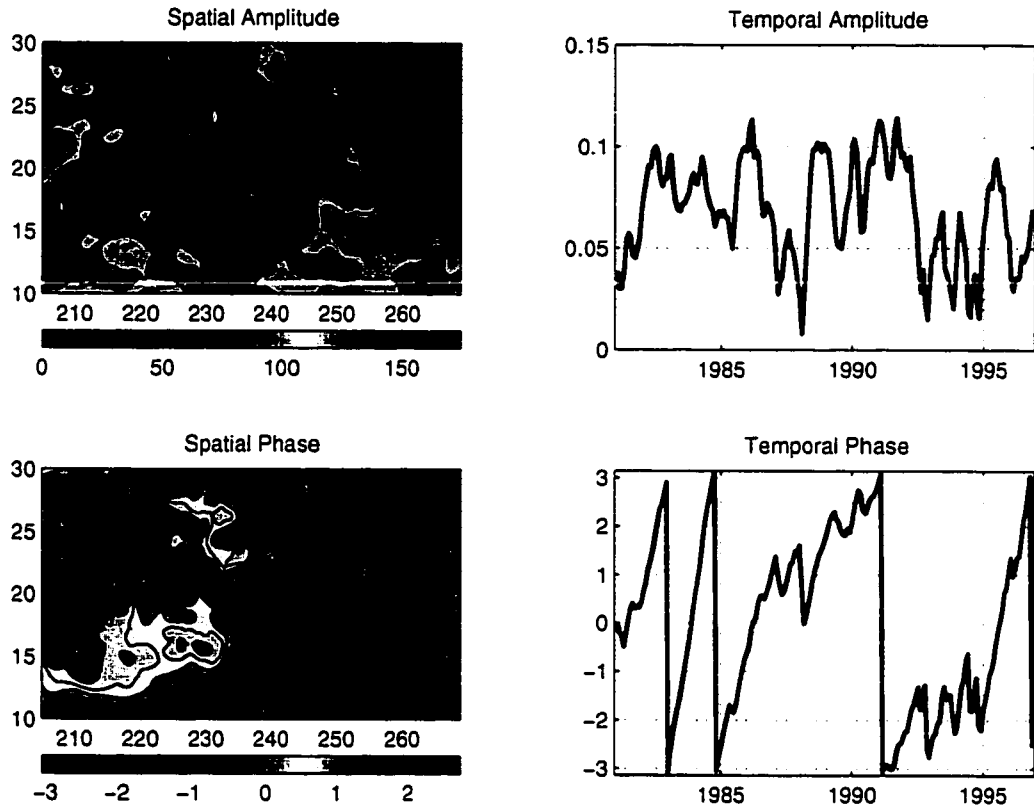


Figure 21: As in figure 19, except for CEOF mode 3 representing 8% of the overall variance.

Islands between 210° - 240° E and (for the most part) out of phase with the coastal response to its immediate east and southeast. The signal represents the dominant interannual signal over the region with a period of roughly four years. As will be discussed below, this signal represents large scale wind forced Rossby waves.

CEOF mode 3 is the first mode that begins to show the signature of a coastally generated wave pattern. Modes 3-5 (figures 21, 22, and 23) combined represent the effects of poleward propagating coastally trapped Kelvin waves and the westward propagating free Rossby waves generated by them. The largest (spatial) amplitude

NLOM LAYER 1 THICKNESS CEOF MODE 4 : 5% VARIANCE

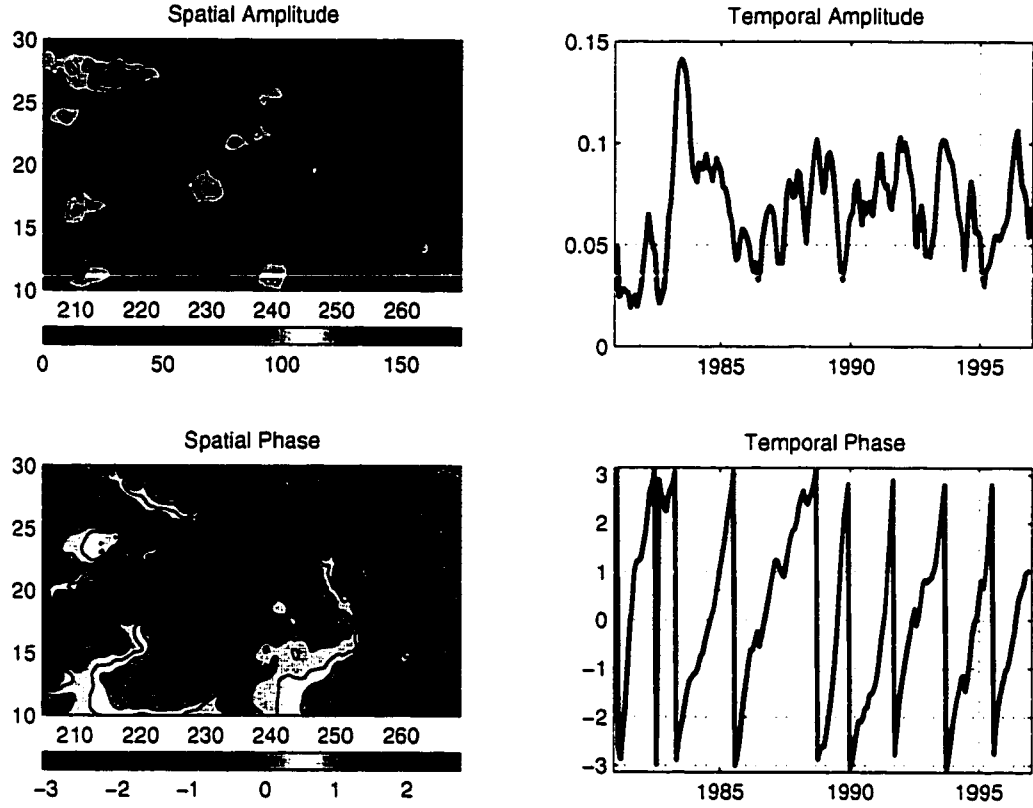


Figure 22: As in figure 19, except for CEOF mode 4 representing 5% of the overall variance.

response can be found in mode 3 off the coast of Mexico from the Gulf of Tehauntepec to the Gulf of California. The spatial amplitude response is much smaller for modes 4 and 5, but the spatial phase more clearly defines the coastally and westward propagating wave patterns. Additionally, modes 3-5 (mode 4 in particular) temporal phase functions reveal the biennial nature of the coastally generated waves while at the same time retaining signatures associated with the interannual mode seen in mode 2. Combined, modes 3-5 represent 17% of the overall variance.

Now, for comparison purposes, it is convenient to revert back to the Hovmüller

NLOM LAYER 1 THICKNESS CEOF MODE 5 : 4% VARIANCE

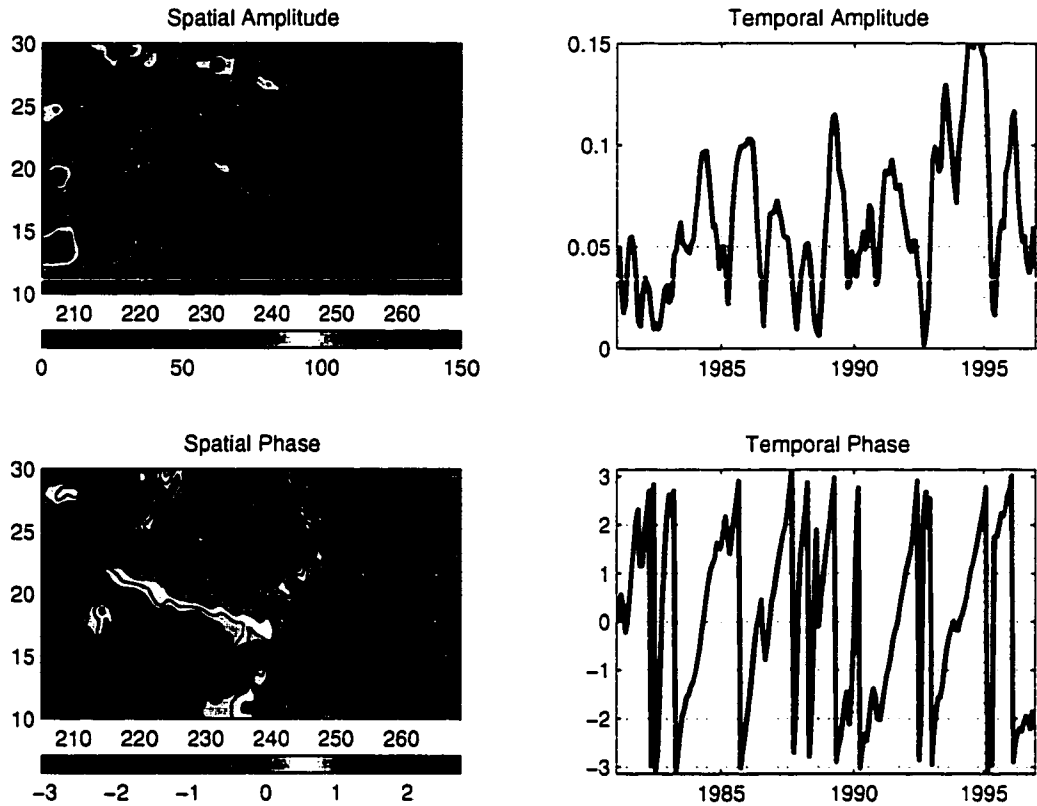


Figure 23: As in figure 19, except for CEOF mode 5 representing 4% of the overall variance.

diagram of figure 18 (left) showing the modeled upper layer thickness response along 20°N latitude. As shown in the figure and discussed previously, it is clear that the large scale Ekman pumping is producing dramatic interannual variability over the eastern subtropical Pacific Ocean. However, the question remains: what is the nature of this variability and what are its sources? CEOF analysis can be used to attempt to assess the nature of the variability and to some degree its sources. This will be addressed next.

For clarity, CEOF modes 1-5 along 20°N are plotted (figure 24a-e) along with

their summed response (figure 24f-j). The figure provides a clear representation of not only the modes themselves, but also of the attenuated response of the modes. As more modes are added together, the CEOF analysis compares more favorably with the original data, as is expected. Additionally, it is easy to discern when features become prominent in the variability as well as their attenuated response.

The results reveal an interesting establishment in the upper layer thickness over the region. *A priori*, the two key elements thought responsible for the interannual variability in the eastern subtropical Pacific were the Ekman pumping and low frequency, freely propagating Rossby waves. The results presented here suggest that the propagating features noted in figure 18 are not entirely due to a coastally generated Rossby wave response. Instead, one of the primary propagating signals (at least in the Hovmöller diagram), beginning in late 1985 and continuing across the basin and arriving at the island of Hawaii by 1988, may actually be a result of the low frequency response here attributed to an interdecadal mode (see above and appendix C for details).

Aside from this large scale feature, the CEOF analysis suggests large scale propagating patterns emanating from near (modes 3-5) and away from (mode 2) the boundary. East of 240°E, the signal emanates from the eastern boundary and propagates westward. This feature is likely a coastally generated long Rossby wave. The signal continues west of 240°E, but is not as coherent (mode 3) and with potentially faster propagation speed. At 240°E, another signal becomes apparent. Mode 2 exhibits a signal beginning at or near 240°E that propagates rapidly (faster than the coastally generated wave) westward. This signal is associated with the interannual Ekman pumping described in SVD mode 2 and likely represents a wind forced Rossby wave.

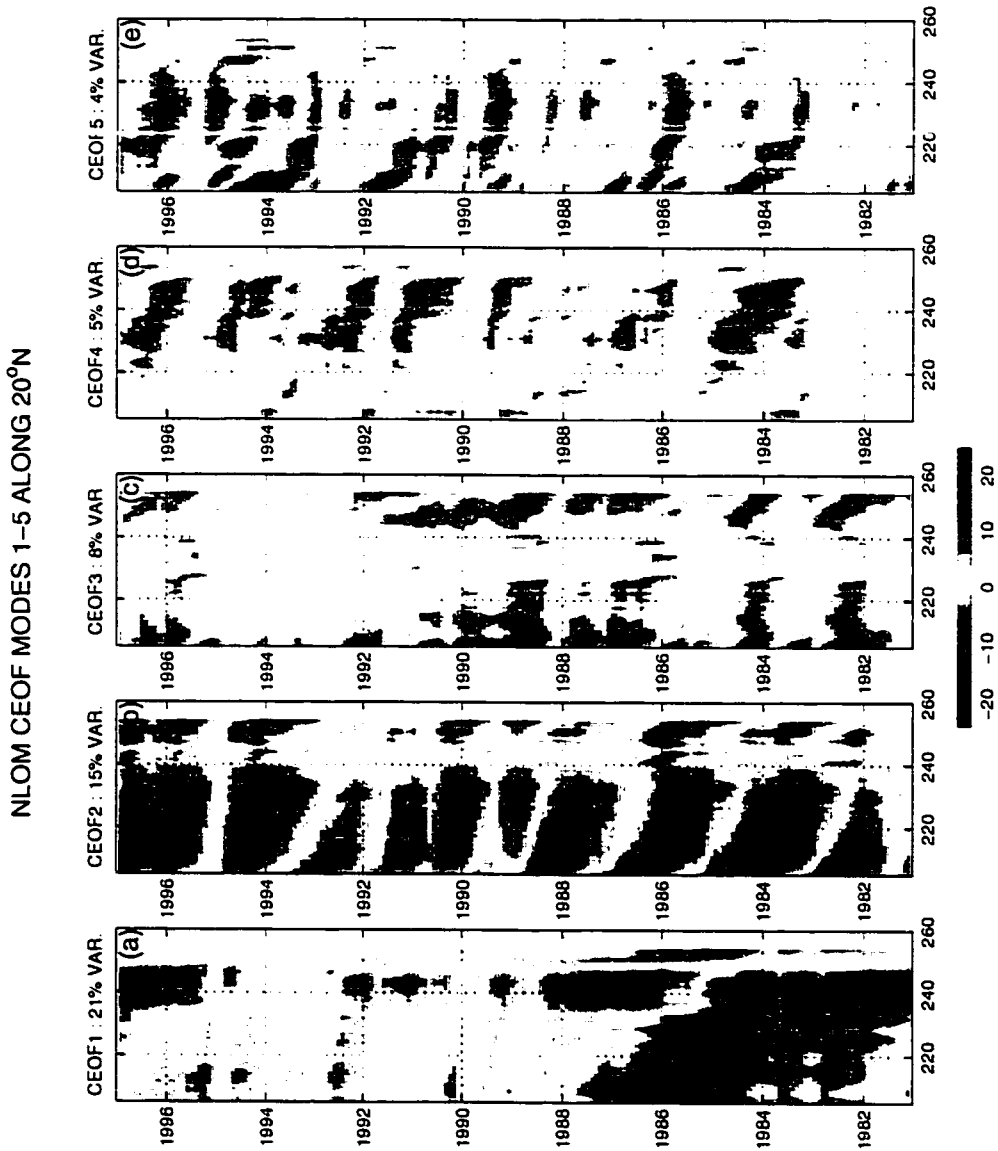


Figure 24: Hovmöller plots along 20° of CEOF modes 1-5. Shown are the modes themselves (a-e) as well as the modes summed consecutively. For example, panel (c) shows the response of mode 3 by itself, while panel (h) shows the attenuated effects of modes 1-3. Similarly, panel (e) shows the response of mode 5 alone, while panel (j) shows the attenuated response of modes 1-5. Variances are given as the percent of overall variance associated with the given mode (a-e) and the variance associated with the attenuated response of the summed modes (f-j).

NLOM CEOF SUMMED MODES 1-5 ALONG 20°N

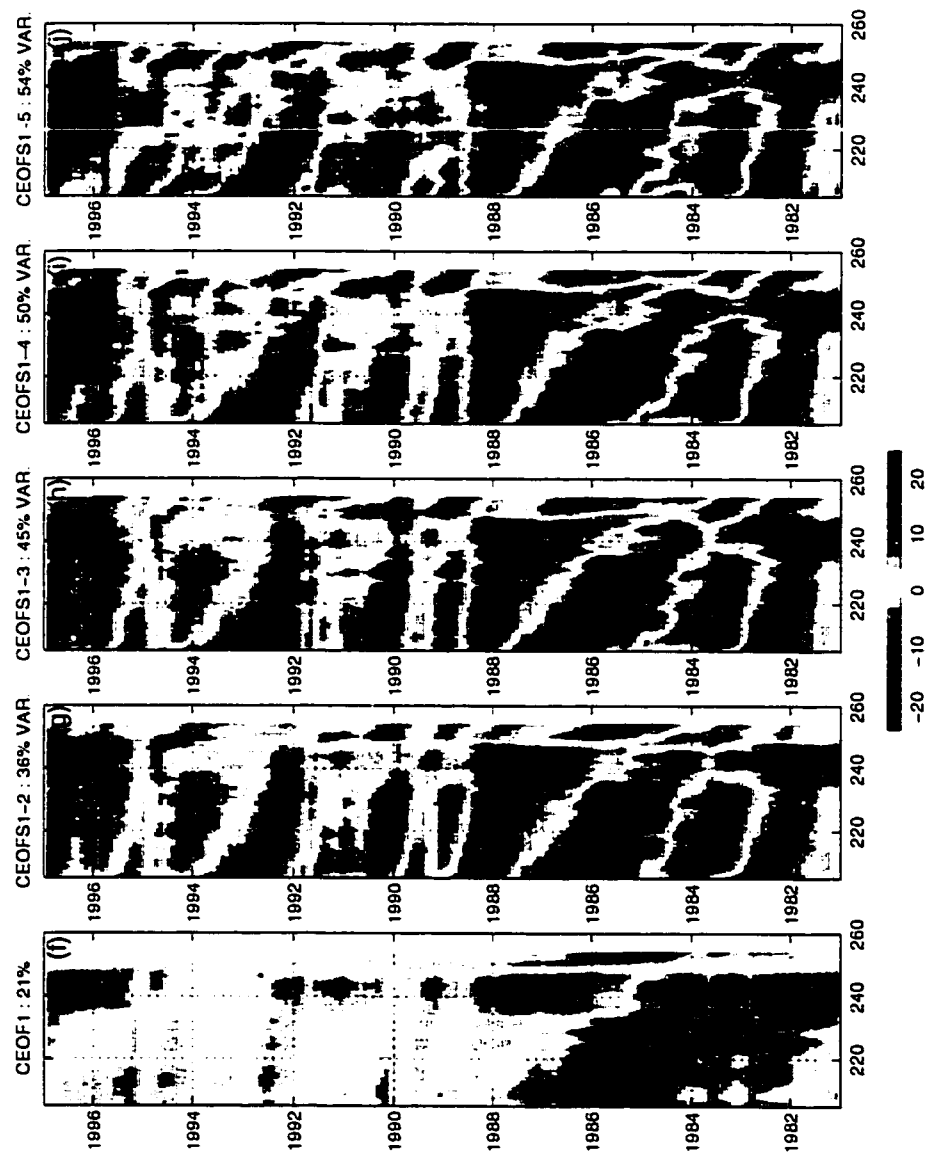


Figure 24: (Continued).

It is important to note that one can distinguish coastally propagating features in the CEOF analysis (not explicitly shown). Namely, poleward propagating Kelvin waves are seen along the eastern boundary in both the spatial amplitude and phase functions, and the Hovmöller diagrams. The Kelvin wave signature exists in all of modes 2-5 of the CEOF analysis as a propagating feature along the coast following the El Niño warm phase events of 1982-83, 1986-87, and 1991-92. However, the signal is strongest in the higher modes with slight modifications occurring from the lower modes.

As is expected (*Chelton and Davis* 1982, *Pares-Sierra and O'Brien* 1989, *Johnson and O'Brien* 1990, *Kessler* 1990, *Shriver et al.* 1991, *White* 1994, *Miller et al.* 1997) the coastally propagating Kelvin waves produce Rossby waves along the North American coast which propagate westward into the basin. However, over the eastern subtropical Pacific Ocean and away from the boundary, the coastally generated Rossby waves (modes 3-5) have a secondary effect to the mid-basin, wind forced Rossby waves (mode 2). This feature has also been observed and discussed by *Miller et al.* (1997) who associate the large wind anomalies with interannual fluctuations in the Aleutian Low pressure system.

5.3 Forced Atmosphere-Ocean Response

Examination of the SVD results suggested a large scale atmosphere-ocean response in which interannual WSC deviations give rise to interannual deviations in ULT. At the same time, CEOF analysis suggests that not only are these interannual fluctuations propagating, but they are also distinct from the freely propagating Rossby waves generated at the eastern boundary. In this section, M-SSA is applied to the ULT and WSC fields in an attempt to gather more information about the propagating

interannual features exhibited in the previous sections.

As was stated in section 3.4, M-SSA is a technique, analogous to both SVD and EOF analysis, aimed at determining oscillating modes of variability in a given data set. In essence, M-SSA filters the data along given channels (or frequency bands) and extracts the modes of variability with maximum variance. The result is a series of oscillating modes of variability that clearly distinguish between patterns of variability that may otherwise be indistinguishable.

In the remainder of this section, the results of M-SSA will be presented for both ULT and WSC anomalies. It is important to note, however, that the M-SSA has been applied to these fields independently. Unlike SVD analysis, in which the cross covariance matrix of the two fields is used, M-SSA is applied to the WSC and ULT separately. Thus, the results represent oscillating modes of variability for each individual field and can not be assumed to be part of a coupled mode of variability *a priori*. Additionally, as before, the data here are preprocessed to remove the annual cycle in an effort to better extract the interannual signals of variability. In all of the results presented below, a window of $m = 60$ months was chosen. Finally, since it is representative of the region, only results along 20° are shown.

Results of the M-SSA analysis (figures 25, 26, and 27) are intriguing. M-SSA modes 1 and 2 are temporally and spatially lagged, indicating they are part of a propagating mode. Similarly, modes 3 and 4 represent the second largest propagating mode and modes 5 through 10 represent the third largest propagating mode (at least for ULT). For the remainder of this discussion, we will refer to these three modes as RC_{1-2} , RC_{3-4} , and RC_{5-10} respectively (where RC represents the reconstructed mode).

Unlike both the SVD and CEOF analyses, the leading M-SSA mode does not

represent a longer term inter-decadal signal. Instead, this interdecadal signal shows up as the second reconstructed M-SSA mode (RC_{3-4}). The leading M-SSA mode (RC_{1-2} , figure 25), on the other hand, represents the large scale interannual signal seen in SVD and CEOF mode 2. In the case of M-SSA, RC_{1-2} , which contains 59% and 21% of the ULT and WSC variance respectively, represents oscillating modes in both WSC and ULT that propagate westward at $\sim 12 \text{ cm/s}^2$ with WSC propagation leading ULT propagation by roughly 3 months. Additionally, both WSC and ULT modes exhibit strong quadrennial (~ 51 months) periods of oscillation.

The second leading mode, made up of M-SSA modes 3 and 4, represents the familiar low frequency signal seen in the SVD and CEOF analysis. Due to the nature of the M-SSA analysis, the signal is not well represented and for the purposes here will be ignored. As has been stated throughout, the model (and in this case the technique) is not suited for examining this mode. Instead, a small discussion is made in an appendix and the remainder is left for future work.

The next substantial mode, RC_{5-10} , is comprised of numerous M-SSA modes³. M-SSA modes 5-10 collectively represent a quasi-biennial signal in both ULT and WSC. In the case of WSC, the signal carries 31% of the overall variance and represents primarily a standing mode of variability. Alternately, the ULT response carries 16% of the overall variance and represents Rossby waves emanating from the eastern boundary and propagating westward freely with a phase speed of $\sim 8 \text{ cm/s}$. It should be noted, however, that aside from the similar biennial characteristics of WSC and ULT mode RC_{5-10} , there is likely no direct connection between the two fields for

²In the above analysis, phase speeds are estimated by constructing a longitude lag/time lag correlation matrix similar to that presented by *White et al.* (1985). In this method, a correlation matrix is created for the given longitude-time (Hovmöller) plot and a best line fit is calculated to determine the propagation speed.

³Since the individual M-SSA modes 5-10 all represent similar temporal and spatial characteristics, with closely corresponding eigenvalues, they are chosen to represent a single mode of variability.

these higher modes. This is clearly represented in the power spectral magnitude for the modes (figure 27) which indicates frequencies corresponding to 17 and 24 month periods for WSC and ULT respectively. Additionally, coupled with the CEOF analysis, this is further proof that these freely propagating Rossby waves and the wind forced Rossby waves of RC_{1-2} are distinct features of the interannual variability.

5.4 Discussion

Analysis of WSC and ULT anomalies have revealed several significant results. First, on interannual time scales, the leading order variability in the eastern subtropical Pacific Ocean can likely be attributed to large scale variability in the wind stress curl and its associated Ekman pumping. The Ekman pumping anomalies give rise to wind forced Rossby waves. Second, The WSC related Ekman pumping and wind forced Rossby waves both propagate westward at phase speeds of roughly 12 cm/s with WSC leading Rossby wave propagation by about 3 months. Third, higher order interannual variability can be attributed to freely propagating Rossby waves generated at the eastern boundary. These freely propagating waves, with phase speeds (8 cm/s) consistent with linear theory, are a distinct oceanic feature and, other than their generation, are not associated with the local Ekman pumping.

Up to this point, there has been relatively little qualitative discussion of the physical processes responsible for the variability. The goal of the current section is to remark on the physics behind the variability using results provided herein. In light of recent observational and theoretical evidence (*Miller et al.* 1997, *White et al.* 1998, *White* 2000), a thorough understanding of the dynamics may not be possible through the use of a hydrodynamical model. That notwithstanding, a purely speculative discussion can be made given past and recent theoretical and observational results. The

remainder of this section will focus on this matter in an effort to provide motivation for future studies.

As was stated in the introduction, numerous theories exist providing a potential explanation for discrepancies between phase speeds of Rossby waves predicted by standard linear theory and those observed by *Chelton and Schlax* (1996). Among these, *Killworth et al.* (1997) and *Dewar* (1998) suggest that interactions between the waves and the mean flow are accountable for the discrepancy. Alternately, *Qiu et al.* (1997) suggests that eddy dissipation reduces the effects of freely propagating waves allowing for the preferential selection of wind forced Rossby waves with phase speeds roughly twice that of standard linear theory and in agreement with the theory of *White* (1977). Finally, observational and theoretical studies suggest that the noted discrepancies are due to large scale atmospheric forcing which has the ability to produce forced Rossby waves with phase speeds twice that expected by linear theory alone. Of these mechanisms (additional theory exists relating propagation speeds to topography, *Barnier* 1988), the results presented here apply to the latter and suggest that faster than expected interannual Rossby waves are the result of large scale, coherent interannual fluctuations in the atmosphere.

Recently, *Miller et al.* (1997) reported observations of interannual thermocline variations in the North Pacific Ocean. Augmenting their observations with the results of a coarse resolution numerical model, *Miller et al.* (1997) conclude that these thermocline variations are long westward propagating Rossby waves with phase speeds slightly faster than linear theory. Further, their model results suggest that although the ocean response is a combination of Ekman pumping as well as westward propagating Rossby waves, that near the eastern boundary the primary component is a tropical remote response, but that this response contributes only weakly in the ocean

interior.

In complementary studies, *White et al.* (1998) and *White* (2000) examine large scale coherent patterns in both atmospheric and oceanic variables. In each study, the authors find biennial Rossby waves with phase speeds consistent with the observations of *Chelton and Schlax* (1996). In CEOF analyses, both oceanic and atmospheric beta-refraction patterns exhibit the classical Rossby wave signature, suggesting that the oceanic Rossby waves are coupled with the overlying atmosphere. Furthermore, the authors suggest that the coupling exists as a self promoting feedback between the atmosphere and the ocean. They hypothesize that warm sea surface temperature anomalies that are found west of Rossby wave related sea level height (SLH) anomalies give rise to anomalies in the local WSC curl. These WSC anomalies then promote Ekman pumping, which in turn promotes westward and northward phase propagation of the SLH anomalies, thus sustaining and promoting the westward traveling wave pattern and associated beta-refraction signal.

The results presented in this study are in agreement with those of *Miller et al.* (1997), *White et al.* (1998) and *White* (2000). Namely, SVD, CEOF, and M-SSA results suggest that interannual variations in the interior eastern subtropical Pacific Ocean are coupled with large scale fluctuations in the wind stress curl. At the same time, unlike the previous authors, the results presented here reveal two distinct forms of westward propagating Rossby waves, one which is boundary generated with phase speed consistent with that of linear theory and the other which is wind forced and faster, consistent with the theory of *White* (1977) and *Qiu et al.* (1997). Unfortunately, since the model used here is hydrodynamic, questions regarding the positive feedback mechanism of *White et al.* (1998) and *White* (2000) can not be answered at the present time. Still, the results promote the notion that extratropical wind stress

curl variability plays an important role in mid-latitude interannual ocean variability and suggest further investigations involving ocean-atmosphere coupling should be pursued.

M-SSA Reconstructed Principal Components Modes 1-2

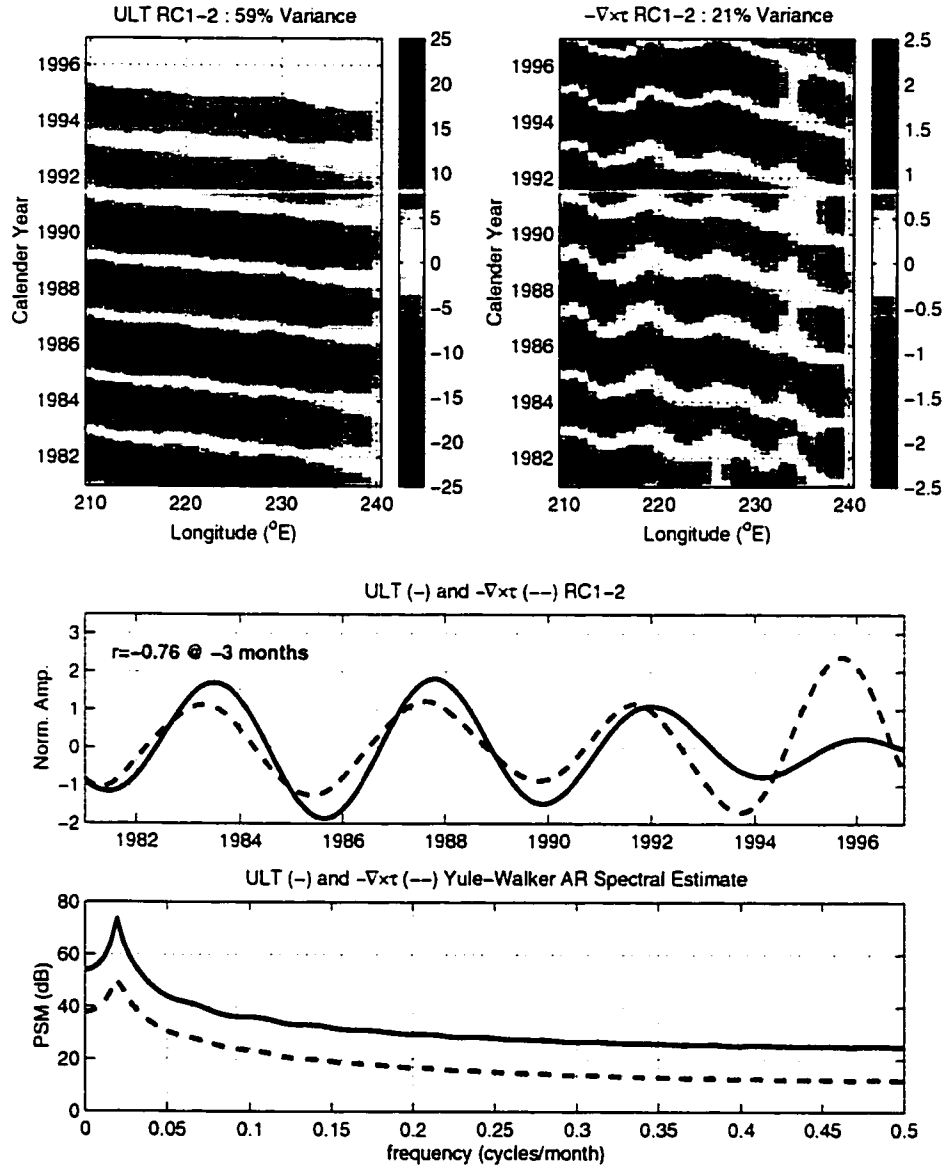


Figure 25: Multi-channel singular spectrum analysis (M-SSA) results for upper layer thickness (ULT) and wind stress curl (WSC). Interannual variability is represented by reconstructed components 1 and 2 (RC_{1-2}) for both ULT, carrying 59% of the variance (top left), and WSC, carrying 21% of the variance (top right), respectively. The reconstructed principal components (middle panel) are highly correlated, $r = -0.76$ at the 99% confidence level, with WSC variations leading ULT by 3 months. Both ULT (bottom panel, solid line) and WSC (bottom panel, dashed line) show strong spectral peaks in the interannual band with frequencies corresponding to ~ 51 months.

M-SSA Reconstructed Principal Components Modes 3–4

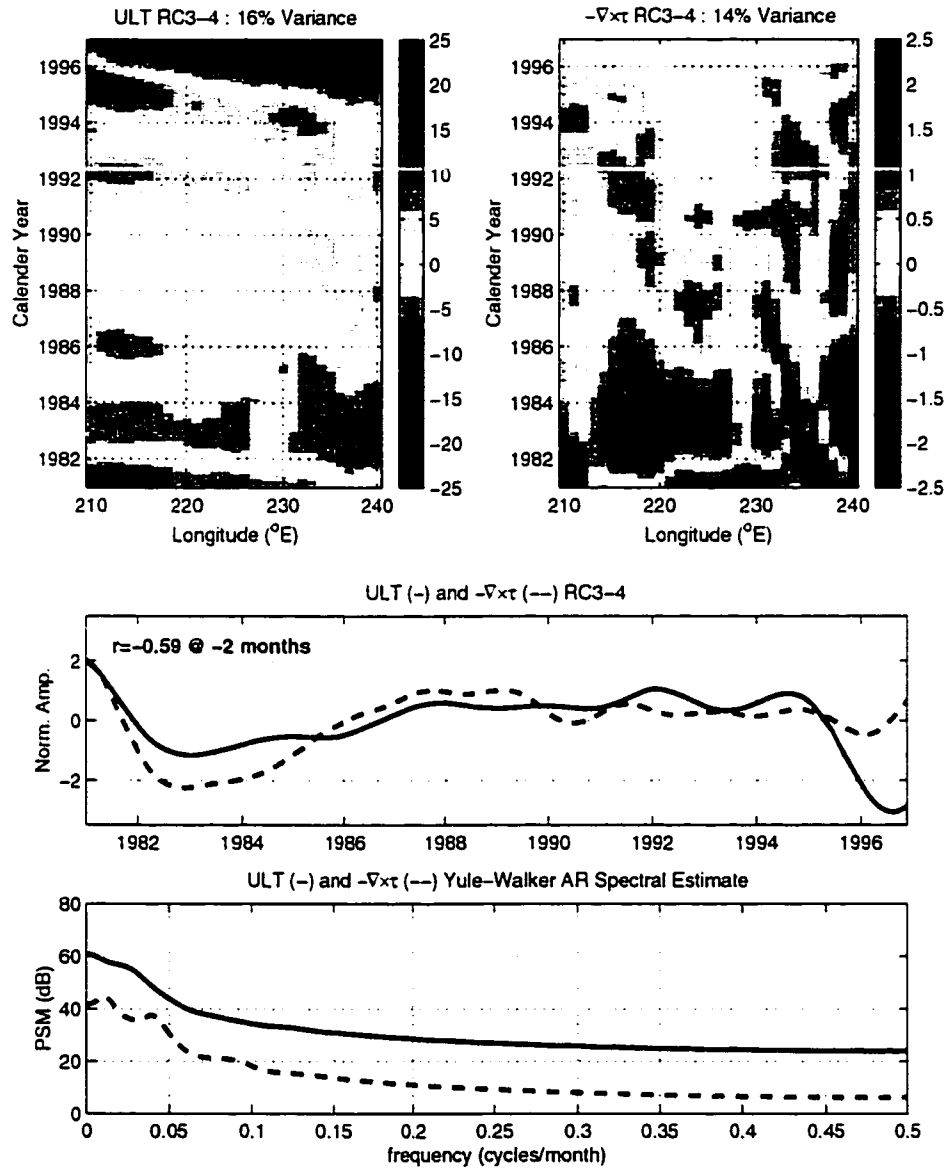


Figure 26: As in figure 25, but for M-SSA reconstructed modes 3 and 4 (RC_{3-4}). A clear interdecadal signal is exhibited with slight propagation. Both signals are highly correlated in time ($r = -0.59$ at the 99% level) with frequency peaks in the interdecadal bands.

M-SSA Reconstructed Principal Components Modes 5–10

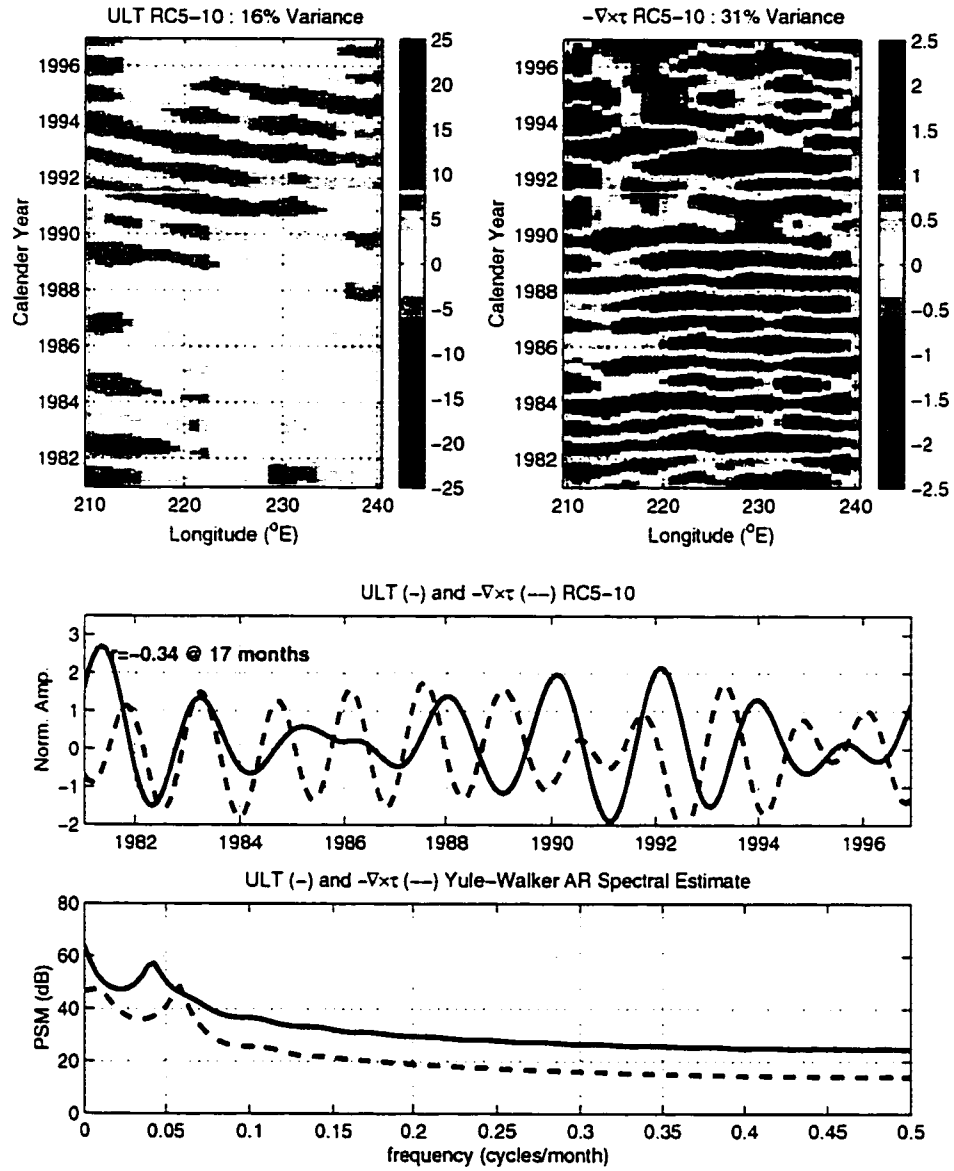


Figure 27: As in figure 25 but for M-SSA reconstructed modes 5 through 10 (RC_{5-10}). Quasi-biennial variability is exhibited for both ULT and WSC anomalies, but with low correlation. The two modes represent differing signals with ULT anomalies being biennial Rossby waves with a period of 24 months, and WSC anomalies representing a quasi-biennial standing mode with period of 17 months.

6. SUMMARY AND CONCLUSIONS

Interannual variability of the eastern subtropical Pacific Ocean has been examined using a high resolution numerical ocean model. The model results as well as ECMWF/HR forcing used agree extremely well with TOPEX/POSEIDON satellite altimetry and FSU pseudo-stresses respectively. The agreement is testament to the validity of the model as well as the state of ocean modeling and its ability to reproduce the dynamical nature of the oceans.

Previous results in the eastern tropical and subarctic Pacific Ocean suggest a primary source of interannual variability to be attributed to westward propagating Rossby waves. Two distinct forms of Rossby waves are found to exist. Of leading order importance, the primary Rossby wave signature is a wind forced Rossby wave with phase speed ($C_r \simeq 12 \text{ cm/s}$) faster than that expected by linear theory. The secondary Rossby wave signature, with phase speed ($C_r \simeq 8 \text{ cm/s}$) in accord with linear theory, stems from coastally trapped, poleward propagating Kelvin Waves generated in mid-basin along the equatorial Pacific.

Associated with the leading order wind forced Rossby wave is an interannual wind stress curl (WSC) fluctuation. Multi-channel singular spectrum analysis (M-SSA) results suggest both WSC and upper layer thickness (ULT) anomalies propagate westward at roughly 12 cm/s after being generated in the interior. WSC anomalies lead ULT anomalies by 3 months, suggesting a forced ocean-atmosphere response exists in which ULT and WSC anomalies are intricately tied.

With reference to current observational and modeling efforts, speculation about

the nature of the forced mode is made. Namely, the forced atmosphere-ocean mode exists on interannual time scales and may be part of a positive feedback loop in which large scale propagating sea surface temperature anomalies feed the overlying atmosphere. In return, these atmospheric anomalies feed the oceanic ULT anomalies and continue progression of the oceanic wave pattern. Speculation aside, however, the results presented here are consistent with the idea that extratropical surface wind anomalies are an important source of interannual variability in the ocean. As such, further understanding of interannual variability in the subtropical Pacific Ocean would benefit from more thorough investigations of the ideas expressed here.

In addition to interannual WSC and ULT variability, an inter-decadal mode (IDM) of variability is shown to exist over the same region. SVD and CEOF analysis reveal the IDM to be a leading order source of variability, but lack of sufficient temporal data limit the extent to which this feature can be adequately examined in the present study. However, the feature is consistent with inter-decadal variability and amplifications in the Aleutian Low and should be studied further.

The events described have potentially large impacts at all time scales for not only oceanic large and mesoscale variability, but also on biological/ecological productivity over a vast area of the eastern Pacific Ocean. As such, further effort should be placed on examining the features, discerning the nature of its variability, and studying its effects on marine ecosystems. Examination of the biological/ecological impacts of the interannual variability described herein and the dynamics of the IDM are left to future research.

APPENDIX A. SYMBOLS

Symbol	Definition
a	radius of the Earth (6371 km);
A_H	coefficient of horizontal viscosity;
C_b	coefficient of bottom friction;
C_k	coefficient of interfacial friction;
C_M	coefficient of additional interfacial friction associated with entrainment;
$D(\phi, \theta)$	ocean depth at rest;
f	Coriolis parameter;
g	acceleration due to gravity;
$G_{kl} = g$	$l \leq k$;
$G_{kl} = g - g \frac{\rho_l - \rho_k}{\rho_0}$	$l > k$;
h_k	kth layer thickness;
h_k^+	kth layer thickness at which entrainment starts;
h_k^-	kth layer thickness at which detrainment starts;
H_k	kth layer thickness at rest;
$H_n = D(\phi, \theta) - \sum_{l=1}^{n-1} H_l$;
$\hat{i}, \hat{j}, \hat{k}$	unit vectors positive eastward, northward, and upward respectively;

t	time;
\vec{v}_k	kth layer velocity;
\vec{V}_k	$h_k \vec{v}_k$;
θ	latitude;
ϕ	longitude;
ρ_k	kth layer density (constant for space and time);
ρ_0	reference density (constant);
$\vec{\tau}_w$	wind stress;
$\vec{\tau}_k = \vec{\tau}_w$	$k = 0$;
$\vec{\tau}_k = C_k \rho_0 \vec{v}_k - \vec{v}_{k+1} (\vec{v}_k - \vec{v}_{k+1})$	$k = 1 \dots n - 1$;
$\vec{\tau}_k = C_b \rho_0 \vec{v}_n \vec{v}_n$	$k = n$;
$\omega_k = 0$	$k = 0, n$;
$\omega_k = \omega_k^+ - \omega_k^- - \Omega_k \hat{\omega}_k$	$k = 1 \dots n - 1$;
$\omega_k^+ = \tilde{\omega}_k [\frac{\max(0, h_k^+ - h_k)}{h_k^+}]^2$;	
$\omega_k^- = \tilde{\omega}_k [\frac{\max(0, h_k - h_k^-)}{h_k^-}]^2$;	
$\hat{\omega}_k = \frac{\int \int (\omega_k^+ - \omega_k^-)}{\int \int \Omega_k}$;	
$\tilde{\omega}_k$	kth interface reference diapycnal mixing velocity;
$\Omega_k(\phi, \theta)$	kth interface weighting factor for mass conservation.

APPENDIX B. HANNING FILTER

Filtering data to isolate or remove specific physical signals is an important tool available to geophysical scientists. However, too often data is filtered and the results discussed without making explicit statements as to the effects of the filtering process. In particular, researchers often state which frequencies have been isolated or removed as a result of applying a given filter, analytical or digital, but fail to provide substantive evidence for their claims. The aim of this section is to explicitly describe the analytical response of a common filter used in the atmospheric and oceanic sciences, and in this work, the Hanning filter.

The Hanning window filter, or Hanning filter as it is commonly known, is a filter that utilizes past, present, and future information from a digital or analog signal to determine the output of a signal in a desired frequency range, much like filters that utilize rectangular or triangular windows. Unlike the rectangular and triangular windows, however, which use information provided in a given range of the data, the Hanning filter uses the complete past and future information of the signal to determine the desired signal response by weighting the values decreasing as the cosine of the time in the past or future. Thus, it is commonly referred to as the raised cosine or sine squared window.

The most common implementation of the Hanning filter is to apply a one-two-one filter repetitively until the desired response is achieved. Mathematically, the

one-two-one filter is equivalent to

$$\overline{F}_n = \frac{1}{4}[F_{n-1} + 2F_n + F_{n+1}] \quad (1)$$

where F_n and \overline{F}_n correspond the original and filtered values of the function at time n .

Now, we can rewrite F_n and \overline{F}_n as

$$\begin{aligned} F_n &= Ae^{i\theta} \\ \overline{F}_n &= Be^{i\theta} \end{aligned} \quad (2)$$

where $\theta = 2\pi f_n \Delta t$, f_n is the frequency and Δt is the time rate of change between samples. Equation (2) is essentially like taking the discrete Fourier Transforms (DFT) of F_n and \overline{F}_n .

Utilizing equation (2), equation (1) becomes

$$Be^{in\theta} = \frac{A}{4} [e^{i(n-1)\theta} + 2e^{i(n)\theta} + e^{i(n+1)\theta}]. \quad (3)$$

Canceling terms and applying trigonometric principles reduces equation (3) further to

$$B = \frac{A}{4}[2 + 2\cos \theta]. \quad (4)$$

Defining the frequency response function, FRF, as

$$FRF = \left(\frac{B}{A} \right) = \left(\frac{1}{2} + \frac{1}{2} \cos \theta \right) \quad (5)$$

the response of the given function, in spectral space, can clearly be seen as the sum of the past and future signal response at time n with decreased cosine response weighting (figure 28, bottom).

Using mathematical induction, it can be shown that j successive applications of a Hanning filter leads to the frequency response function

$$FRF_j = \left(\frac{1}{2} + \frac{1}{2} \cos \theta \right)^j. \quad (6)$$

At first glance, equation (6) may seem a little suspicious, that is to say, the relationship seems too simple. However, thinking about the filter in terms of DFT's (or Fast Fourier Transforms (FFT's)) sheds some light on the matter.

Let the DFT of a input signal $x(t)$ be labeled as $\Phi(\omega) = DFT(x(t))$. Similarly, let the DFT of the output signal $y(t)$ be labeled as $\Upsilon(\omega) = DFT(y(t))$. Then, applying the Hanning filter to the input signal is identical to the convolution of the FRF with the DFT of the input signal

$$\Upsilon(\omega) = FRF * \Phi(\omega). \quad (7)$$

Successive applications of the Hanning filter are simply the convolution of the FRF

with the previous filtered response

$$\Upsilon(\omega)_j = FRF * (FRF * (\dots \Phi(\omega))) \quad (8)$$

where j represents the number of Hanning filter applications, and the convolution $(FRF * (\dots))$ is applied j times. Clearly, the cumulative FRF associated with equation (8) can be none other than provided by equation (6).

Finally, since we are interested in how much of the signal at the given frequency we have retained it is essential to discuss the notion of power. The power of the filter can be defined simply as the square of the frequency response function. Thus, when examining the response of an input signal we can explain the percentage of the power that is retained by the filter by simply looking at the FRF. For example, if we apply a Hanning filter to an input time series (see figure 28) 6 times successively, we want to know how much of the power at time scales longer than 1 year (frequencies of 0.0027day^{-1}) is retained. Clearly, we see that at time scales longer than 1 year (represented by the dashed line in figure 28, bottom) over 40% of the power is retained, with increasingly more power retained at the lower frequencies.

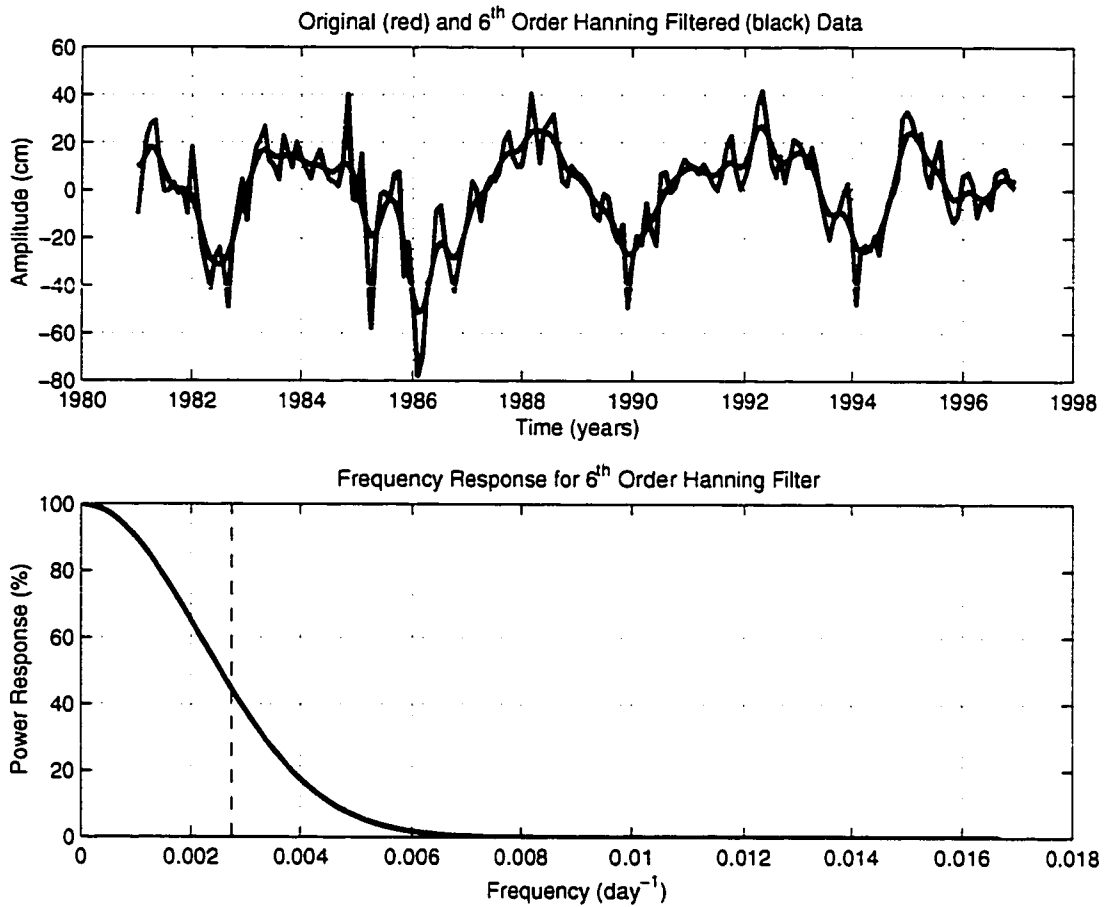


Figure 28: Example of successive application of a Hanning filter. Here, the order of the hanning filter represents the number of successive applications of the filter, i.e. a 6th order Hanning filter means the filter was applied repetitively 6 times to the original data. Top: The original data along with the low pass filtered data. Bottom: Power response associated with the 6th order Hanning filter. Clearly, over 40% of the power is retained at frequencies lower than 0.0027 day^{-1} (dashed line, corresponding to a time scales longer than 1 year).

APPENDIX C. (INTER)DECADAL VARIABILITY

As noted in the text, the dominant mode in both the singular value decomposition (SVD) and complex empirical orthogonal function (CEOF) analyses is a long term decadal or interdecadal signature. Unfortunately, the model time series length is not sufficiently long enough to discern the true nature of the signal. However, there is evidence to suggest that the signal is in fact realistic in nature. The signal is discussed in this appendix in an attempt to provide the physical mechanism behind the signal.

Since the SVD and CEOF analyses both reveal the interdecadal mode (IDM), it is only necessary to further examine one of them. Here, the SVD analysis will be discussed in an effort to more clearly depict the connection between the wind stress curl (WST) and the upper layer thickness (ULT) response to the IDM. Analogous results hold for the CEOF analysis with the exception that the CEOF analysis contains information about the propagation characteristics of the pattern. These will be discussed without showing results of the CEOF analysis itself, but rather will rely upon prior observational and analytical evidence.

SVD analysis is extended to include the area between 10°-60°N latitude and 120°-280°E longitude in an effort to obtain the true nature of the IDM while minimizing the strong equatorial effects of ENSO. Additionally, since they are the most relevant, only the first two modes of the SVD analysis are discussed.

The first SVD mode (figure 29, SVD1) represents a strong decadal scale pattern commonly known as the Pacific (inter)Decadal Oscillation (PDO, *Mantua et al.* 1997)

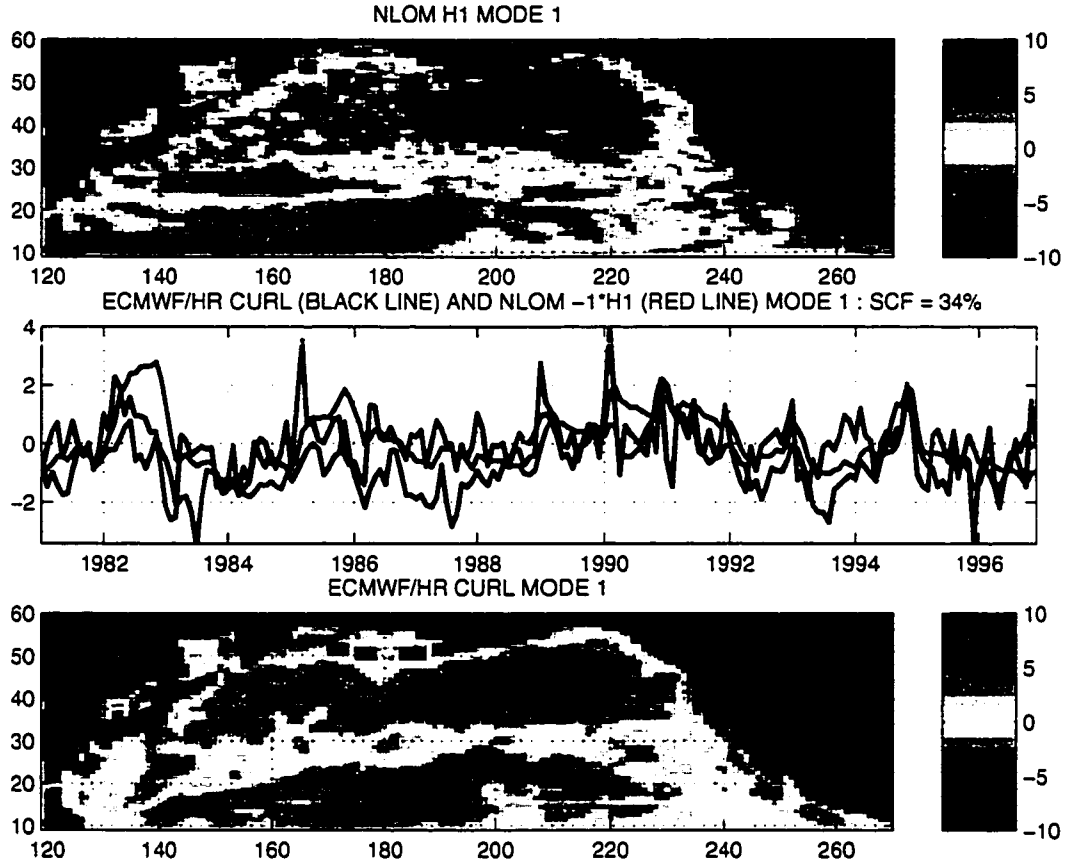


Figure 29: First mode SVD spatial eigenvectors of the monthly mean NLOM upper layer thickness (top) and ECMWF/HR monthly wind stress curl (bottom) along with their associated eigenfunctions (middle, NLOM=black line, ECMWF/HR=red line) accounting for 34% of the overall variance. For comparison purposes, the PDO index is plotted (in blue) along with the SVD eigenfunctions.

and encompasses 34% of the overall variance. Temporally, the PDO coincides with the southern oscillation index (SOI) such that a positive (negative) polarity in the PDO corresponds with ENSO warm (cold) phases, the primary difference being a stronger interdecadal component within the PDO time series. Clearly, the correlation between the PDO index and the first mode eigenfunctions is strong with notable deviations occurring during ENSO warm and cold events (e.g. 1983, 1985).

Spatially, SVD1 and the PDO exhibit the largest anomalies in the Central North

Pacific Ocean with colder/thinner (warmer/thicker) than normal SST's/ULT's associated with the PDO positive (negative) phase spanning from 20°-60°N and 120°-220°E. East of this, stretching from the Gulf of Alaska (GOA), through the Hawaiian Islands, and to the western boundary east of Taiwan and the Philippines, lies a cusp of warmer/thicker (colder/thinner) water. Differences between the SVD1 and the PDO are likely the result of the hydrodynamic nature of the model. Even-so, the model picks up the PDO extremely well given the temporal limitations of the modeled results. It is additionally interesting to note that when the SVD and CEOF analyses are performed only over the region of the of interest, east of the Hawaiian Islands, the PDO does not show up as a strong mode of variability, except in the sense that it modifies the background state upon which the other modes of variability act.

Similar to SVD1, the second SVD mode (SVD2 with 20% of the overall variance, figure 30) represents another interdecadal signature, a relationship between the ULT and the strength of the Aleutian Low (AL). The AL was first examined as a possible source of interdecadal variability when *Beamish and Bouillon* (1993) noted a strong correlation between Pacific Salmon production trends and the strength of the AL. The resulting Aleutian Low Pressure Index (ALPI) is a measure of the average winter season oceanic coverage of the AL (in km^2). Since then, numerous studies have used the ALPI as a benchmark for climatological responses in fish stock and biological production in the North Pacific (*Polovina et al.* 1995, *Beamish et al.* 1999, *Anderson and Piatt* 1999).

The ALPI suggests that large spatial and long temporal scale changes exist in the strength of the Aleutian Low. During normal conditions the AL, centered over the Aleutian Islands, begins to form during autumn, increases in strength over the winter months, and finally diminishes in strength before breaking down in the summer.

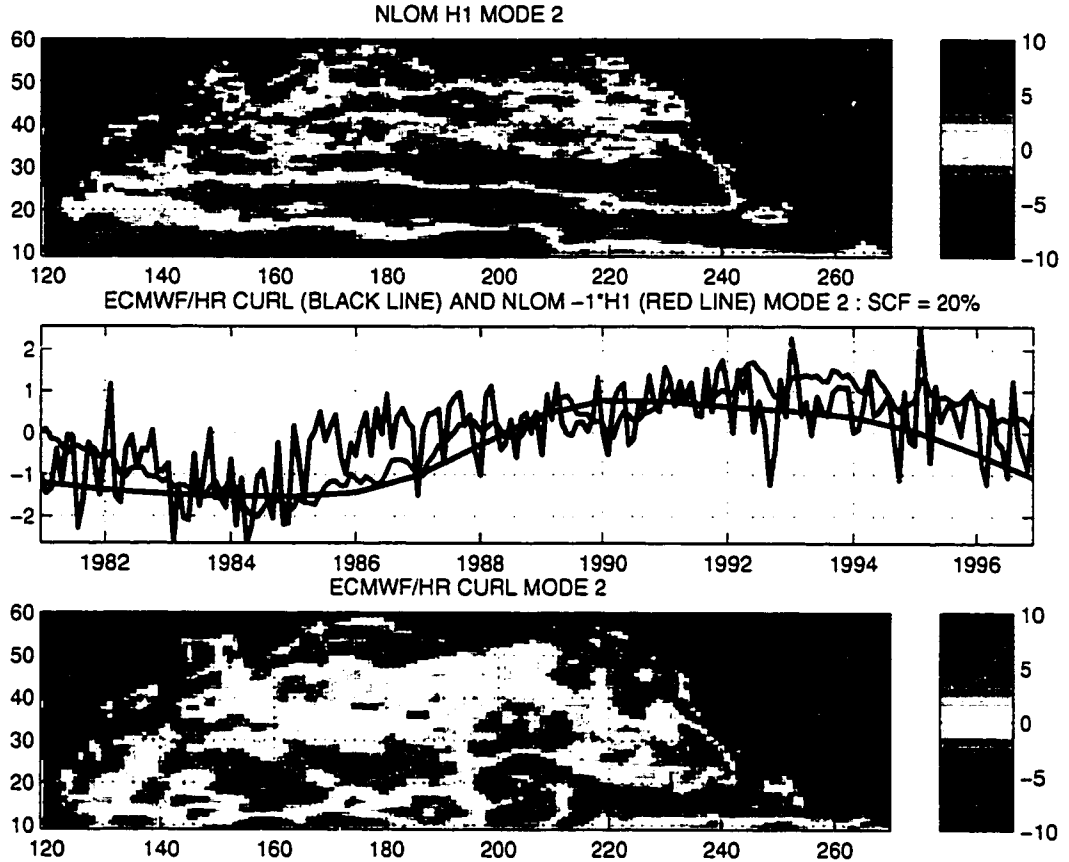


Figure 30: Second mode SVD spatial eigenvectors of the monthly mean NLOM upper layer thickness (top) and ECMWF/HR monthly wind stress curl (bottom) along with their associated eigenfunctions (middle, NLOM=black line, ECMWF/HR=red line) accounting for 20% of the overall variance. For comparison purposes, the low pass filtered ALPI is plotted (in blue) along with the SVD eigenfunctions.

Following a climate shift in 1977, the AL both intensified and shifted south resulting in stronger westerly winds and warmer surface waters in the GOA (*Anderson and Piatt* 1999). SVD2 results reveal this impact with a strong WST gradient south of the GOA associated with the increased westerlies. In accordance, a strong WST gradient, and associated ULT gradient, also exists east of the Hawaiian Islands. This WST gradient shows up as a dominant mode of variability over the eastern Pacific Ocean subtropical gyre (see section 5.1).

Physically, the two IDM's account for $\sim 54\%$ of the overall coupled variance of the North Pacific. Clearly, non ENSO-related, large scale changes are evident over the basin as a whole. The results presented here, although limited in scope due to the reduced temporal input, compare well with observational results, and suggest interdecadal variability of the WST not only in the GOA, but also over the subtropical eastern Pacific Ocean. However, it is left to future research to determine what the nature of this variability is. For the purposes here, it is sufficient to qualitatively explain the source of variability while noting the impacts.

REFERENCES

- Allen, M. R., and A. W. Robertson, Distinguishing modulated oscillations from coloured noise in multivariate datasets, *Climate Dyn.*, *12*, 775–784, 1996.
- Allen, M. R., and L. A. Smith, Monte Carlo SSA: detecting irregular oscillations in the presence of coloured noise, *J. Climate*, *9*, 3373–3404, 1996.
- Anderson, P. J., and J. F. Piatt, Community reorganization in the Gulf of Alaska following ocean climate regime shift, *Mar. Ecol. Prog. Series*, *189*, 117–123, 1999.
- Archiving, Validation, and Interpretation of Satellite Oceanographic data, *CD-ROM user manual: Merged TOPEX/POSEIDON products*, aVI-NT-02-100-CN, Edition 2.1, 231 pp., 1992.
- Barnier, B., Numerical study on the influence of the mid-Atlantic ridge on nonlinear first-mode baroclinic rossby waves generated by seasonal winds, *jpo*, *18*, 417–433, 1988.
- Beamish, R. J., and D. R. Bouillon, Pacific salmon production trends in relation to climate, *Can. J. Fish. Aquat. Sci.*, *50*, 1002–1016, 1993.
- Beamish, R. J., D. J. Noakes, G. A. McFarlane, L. Klyashtorin, V. V. Ivanov, and V. Kurashov, The regime concept and natural trends in the production of Pacific Salmon, *Can. J. Fish. Aquat. Sci.*, *56*, 516–526, 1999.
- Bretherton, C. S., C. Smith, and J. M. Wallace, An intercomparison of methods for finding coupled patterns in climate data, *J. Climate*, *5*, 541–560, 1992.
- Busalacchi, A. J., and J. J. O'Brien, The seasonal variability in a model of the tropical Pacific, *J. Phys. Oceanogr.*, *10*, 1929–1951, 1980.
- Busalacchi, A. J., K. Takeuchi, and J. J. O'Brien, Interannual variability of the Equatorial Pacific - revisited, *J. Geophys. Res.*, *88*, 7551–7562, 1983.
- Callahan, P. S., *TOPEX/POSEIDON project GDR user's handbook*, JPL D-8944, rev. A, Jet Propul. Lab., Pasadena, Calif., 1993.
- Chelton, D. B., and R. E. Davis, Monthly mean sea-level variability along the west coast of North America, *J. Phys. Oceanogr.*, *12*, 757–784, 1982.

- Chelton, D. B., and M. G. Schlax, Global observations of oceanic Rossby Waves, *272*, 234–238, 1996.
- Cheney, R. E., J. G. Marsh, and B. D. Beckley, Global mesoscale variability from collinear tracks of Seasat altimeter data, *J. Geophys. Res.*, *88*, 4343–4354, 1983*a*.
- Cheney, R. E., J. G. Marsh, and B. D. Beckley, Global mesoscale variability from collinear tracks of Seasat altimeter data, *J. Geophys. Res.*, *88*, 4343–4354, 1983*b*.
- Cheng, X., and T. J. Dunkerton, Orthogonal rotation of spatial patterns derived from singular value decomposition analysis, *J. Climate*, *8*, 2631–2643, 1995.
- Dewar, W. K., On “too fast” planetary waves in the general circulation, *J. Phys. Oceanogr.*, *28*, 1739–1758, 1998.
- Eanes, R. J., and S. V. Bettadpur, *The CSR 3.0 Global Ocean Tide Model*, cSR- TM- 95- 06, Center for Space Research, Univ. of Texas at Austin, 1995.
- Emery, W. J., and R. E. Thomson, *Data Analysis Methods in Physical Oceanography*, Elsevier Science Inc., 634 pp., 1997.
- European Centre for Medium-Range Weather Forecasts, *User guide to ECMWF products*, meteorological Bulletin M3.2, ECMWF, Reading, Berkshire, UK, 1995.
- Fu, L. L., E. J. Christensen, C. A. Y. Jr., M. Lefebvre, Y. Ménard, M. Dorrer, and P. Escudier, TOPEX/POSEIDON mission overview, *J. Geophys. Res.*, *99*, 24369–24382, 1994.
- Gill, A. E., *Atmosphere-Ocean Dynamics*, Academic Press, 662 pp., 1982.
- Gill, A. E., and A. J. Clarke, Wind induced upwelling, coastal currents and sea-level changes, *Deep Sea Res.*, *21*, 321–345, 1974.
- Goldenberg, S. B., and J. J. O'Brien, Time and space variability of the tropical Pacific wind stress, *Mon. Wea. Rev.*, *6*, 1190–1207, 1981.
- Hellerman, S., and M. Rosenstein, Normal monthly wind stress over the World Ocean with error estimates, *J. Phys. Oceanogr.*, *13*, 1093–1104, 1983.
- Hundermark, B. A., H. E. Hurlburt, E. J. Metzger, and J. F. Shriver, *A comparison of wind stresses derived from archived operational European Centre for Medium-Range Weather Forecasts 1000 mb winds and Florida State University psuedo stresses over the Tropical Pacific Ocean, 1981-1993*, Nav. Res. Lab, Stennis Space Center, Miss., 40 pp., 1999.
- Hurlburt, H. E., and J. D. Thompson, A numerical study of the Loop Current intrusions and eddy-shedding, *J. Phys. Oceanogr.*, *10*, 1611–1651, 1980.

- Hurlburt, H. E., A. J. Wallcraft, W. J. Schmitz Jr., P. J. Hogan, and E. J. Metzger, Dynamics of the Kuroshio/Oyashio current system using eddy-resolving models of the North Pacific Ocean, *J. Geophys. Res.*, *101*, 941–976, 1996.
- Jacobs, G. A., H. E. Hurlburt, J. C. Kindle, E. J. Metzger, J. L. Mitchell, W. J. Teague, and A. J. Wallcraft, Decade-scale trans-Pacific propagation and warming effects of an El Niño anomaly, *Nature*, *370*, 360–363, 1994.
- Johnson, M. A., and J. J. O'Brien, The Northeast Pacific Ocean response to the 1982–1983 El Niño, *J. Geophys. Res.*, *95*, 7155–7166, 1990.
- Kang, Y. Q., and L. Magaard, Annual baroclinic waves in the Central North Pacific, *J. Phys. Oceanogr.*, *10*, 1159–1167, 1980.
- Kelly, K. A., Comment on “empirical orthogonal function analysis of advanced very high resolution radiometer surface temperature patterns in Santa Barbara channel” by G. S. E. Lagerloef and R. L. Bernstein, *J. Geophys. Res.*, *93*, 15753–15754, 1988.
- Keppenne, C. L., and M. Ghil, Adaptive spectral analysis and prediction of the Southern Oscillation index, *JGR*, *97*, 20,449–20,454, 1992.
- Keppenne, C. L., and M. Ghil, Adaptive filtering and prediction of noisy multivariate signals: an application to subannual variability in atmospheric angular momentum. *Int. J. Bifurcat. Chaos*, *3*, 625–634, 1993.
- Kessler, W. S., Observations of long Rossby waves in the northern tropical Pacific, *J. Geophys. Res.*, *95*, 5183–5217, 1990.
- Killworth, P. D., D. B. Chelton, and R. A. deZoeke, The speed of observed and theoretical extra tropical planetary waves, *J. Phys. Oceanogr.*, *27*, 1946–1966, 1997.
- Leonardi, A. P., H. E. Hurlburt, E. J. Metzger, , and J. J. O'Brien, Dynamics of the North Hawaiian Ridge Current, *J. Phys. Oceanogr.*, *in review*, 2000.
- Leuliette, E. W., and J. M. Wahr, Coupled pattern analysis of sea surface temperature and TOPEX/Poseidon sea surface height, *J. Phys. Oceanogr.*, *29*, 599–611, 1999.
- Magaard, L., On the potential energy of baroclinic Rossby waves in the North Pacific, *J. Phys. Oceanogr.*, *13*, 38–42, 1983.
- Mantua, N. J., S. R. Hare, Y. Zhang, J. M. Wallace, and R. C. Francis, A Pacific interdecadal climate oscillation with impacts on salmon production, *Bull. Am. Meteor. Soc.*, *78*, 1069–1079, 1997.
- Messinger, F., and A. Arakawa, *Numerical Methods Used in Atmospheric Models*, GARP Publ. Serv., World Meteorological Organization, 64 pp., 1976.

- Metzger, E. J., and H. E. Hurlburt, Coupled dynamics of the South China Sea, the Sulu Sea and the Pacific Ocean, *J. Geophys. Res.*, *101*, 12331–12352, 1996.
- Meyers, G., Seasonal variation in transport of the Pacific North Equatorial Current relative to the wind field, *J. Phys. Oceanogr.*, *5*, 442–449, 1975.
- Meyers, G., On the annual Rossby wave in the tropical North Pacific Ocean, *J. Phys. Oceanogr.*, *9*, 663–674, 1979.
- Miller, A. J., W. B. White, and D. R. Cayan, North Pacific thermocline variations on ENSO timescales, *J. Phys. Oceanogr.*, *27*, 2023–2039, 1997.
- Mitchell, J. L., W. J. Teague, G. A. Jacobs, and H. E. Hurlburt, Kuroshio Extension dynamics from satellite altimetry and a model simulation, *J. Geophys. Res.*, *101*, 1045–1058, 1996.
- Mitchum, G. T., Principle component analysis: basic methods and extensions, in *Proceedings of the 'Aha Huliko'a Hawaiian winter workshop*, edited by P. Müller and D. Henderson, 185–199, SOEST, University of Hawaii, Honolulu, HI, 1993.
- Murray, C. P., S. L. Morey, and J. J. O'Brien, Interannual variability of upper ocean vorticity balances in the Gulf of Alaska, *J. Geophys. Res.*, *in review*, 2000.
- NOAA, ETOP05 digital relief of the surface of the earth, Natl. Geophys. Data Cent., Washington, D.C., data Announce. 86-MGG-07, 1986.
- Pares-Sierra, A., and J. J. O'Brien, The seasonal and interannual variability of the California Current system, *J. Geophys. Res.*, *94*, 3159–3180, 1989.
- Polovina, J. J., G. T. Mitchum, and G. T. Evans, Decadal and basin-scale variation in mixed layer depth and the impact on biological production in the Central and North Pacific, 1960–88, *Deep Sea Res.*, *42*, 1701–1716, 1995.
- Preisendorfer, R. W., *Principal component analysis in meteorology and oceanography*, Elsevier, 1988.
- Qiu, B., W. Mao, and P. Müller, Propagation and decay of forced and free baroclinic Rossby waves in off-equatorial oceans, *J. Phys. Oceanogr.*, *27*, 2405–2417, 1997.
- Shriver, J. F., and H. E. Hurlburt, The contribution of the global thermohaline circulation to the Pacific to Indian Ocean throughflow via Indonesia, *J. Geophys. Res.*, *102*, 5491–5511, 1997.
- Shriver, J. F., M. A. Johnson, and J. J. O'Brien, Analysis of remotely forced oceanic Rossby waves off California, *J. Geophys. Res.*, *96*, 749–757, 1991.
- Stommel, H., A survey of ocean current theory, *Deep Sea Res.*, *4*, 149–184, 1957.

- Stricherz, J. N., J. J. O'Brien, and D. M. Legler, *Atlas of Florida State University Tropical Pacific Winds for TOGA 1966-1985*, florida State University, Tallahassee, FL, 250 pp., 1992.
- Stricherz, J. N., D. M. Legler, and J. J. O'Brien, *TOGA pseudo-stress atlas 1985-1994, Volume II: Pacific Ocean*, florida State University, Tallahassee, FL, 158 pp., 1997.
- Tourre, Y. M., Y. Kushnir, and W. B. White, Evolution and variability in sea level pressure, sea surface temperature, and upper ocean temperature over the Pacific Ocean, *jpo*, 29, 1528-1541, 1999.
- Vautard, R., P. Yiou, and M. Ghil, Singular spectrum analysis: a toolkit for noisy and chaotic series, *Physica D.*, 58, 95-126, 1992.
- Waliser, D. E., and C. Gautier, A satellite derived climatology of the ITCZ, *J. Climate*, 6, 2162-2174, 1993.
- Wallace, J. M., C. Smith, and C. S. Bretherton, Singular value decomposition of wintertime sea surface temperature and 500-mb height anomalies, *J. Climate*, 5, 561-576, 1992.
- Wallcraft, A. J., *The Navy Layered Ocean Model user's guide*, Nav. Res. Lab, Stennis Space Center, Miss., 21 pp., 1991.
- Wang, B., Interdecadal changes in El Niño onset in the last four decades, *J. Climate*, 8, 267-285, 1995.
- Wang, X. L., and C. F. Ropelewski, An assesment of ENSO-scale secular variability, *J. Climate*, 8, 1584-1599, 1995.
- White, W. B., Annual forcing of baroclinic long waves in the tropical North Pacific, *J. Phys. Oceanogr.*, 7, 50-61, 1977.
- White, W. B., A wind driven experiment of the seasonal cycle of the main thermocline in the interior Midlatitude North Pacific, *J. Phys. Oceanogr.*, 8, 818-824, 1978.
- White, W. B., Slow El Niño-Southern Oscillation boundary waves, *J. Geophys. Res.*, 99, 22,737-22,751, 1994.
- White, W. B., Tropical coupled Rossby waves in the Pacific ocean-atmosphere system, *J. Phys. Oceanogr.*, 30, 1245-1264, 2000.
- White, W. B., and D. R. Cayan, A global El Niño-Southern Oscillation wave in surface temperature and pressure and its interdecadal modulation from 1900 to 1997, *J. Geophys. Res.*, 105, 11,223-11,242, 2000.

- White, W. B., and J. P. McCreary, Eastern intensification of ocean spin-down: application to El Niño, *J. Phys. Oceanogr.*, *4*, 295–303, 1974.
- White, W. B., G. A. Meyers, J. R. Donguy, and S. E. Pazan, Short-term climatic variability in the thermal structure of the Pacific Ocean during 1979–1982, *J. Phys. Oceanogr.*, *15*, 917–935, 1985.
- White, W. B., S. E. Pazan, and M. Inoue, Hindcast/forecast of ENSO events based upon the redistribution of observed and model heat content in the Western Tropical Pacific, 1964–86, *J. Phys. Oceanogr.*, *17*, 264–280, 1987.
- White, W. B., Y. Chao, and C. K. Tai, Coupling of biennial oceanic Rossby waves with the overlying atmosphere in the Pacific basin, *J. Phys. Oceanogr.*, *28*, 1236–1251, 1998.

BIOGRAPHICAL SKETCH

Degrees

Ph.D., Oceanography, 2000, Florida State University

M.S., Oceanography, 1998, Florida State University

B.S., Meteorology, 1995, University of Wisconsin - Madison

Experience

Florida State University. Center for Ocean-Atmospheric Prediction Studies.

Programmer. Responsibilities included programming and data analysis utilizing Satellite Scatterometer data and Research Vessel data for the COARE region. 1995.

Florida State University. Naval Research Laboratory Graduate Research Fellow.

Projects involve examining the flow in the North Pacific Ocean using the NRL Layered Ocean Model, and implementation of the model on the Silicon Graphics Power Challenge Array supercomputer at Florida State University. In addition, responsibilities include work on other research leading to publications. 1995-1998.

NRL, Stennis Space Center. Summer research program. Spent summer conducting research and interacting with scientists. Projects involved working with the NRL Layered Ocean Model. 1996.

World Ocean Circulation, WOCE-ACCE cruise participant. Data collection and analysis for three week leg from Fortaleza, Brazil, to Cape Town, South Africa. July/August 1997.

The Florida State University. National Aeronautics and Space Administration Earth System Science Graduate Research Fellow. Projects involved examining the flow in the Tropical Pacific Ocean using general ocean circulation models and altimeter data. 1998-2000.

Universities Space Research Association (USRA) Graduate Student Summer Program (GSSP) participant. The program involved working closely with scientists at the National Aeronautic and Space Administration (NASA) Goddard Space Flight Center (GSFC) in Greenbelt, Maryland. Research included an in depth examination of Topex/Poseidon satellite altimetry and high resolution numerical model results. 06/1999-08/1999.

Universities Space Research Association (USRA) - NASA Goddard Space Flight Center's Earth and Space Data Computing Division (ESDCD) Summer School for High Performance Computational Earth and Space Sciences. July 2000.

Honors

Naval Research Laboratory (NRL) Graduate Research Fellowship, 1995-1998.

NASA ESS Graduate Research Fellowship, 1998-2000.

NASA GSSP Summer Fellowship, 1999

Outstanding Oceanography Graduate Student Award, FSU, 1999

Memberships

American Geophysical Union.

The Oceanography Society.

American Meteorological Society.

Personal information

Born 10 December 1972, Crystal Falls, Michigan